



**LIGHT SHIFT COMPENSATION
FOR THE RUBIDIUM TWO-PHOTON CLOCK
STUDIES USING A 1556.2 NM WAVELENGTH MITIGATION LASER**

Thèse présentée à la Faculté des Sciences de l'Université de Neuchâtel
pour l'obtention du grade de Docteur ès Sciences

par

Roman Blum

Composition du jury:

Prof. Gaetano Mileti, directeur de thèse, Université de Neuchâtel, Suisse

Prof. Thomas Südmeyer, Université de Neuchâtel, Suisse

Dr Sylvain Karlen, CSEM, Neuchâtel, Suisse

Dr Pierre Waller, ESA/ESTEC, Noordwijk, Pays-Bas

Dr John Kitching, NIST, Boulder CO, USA

Soutenue le 14 mars 2025

IMPRIMATUR POUR THESE DE DOCTORAT

La Faculté des sciences de l'Université de Neuchâtel autorise
l'impression de la présente thèse soutenue par

Monsieur Roman BLUM

Titre :

“Light Shift Compensation for the Rubidium Two-Photon Clock: Studies using a 1556.2 nm Wavelength Mitigation Laser”

sur le rapport des membres du jury composé comme suit :

- **Prof. Gaetano Mileti**, directeur de thèse, Université de Neuchâtel, Suisse
- **Dr Sylvain Karlen**, CSEM SA, Suisse
- **Dr Pierre Waller**, European Space Agency, Pays-Bas
- **Prof. Thomas Södmeyer**, Université de Neuchâtel, Suisse
- **Dr John Kitching**, National Institute of Standards and Technology, USA

Neuchâtel, le 29 avril 2025

Le Doyen, Prof. P. Brunner



I han en Uhr erfunde
wo geng nach zwone Stunde
blybt stah.
— Mani Matter

To my parents

Acknowledgements

My colleagues at CSEM have been a great support and source of inspiration along the entire project. Above all, I thank Sylvain Karlen for following my work closely, guiding me when needed, and helping me find solutions to smaller and larger problems. I also thank Fabien Droz for sharing his vast experience with me. Moreover, I am very grateful for the help of Stefan Kundermann, Marianne Toimil Martinez, Sanghoon Chin, Thibaud Ruelle, Etienne Batori, Lauriane Karlen, Christoph Hofer, and many more. I thank CSEM for giving me the opportunity to work in such a stimulating environment. My thanks especially go to Steve Lecomte who has proposed me this thrilling position and has furthermore supported me in many occasions. This work would not have been possible without the funding from CSEM.

Furthermore, I am grateful for the support of the European Space Agency¹ and the great opportunity to stay at ESA/ESTEC as a visiting researcher during three interesting months. In particular, I thank Pierre Waller for his genuine interest in my work and his critical questions.

I also thank my colleagues at Laboratoire Temps-Fréquence at University of Neuchâtel. I am very grateful to Valentin Wittwer for providing the custom dichroic mirror for the atomic vapor cell assembly. In particular, my thanks go to my thesis director Prof Gaetano Mileti who has inspired me not only with his dedication to the research community but also with his passion for the history of the measurement of time.

Last but not least, I also thank my family and friends who have supported me in this adventure.

Bern, 14 April 2025

Roman Blum

¹The project has been financially supported through the ESA Open Space Innovation Platform (OSIP), ESA contract Nr 4000137744.

Abstract

Atomic clocks are essential for many modern applications in science and technology. By referencing the frequency of a local oscillator to an atomic electron transition, passive atomic clocks achieve outstanding levels of frequency stability and accuracy. In the last decades, the scientific interest in electron transitions in the optical frequency spectrum has grown considerably due to the invention of the optical frequency comb. Optical atomic clocks have an advantage over their traditional microwave frequency counterparts by making use of transitions with higher resonance quality factors, leading to improved short-term frequency stability.

The rubidium two-photon clock is a passive optical atomic clock that combines the high quality factor of an optical transition with the simplicity of hot atomic vapor cell technology. This makes it a promising technology for compact and miniature clocks and optical frequency standards. The combination of a small atomic vapor cell with an optical transition is possible through Doppler-free two-photon absorption spectroscopy of a hyperfine spectral component using a near-infrared interrogation laser beam at 778.1 nm wavelength.

However, the AC Stark shift (or light shift) often limits the long-term frequency stability. It maps fluctuations and drifts in laser intensity onto the atomic resonance and thus the clock frequency.

This thesis explores a light shift compensation scheme based on a mitigation laser beam at 1556.2 nm wavelength. The mitigation beam shifts the atomic resonance frequency in the opposite direction as the interrogation beam. Adjusting the intensity ratio of the two beams and combining them to jointly address the same atomic population in the vapor cell allows to control the magnitude of the resulting total AC Stark shift.

The compensation scheme is implemented and evaluated regarding frequency stability and accuracy. An optical frequency standard is designed, built and tested. In comparison to a conventional two-photon standard, it features the additional 1556.2 nm wavelength light shift mitigation beam whose power can be controlled independently of the one of the interrogation laser. Frequency instability at 1 second integration time is measured to a few parts in 10^{13} and

Abstract

averages down to a few parts in 10^{15} at longer integration times. With the added mitigation laser, an improvement in frequency accuracy is demonstrated. The dependence of the clock frequency on the interrogation laser intensity becomes negligible. A retrace measurement confirms the repeatability of the light shift mitigation.

Moreover, the potential for an improvement in frequency stability is assessed. With the mitigation scheme, the clock frequency sensitivity to reference voltage drifts is reduced by over an order of magnitude. Finally, an outlook on possible future research directions is given.

The characterization of this optical frequency standard requires an optical fiber link. The validity of the measurements must be verified since an optical frequency that is transferred via fiber acquires acoustic and thermal noise. Such perturbations can be detected and compensated with the so-called Doppler cancellation scheme.

In addition to the light shift mitigation setup, this thesis theoretically and experimentally discusses an extension of the Doppler cancellation scheme allowing to transmit two independent optical frequencies simultaneously. For this purpose, a primary and a secondary optical signal are multiplexed into the same optical fiber. The Doppler cancellation scheme is implemented for the primary signal. The transfer of the secondary signal is demonstrated to benefit from indirect stabilization. At 1000 seconds integration time, the stability of the optical frequency transfer of the secondary signal is improved by 16 dB using polarization multiplexing. Finally, practical limitations of the method are discussed and it is put in a broader context.

Keywords: Atomic Clock, Optical Frequency Standard, Rubidium, Two-Photon Absorption Spectroscopy, AC Stark Effect, Light Shift, Light Shift Mitigation, Optical Frequency Transfer, Optical Fiber Link.

Résumé

Les horloges atomiques sont essentielles pour plusieurs applications modernes en science et en technologie. En asservissant la fréquence d'un oscillateur local sur une transition électronique, les horloges atomiques passives atteignent des niveaux exceptionnels de stabilité et d'exactitude de fréquence. Ces dernières décennies, l'intérêt scientifique pour les transitions électroniques optiques augmenta considérablement grâce à l'invention du peigne de fréquences optiques. Les horloges atomiques optiques possèdent un avantage face aux horloges micro-ondes traditionnelles grâce à leur utilisation de transitions à facteurs de qualité plus élevés, ce qui mène à une amélioration de la stabilité de fréquence dans le court terme.

L'horloge de rubidium à deux photons est une horloge atomique optique passive qui combine le facteur de qualité élevé d'une transition optique avec la simplicité de la technologie des cellules à vapeurs chaudes. Ceci la rend une technologie prometteuse pour des horloges et des étalons de fréquence compacts et miniatures. La combinaison d'une petite cellule à vapeur avec une transition optique est possible grâce à la spectroscopie à deux photons sans effet Doppler d'un composant spectral hyperfin en utilisant un faisceau laser dans l'infrarouge proche qui a une longueur d'onde de 778.1 nm.

Néanmoins, l'effet Stark dynamique (ou décalage Stark) limite souvent la stabilité de fréquence dans le long terme. Il reproduit des fluctuations et des dérives de l'intensité du laser sur la résonance atomique et donc sur la fréquence d'horloge.

Cette thèse traite d'un schéma de compensation pour le décalage Stark qui est basé sur un faisceau laser de mitigation ayant une longueur d'onde de 1556.2 nm. Le faisceau de mitigation décale la fréquence de résonance atomique dans le sens opposé à celui du faisceau d'interrogation. En ajustant le ratio d'intensité des deux faisceaux et en les combinant afin d'adresser conjointement la même population atomique dans la cellule à vapeur, la magnitude du décalage Stark total qui en résulte peut être contrôlée.

Le schéma de compensation est implémenté et évalué en vue de la stabilité et de l'exactitude de fréquence. Un étalon de fréquence optique est conçu, construit et testé. En comparaison avec un étalon conventionnel à deux photons, il est doté du faisceau laser supplémentaire

Résumé

dit de mitigation dont la puissance optique peut être contrôlée de manière indépendante de celle du faisceau d'interrogation. L'instabilité de fréquence à un temps d'intégration de 1 seconde est mesurée à quelques parts en 10^{13} et se moyenne à quelques parts en 10^{15} pour des temps d'intégration plus longs. Avec le laser de mitigation supplémentaire, une amélioration de l'exactitude de fréquence est démontrée. La dépendance de la fréquence d'horloge à l'intensité du laser d'interrogation devient négligeable. Une mesure de retrace confirme la répétabilité de la mitigation du décalage Stark.

En outre, le potentiel pour une amélioration en stabilité de fréquence est évaluée. Avec ce schéma de mitigation, la sensibilité de la fréquence d'horloge aux dérives de tension de référence est réduite de plus d'un ordre de grandeur. Finalement, une perspective est donnée sur des directions de recherche à considérer à l'avenir.

La caractérisation de cet étalon de fréquence optique nécessite un lien optique fibré. La pertinence des mesures doit être vérifiée car une fréquence optique transmise par fibre acquiert du bruit acoustique et thermique. De telles perturbations peuvent être détectées et compensées grâce au schéma dit compensation de Doppler.

A part de la manipulation sur la mitigation du décalage Stark, cette thèse discute d'un point de vue théorique et expérimental une extension du schéma de compensation de Doppler qui permet de transmettre simultanément deux fréquences optiques. Dans ce but, un signal primaire ainsi qu'un signal secondaire sont regroupés dans la même fibre. Le schéma de compensation de Doppler est implémenté pour le signal primaire. Il est démontré que le transfert du signal secondaire profite d'une stabilisation indirecte. A un temps d'intégration de 1000 secondes, la stabilité du transfert du signal secondaire est amélioré de 16 dB en utilisant le multiplexage par polarisation. Finalement, des limites pratiques de la méthode sont discutées et mises en contexte.

Mots-clés : Horloge Atomique, Etalon de Fréquence Optique, Rubidium, Spectroscopie d'Absorption à Deux Photons, Effet Stark Dynamique, Décalage Stark, Modération du Décalage Stark, Transfert de Fréquence Optique, Lien Optique Fibré.

Zusammenfassung

Atomuhren sind unerlässlich für viele moderne Anwendungen in Technologie und Wissenschaft. Dadurch, dass die Frequenz eines lokalen Oszillators auf einen elektronischen Übergang referenziert wird, erreichen passive Atomuhren einen ausserordentlich hohen Grad an Frequenzstabilität und -genauigkeit. In den letzten Jahrzehnten hat durch die Erfindung des optischen Frequenzkammes das wissenschaftliche Interesse an optischen elektronischen Übergängen bedeutend zugenommen. Optische Atomuhren verfügen über einen Vorteil gegenüber traditionellen Mikrowellen-Uhren, da sie Übergänge mit höheren Qualitätsfaktoren nutzen und dadurch eine bessere Frequenz-Kurzzeitstabilität ermöglichen.

Die Rubidium-Zwei-Photonen-Uhr ist eine passive optische Atomuhr, die den hohen Qualitätsfaktor eines optischen Übergangs mit der Einfachheit einer heissen atomaren Dampfzelle kombiniert. Dadurch ist sie eine vielversprechende Technologie sowohl für kompakte als auch für miniaturisierte Uhren und Frequenzstandards. Die Kombination einer kleinen Dampfzelle mit einem optischen Übergang wird ermöglicht durch Doppler-Effekt-freie Zwei-Photonen-Absorptionsspektroskopie einer hyperfeinen Spektralkomponente im nahen Infrarot-Bereich mit 778.1 nm Wellenlänge.

Der dynamische Stark-Effekt (oder Lichtverschiebung) beschränkt jedoch oftmals die Frequenz-Langzeitstabilität. Dieser Effekt überträgt Fluktuationen und Nullpunktabweichungen der Laser-Intensität auf die atomare Schwingungsfrequenz und dadurch auf die Uhrenfrequenz.

Diese Arbeit behandelt ein Kompensationsschema für die Lichtverschiebung, welches auf einem Milderungslaser mit 1556.2 nm Wellenlänge basiert. Der Milderungslaser verschiebt die atomare Schwingungsfrequenz in die entgegengesetzte Richtung wie der Abfragestrahl. Dadurch, dass das Intensitätsverhältnis der beiden Strahlen angepasst wird und diese zur gemeinsamen Ansprache der gleichen Population von Atomen in der Dampfzelle überlagert werden, kann das gesamte Ausmass der daraus resultierenden Lichtverschiebung kontrolliert werden.

Das Kompensationsschema wird in der Praxis umgesetzt und dann im Bezug auf Frequenzstabilität und -genauigkeit bewertet. Ein optischer Frequenzstandard wird entworfen, gebaut

Zusammenfassung

und getestet. Im Gegensatz zu einem konventionellen Zwei-Photonen-Standard ist dieser mit einem zusätzlichen Milderungsstrahl ausgestattet, dessen Leistung unabhängig von jener des Abfragestrahls kontrolliert werden kann. Die Frequenzinstabilität bei einem Abtastintervall von 1 Sekunde beträgt wenige Anteile pro 10^{13} und mittelt mit längerer Integrationszeit zu wenigen Anteilen pro 10^{15} . Mit dem zusätzlichen Milderungslaser wird eine Verbesserung der Frequenzgenauigkeit erreicht. Die Abhängigkeit der Uhrenfrequenz von der Intensität des Abfragelasers wird dadurch vernachlässigbar. Die Reproduzierbarkeit der Lichtverschiebungsmilderung wird durch Ab- und erneutes Anschalten des Messaufbaus und eine erneute Messung bestätigt.

Zusätzlich wird das Potenzial einer Verbesserung der Frequenzstabilität beurteilt. Mithilfe des Kompensationsschemas wird die Anfälligkeit der Uhrenfrequenz auf Nullpunktverschiebungen der Referenzspannung um mehr als eine Größenordnung verringert. Schliesslich wird ein Ausblick auf mögliche künftige Forschungsrichtungen gegeben.

Die Charakterisierung dieses optischen Frequenzstandards erfordert eine optische Glasfaser-Verbindung. Die Aussagekraft der Messungen muss überprüft werden, da eine fasergeführte optische Frequenz akustisches und thermisches Rauschen aufnimmt. Solche Störeffekte können mit dem sogenannten Doppler-Schema erfasst und kompensiert werden.

Zusätzlich zum Experimentalaufbau zur Lichtverschiebungsmilderung behandelt diese Arbeit theoretisch wie praktisch eine Erweiterung dieses Doppler-Schemas, welche es erlaubt, zwei unabhängige optische Frequenzen gleichzeitig zu übertragen. Dafür werden ein primäres und ein sekundäres Signal in derselben Glasfaser gebündelt. Das Doppler-Schema wird für das primäre Signal umgesetzt. Es wird für das sekundäre Signal aufgezeigt, dass dessen Übertragung durch indirekte Stabilisierung verbessert wird. Bei einem Abtastintervall von 1000 Sekunden wird die Übertragungsstabilität der optischen Frequenz um 16 dB verbessert, wenn die Signale durch Polarisation gebündelt werden. Schliesslich werden praktische Einschränkungen der Methode diskutiert und in einem breiteren Zusammenhang betrachtet.

Stichwörter: Atomuhr, Optischer Frequenzstandard, Rubidium, Zwei-Photonen-Absorptionsspektroskopie, Dynamischer Stark-Effekt, Lichtverschiebung, Milderung der Lichtverschiebung, Optische Frequenzübertragung, Glasfaser-Verbindung.

Samenvatting

Atoomklokken zijn essentieel voor vele moderne toepassingen in wetenschap en technologie. Doordat de frequentie van een lokale oscillator op een elektronische transitie gerefereerd wordt, kunnen passieve optische atoomklokken een ontzettend hoog niveau van frequentiestabiliteit en -nauwkeurigheid bereiken. In de laatste decennia is de wetenschappelijke belangstelling voor elektronische transities in het optisch frequentiespectrum beduidend gegroeid dankzij de uitvinding van de optische frequentiekam. Optische atoomklokken hebben een voordeel ten opzichte van de traditionele microgolfklokken omdat ze van transities met hogere kwaliteitsfactoren gebruik maken, wat tot een verbetering van de korte-termijn frequentiestabiliteit leidt.

De rubidium-twee-foton-klok is een passieve optische atoomklok die de hoge kwaliteitsfactor van een optische transitie combineert met de eenvoud van een warme atomische stoomcel. Daarom is het een veelbelovende technologie voor compacte en geminiaturiseerde klokken en frequentiestandaards. De combinatie van een kleine atomische stoomcel met een optische transitie wordt mogelijk gemaakt door de Doppler-vrije absorptiespectroscopie van een hyperfijne spectrale component met een laserstraal in het nabij infrarode bereik met een golflengte van 778.1 nm.

Het sterkeffect beperkt echter vaak de lange-termijn frequentiestabiliteit van de rubidium-twee-foton-klok. Dit effect overdraagt fluctuaties en drijven van de laserintensiteit op de atomische resonantiefrequentie en daardoor op de klokfrequentie.

Dit proefschrift exploreert een compensatieschema voor het sterkeffect dat gebaseerd is op een verzachtingslaser met een golflengte van 1556.2 nm. De verzachtingslaser schuift de atomische resonantiefrequentie in de tegenovergestelde richting van de laser die de transitie aanspreekt. Doordat de intensiteitsverhouding van de twee stralen aangepast wordt en ze gecombineerd worden om dezelfde atoompopulatie te bereiken, kan de hele omvang van de eruit voortvloeiende sterkeffect gecontroleerd worden.

Het compensatieschema wordt geïmplementeerd en beoordeeld op frequentiestabiliteit en -nauwkeurigheid. Een optische frequentiestandaard wordt ontworpen, gebouwd en getest.

Samenvatting

Deze vertoont, in vergelijking met een conventionele twee-foton-standard, de bijkomende sterkeffect-verzachtingslaser met een golflengte van 1556.2 nm, van welke het vermogen onafhankelijk gecontroleerd kan worden van het vermogen van de laser die de atomen aanspreekt. De frequentieinstabiliteit voor 1 seconde integratietijd wordt gemeten als enkele delen in 10^{13} en gaat omlaag naar enkele delen in 10^{15} voor langere integratietijden. Met de bijkomende verzachtingslaser wordt een verbetering van de frequentienauwkeurigheid aangetoond. De afhankelijkheid van de klokfrequentie van de intensiteit van de laser die de atomen aanspreekt wordt verwaarloosbaar. Twee metingen voordat en nadat de frequentiestandaard uitgeschakeld wordt, tonen aan dat de verzachting van het sterkeffect met deze methode reproduceerbaar is.

Bovendien wordt het potentieel voor een verbetering van de frequentiestabiliteit beoordeeld. Met het verzachtingschema wordt de sensibiliteit van de klokfrequentie voor drijven van de referentiespanning met meer dan een grootteorde verminderd. Tenslotte worden perspectieven gegeven op mogelijke toekomstige onderzoeksrichtingen.

De karakterisering van deze optische frequentiestandaard benodigt een glasvezelverbinding. De betrouwbaarheid van de metingen moet gecontroleerd worden omdat een optische frequentie die over glasvezel overgedragen wordt akoustische en thermische ruis ondergaat. Zulke verstoringen kunnen gedetecteerd en gecompenseerd worden door het zogenoemd Doppler-schema.

Naast de experimentele opbouw voor de verzachting van het sterkeffect wordt zowel theoretisch als praktisch een uitbreiding van het Doppler-schema, die het veroorlooft om twee onafhankelijke optische frequenties gelijktijdig te overdragen, behandeld. Om dit doel te bereiken, worden een primair en een secundair optisch signaal in dezelfde glasvezel gebundeld. Het Doppler-schema wordt voor het primaire signaal geïmplementeerd. Het wordt aangetoond dat de overdraging van het secundaire signaal door indirecte stabilisering verbeterd wordt. Voor een integratietijd van 1 seconde wordt de overdragingsstabiliteit van de optische frequentie van het secundaire signaal met 16 dB verbeterd als de signalen met de polarisatie van het licht gebundeld worden. Uiteindelijk worden praktische beperkingen van de methode besproken en in bredere context geplaatst.

Trefwoorden: Atoomklok, Optische Frequentiestandaard, Rubidium, Twee-Foton-Absorptiespectroscopie, Starkeffect, Verzachting van het Starkeffect, Optische Frequentieoverdraging, Glasvezelverbinding.

Contents

Acknowledgements	i
Abstract	iii
Publications and Conferences	xvii
List of Abbreviations	xix
I Introduction	1
1 Clocks and Time	3
1.1 Time and Frequency	3
1.1.1 The Measurement of Time	3
1.1.2 The Atomic Clock	4
1.1.3 Frequency and Noise	4
1.2 Going Optical	5
1.2.1 The Resonance Quality Factor	5
1.2.2 From Optical to Microwave Frequency	5
1.2.3 The Passive Optical Atomic Clock	7
1.3 Performance Metrics	8
1.3.1 Frequency Accuracy	8
1.3.2 Frequency Stability	8
1.3.3 Size, Weight and Power	9
2 Compact Atomic Clocks	11
2.1 Compact Rubidium Two-Photon Clocks	11
2.2 Alternative Technologies	12
2.2.1 Optical Iodine Clock	12
2.2.2 Pulsed Optically Pumped Rubidium Clock	13
2.2.3 Cold-Atom Ramsey Clocks	14

3	Overview of Thesis Structure	15
II	Theoretical Background	17
4	Rubidium Two-Photon Optical Clock	19
4.1	Two-Photon Transition	19
4.1.1	Atomic Structure	19
4.1.2	Doppler-Free Spectroscopy	21
4.1.3	Transition Linewidth	21
4.1.4	Differences between Isotopes	22
4.2	Frequency Lock	22
4.3	Residual Amplitude Modulation	23
4.4	Alternative Two-Photon Approaches	24
4.4.1	Two-Color Two-Photon Frequency Standard	24
4.4.2	Direct Comb Interrogation	25
4.5	Resonance Frequency Shifts	26
4.5.1	Self-Collision Shift	27
4.5.2	Helium Collision Shift	28
4.5.3	Second-Order Doppler Shift	28
4.5.4	Zeeman Shift	29
4.5.5	Black Body Radiation Shift	29
4.5.6	Line Pulling	29
4.5.7	Gravitational Red Shift	29
5	AC Stark Shift	31
5.1	Physical Origin	31
5.2	Impact on Clock Frequency	31
5.2.1	Sensitivity Coefficient	32
5.3	Overview of Mitigation Approaches	33
5.4	Combined Error Signal	35
5.4.1	Working Principle	35
5.4.2	Error Signal Conditions	35
5.4.3	Linear Combination and Calibration Factor	36
5.4.4	Laser Frequency Noise	37
5.4.5	Intensity Modulation	37
5.4.6	Dual Interrogation	39
5.5	Reduction of Frequency Sensitivity to Power	39
5.5.1	Resonance-Offset Locking	40
5.5.2	Reducing Optical Intensity	40
5.6	Compensation with a Mitigation Beam	41
5.6.1	Concept of a Mitigation Beam	41
5.6.2	Stabilization to the Appropriate Optical Intensity Ratio	43

5.6.3	Application to the Two-Color Two-Photon Standard	44
5.6.4	Application to the Single-Color Two-Photon Standard	45
5.7	Choice of a Mitigation Approach	45
5.7.1	Size, Weight and Power	45
5.7.2	Repeatability	46
5.7.3	Application to an Optical Frequency Standard	47
5.7.4	Selection and Chapter Conclusions	47
6	Optical Fiber Link Stabilization	49
6.1	Indirect Stabilization using Multiplexing	49
6.1.1	Theoretical Compensation Limit	51
III	Experiment	55
7	Optical Fiber Link	57
7.1	Layout Plan	57
7.2	Transfer Stability without Fiber Noise Cancellation	58
7.3	Indirect Stabilization of Optical Frequency Transfer	60
7.3.1	Experimental Setup	60
7.3.2	Frequency Measurements	64
7.3.3	Phase Noise Measurements	66
7.3.4	Configuration for Characterization of the Optical Standard	69
7.3.5	Chapter Conclusions	69
8	Optical Frequency Standard Setup	71
8.1	Fiber Optics Part	73
8.1.1	Clock Laser	73
8.1.2	Pre-Amplifier	73
8.1.3	Power Splitting and Amplification	74
8.2	Atomic Reference	76
8.3	Characterization Setup	78
8.4	Chapter Conclusions	79
9	AC Stark Shift Sensitivity Coefficients	81
9.1	Methodology	81
9.1.1	Measurement Setup	81
9.1.2	Auxiliary Measurements and Calibration	82
9.2	Measurement and Calculation	84
9.2.1	Frequency Response to Intensity Changes	84
9.2.2	Orthogonal Distance Regression	85
9.3	Experimental Observation of Light Shift Compensation	85
9.4	Chapter Conclusions	87

Contents

10 Relative Intensity Stabilization	89
10.1 Practical Implementation	89
10.1.1 Optical Setup	89
10.1.2 Power Stabilization Electronics	91
10.2 Voltage Reference Stability	92
10.2.1 Voltage Reference Stability Measurements	92
10.2.2 Perturbation and Compensation	94
10.3 Temperature Sensitivity of Electronics	95
10.3.1 Empirical Sensitivity Coefficient	96
10.3.2 Frequency Instability Limits	97
10.4 Stability Budget	98
10.5 Chapter Conclusions	100
11 Absolute Frequency	101
11.1 Absolute Frequency Measurement	101
11.1.1 Optical Frequency Domain	101
11.1.2 Radio Frequency Domain	102
11.1.3 Measurement Chain Referenced to UTC	103
11.1.4 Measurement of Clock Laser Frequency	107
11.2 Systematic Resonance Frequency Shifts	107
11.2.1 Self-Collision Shift	107
11.2.2 Helium Collision Shift	109
11.2.3 Second-Order Doppler Shift	113
11.2.4 Zeeman Effect	113
11.2.5 Black Body Radiation Shift	114
11.2.6 Gravitational Red Shift	114
11.3 Accuracy Budget	115
11.3.1 Correction of Measured Clock Frequency	115
11.3.2 Estimation of Residual Light Shift	116
11.4 Comparison to Previously Reported Measurements	116
11.5 Retrace Measurement	117
11.6 Chapter Conclusions	118
IV Conclusion	119
12 Summary of Thesis	121
12.1 Rubidium Two-Photon Clock	121
12.2 Optical Fiber Link	122
13 Outlook and Concluding Thoughts	123
13.1 Rubidium Two-Photon Clock	123
13.2 Optical Fiber Link	124

Bibliography	141
Appendix	143
Science Communication	143
Red, Blue and Green - An Artistic View on the Two-Photon Clock	145
Curriculum Vitae	147

Publications and Conferences

Peer-Reviewed Journal Papers

Published

R. Blum, S. Denis, L. Karlen, S. Kundermann, S. Karlen, and S. Lecomte, “Dual optical frequency transfer through wavelength-division and polarization multiplexing in a 184-meter fiber link,” *Opt. Continuum*, Jun. 2024, doi: 10.1364/OPTCON.516673.

M. Ludwig, F. Ayhan, T.M. Schmidt, T. Wildi, T. Voumard, **R. Blum**, Z. Ye, F. Lei, F. Wildi, F. Pepe et al., “Ultraviolet astronomical spectrograph calibration with laser frequency combs from nanophotonic lithium niobate waveguides,” *Nature Communications*, vol. 15, no. 1, p. 7614, Sep. 2024, doi: 10.1038/s41467-024-51560-x.

Under Review

R. Blum, S. Kundermann, T. Ruelle, S. Lecomte, and S. Karlen, “AC Stark Shift Mitigation for the Rubidium Two-Photon Clock using 1556.2 nm Wavelength,” submitted to *Phys. Rev. Applied*, Jan. 2025.

Industry Journal Paper

Published (in French)

J.-M. Bonard, O. Hog, J. Haesler, T. Ruelle, **R. Blum**, S. Karlen, F. Droz, A. Jallageas, J. Morel, O. Greim, “ROLEX RUBIDIUM OPTICAL ATOMIC CLOCK, une nouvelle horloge atomique optique,” *Journée d’Etude Société Suisse de Chronometrie (SSC)*, vol. 2024-Les artistes du temps, 2024.

International Conferences

Conference Paper

R. Blum, S. Kundermann, T. Ruelle, S. Lecomte, and S. Karlen, “Light shift mitigation for the 5S-5D two-photon transition in rubidium,” in *Quantum Technologies 2024*, F. Baboux, V. D’Auria, and T. Bienaimé, Eds., Strasbourg, France: SPIE, Jun. 2024, p. 55. doi: 10.1117/12.3027257.

Oral Presentations

R. Blum, S. Kundermann, T. Ruelle, S. Lecomte, and S. Karlen, "Rubidium 5S-5D Two-Photon AC Stark Shift Mitigation with 1556.2 nm Beam and Relative Intensity Stabilization," presented at International Conference on Space Optics (ICSO), Antibes Juan-les-Pins, France, Oct. 21, 2024.

R. Blum, S. Kundermann, T. Ruelle, S. Lecomte, and S. Karlen, "Light Shift Mitigation for the Rb Two-Photon Clock Targeting High-Performance Timekeeping in Space," presented at 9th International Colloquium on Scientific and Fundamental Aspects of GNSS, Wrocław, Poland, Sept. 26, 2024.

Poster Presentations

R. Blum, S. Kundermann, T. Ruelle, S. Lecomte, and S. Karlen, "Light Shift Mitigation in a Rubidium Two-Photon Optical Frequency Standard Using a 1556.2 nm Wavelength Beam," presented at the European Frequency and Time Forum (EFTF), Neuchâtel, Switzerland, Jun. 25, 2024.

R. Blum, S. Denis, L. Karlen, S. Kundermann, S. Karlen, and S. Lecomte, "Indirect stabilization of optical frequency transfer over fiber by polarization and wavelength-division multiplexing," presented at the European Frequency and Time Forum (EFTF), Neuchâtel, Switzerland, Jun. 27, 2024.

R. Blum, S. Kundermann, T. Ruelle, S. Lecomte, and S. Karlen, "Light shift mitigation for the 5S-5D two-photon transition in rubidium," presented at SPIE Photonics Europe, Strasbourg, France, Apr. 9, 2024

R. Blum, S. Karlen, S. Kundermann, F. Droz, and S. Lecomte, "A Hot Vapor Optical Clock Targeting Miniature Dimensions With Frequency Instability Below 10^{-13} ," presented at EFTF-IFCS 2022, Paris, France, April 25, 2022.

List of Abbreviations

ADEV	Allan Deviation
AOM	Acousto-Optic Modulator
ASG	Aluminosilicate Glass
CMS	Cladding Mode Stripper
CPL	(Fiber) Coupler
CW	Continuous-Wave (Laser)
DUT	Device Under Test
ECDL	External Cavity Diode Laser
EDFA	Erbium-Doped Fiber Amplifier
EOM	Electro-Optic Modulator
ESA	European Space Agency
FWHM	Full Width at Half Maximum
GNSS	Global Navigation Satellite System
IL	In-Loop
ISO (SS/DS)	Isolator (Single-Stage/Dual-Stage)
LO	Local Oscillator
MUX	Multiplexer
MZI	Mach-Zehnder Interferometer
ND	Neutral Density

List of Abbreviations

NTC	Negative Temperature Coefficient (Thermistor)
OADEV	Overlapping Allan Deviation
OOL	Out-of-Loop
PBS	Polarizing Beam Splitter
PD	Photodiode
PI	Proportional-Integral (Feedback Loop)
PLL	Phase-Locked Loop
PMT	Photo-Multiplier Tube
POP	Pulsed Optically Pumped
PPLN	Periodically Poled Lithium Niobate (Crystal)
RAM	Residual Amplitude Modulation
RF	Radio Frequency
SHG	Second Harmonic Generation
SWaP	Size, Weight and Power
TIA	Trans-Impedance Amplifier
WDM	Wavelength-Division Multiplexer

Introduction **Part I**

1 Clocks and Time

1.1 Time and Frequency

1.1.1 The Measurement of Time

Time has fascinated humans for centuries and has given rise to a variety of ingenious technical solutions to measure it. Timekeeping is an essential pillar of the modern societies we live in. Not only large parts of economy, but also social interactions would look completely different without the broad variety of technological achievements based on the measurement of time.

On the one hand, mastering time is useful for synchronization. People can meet at a predefined moment in time, train crossings can be planned such that collisions are avoided, and in datacenters the loss of data is avoided by precisely synchronizing the internal clocks of many different computers. On the other hand, time measurements allow to detect the interval between two events. We can determine how long a chocolate cake needs to stay in the oven, who has won a ski race, or how long the signals emitted by satellites in space need to travel down to Earth, allowing to locate ourselves with Global Navigation Satellite Systems (GNSS).

Simpler devices, such as sundials and hour glasses, have been used by humans for a long time, but soon reached practical limits. Clocks were invented, improved, and shrunk to evolve into delicate watches. A bit later, they were joined by electronic wristwatches. Whether it concerns a clock-tower mechanism, a mechanical pocketwatch, or a quartz wristwatch, these timekeepers all share a common feature: their heartbeat is the steady vibrations of an *oscillator*. Their pendulum, hairspring and quartz crystal make them capture the flow of time.

However, an oscillator is not enough; a clock must count its vibrations to trace the passing of time. In a mechanical watch, a set of miniature cogwheels reduces the lively vibrations of the hairspring to gentle rotations of the ensemble of second, minute and hour hands, which uncovers the time of day to the educated reader. Such an oscillator is very sensitive to external impacts. Its rate of vibrations is influenced by temperature, magnetic fields, or orientation in space. But some oscillators can be coupled to a robust reference: an atomic reference.

1.1.2 The Atomic Clock

If your watch runs fast or slow, you could bring it to the watchmaker who would then regulate it. The watchmaker would tune its oscillator frequency according to a superior oscillator acting as a reference. But after some time, you would probably notice that your watch again loses or gains time. An atomic clock, in contrast, is different: its oscillator is tuned to the reference with a feedback loop. The incessant feedback makes the regulation continuous; it is as if the atomic clock always had a personal watchmaker on its side.

The superior reference in an atomic clock is defined by an atomic electron transition¹. The difference between two atomic energy levels encodes a well-defined resonance frequency. The electron transition is only possible when an atom is excited with an electromagnetic field matching the atomic resonance frequency. Whether this is the case is determined by *probing* or *interrogating* an atomic population. As an alternative to neutral atoms, single ions, or simple molecules can be probed. The electromagnetic field is provided by an oscillator. To distinguish the atomic reference from the macroscopic oscillator, the latter is referred to as the *local oscillator*. A clock that works as described above is referred to as a *passive atomic clock*.

An atomic reference has at least two key advantages over a macroscopic one. Firstly, as highlighted above, it is less susceptible to external perturbations. And in the long haul, the reference does not change, as unlike macroscopic objects atoms do not age. Secondly, since the atomic structure is identical for all individual atoms of the same isotope, they can act as an universal standard. In this regard, it does not surprise that the definition of the second is set by a feature of the atomic structure of a certain atom and isotope, namely the unperturbed ground-state hyperfine transition frequency of the ¹³³Cs atom [14].

1.1.3 Frequency and Noise

The performance of a passive atomic clock is determined by how well its local oscillator can reproduce the stability of the atomic reference. The signal of an atomic clock can often be described by a sinusoidal function. Unlike a perfect sinus, it suffers from amplitude and phase noise. It can be written as [98]

$$V(t) = V_0[1 + \alpha(t)] \cos [2\pi\nu_0 t + \varphi(t)] \quad (1.1)$$

with V_0 being the amplitude, ν_0 the frequency, $\alpha(t)$ the random fractional amplitude and $\varphi(t)$ the random phase. With regard to an atomic clock, we are mainly interested in phase and frequency rather than in amplitude. The *instantaneous frequency fluctuation* $(\Delta\nu)(t)$ is linked to the random phase $\varphi(t)$ by the definition [98]

$$(\Delta\nu)(t) = \frac{1}{2\pi} \frac{d\varphi(t)}{dt} \quad (1.2)$$

¹Recent progress has been made on clocks that probe a nuclear rather than an electron atomic transition [118]. Nevertheless, as of today the vast majority of atomic clocks is based on electron transitions.

To analyze and compare different clocks to each other, normalization of frequency is useful. To this goal, the *fractional frequency fluctuation* is defined as [98]

$$y(t) = \frac{(\Delta\nu)(t)}{\nu_0} \quad (1.3)$$

While for the performance of an atomic clock, its fractional frequency fluctuations are decisive (see 1.3.2), the atomic resonance frequency as an absolute number can also be of importance. Atomic transitions in different frequency ranges offer advantages and shortcomings. Optical resonance frequencies are an attractive choice for the reasons that are outlined below.

1.2 Going Optical

Atomic clocks can be realized with energy level transitions in different spectral domains. Whereas traditionally, microwave transitions have been favored in research and industry, the last two decades have witnessed a strong push towards optical transitions. An important advantage of optical transitions over their microwave counterparts lies in the so-called quality factor. But the much higher optical frequencies also come with a technical challenge, namely the counting of these very fast oscillations. This challenge has been solved by the *optical frequency comb*, whose invention became the key enabler for optical atomic clocks.

1.2.1 The Resonance Quality Factor

The transition linewidth γ expresses how narrowly the resonance frequency is defined by the atomic structure. It depends on the lifetime of the excited state: the longer it is, the narrower is the linewidth. For an atomic clock, the linewidth of a transition is particularly expressive when put into perspective with the absolute resonance frequency ν_0 . The quantity called quality factor Q expresses this ratio

$$Q = \frac{\nu_0}{\gamma} \quad (1.4)$$

The higher its quality factor, the better an atomic transition is suited for an atomic clock. As it can be seen in Eq. (1.4), one way to increase it, is to have a higher resonance frequency ν_0 . Thanks to their very high resonance frequencies in the order of hundreds of terahertz, optical transitions can achieve extremely high quality factors. Even if a particular optical transition has a larger linewidth than a microwave transition, it has good chances to feature a higher quality factor.

1.2.2 From Optical to Microwave Frequency

In a passive atomic clock, the atomic resonance must be addressed with an oscillator. For the realization of passive optical clocks, suitable optical oscillators are available in the form of

lasers. Light emitted by a laser can be manipulated with ease, both in frequency and amplitude. Matching detectors exist too, such as photodiodes and photomultiplier tubes. With these components, laser frequency can be adjusted to the one of an optical transition. Such a device is known as an *optical frequency standard*. Very low fractional frequency fluctuations $y(t)$ can be achieved by an optical frequency standard. Nevertheless, the high optical frequencies make it impossible to count the laser oscillations directly. Therefore, one of the difficulties in realizing an optical atomic clock lies in the challenge to convey the very low fractional frequency fluctuations in the optical domain to equally low fractional frequency fluctuations in the microwave domain. This challenge can be divided into two parts. Firstly, the optical frequency must be detected. Secondly, a link must be established between the two frequency domains.

Both challenges are solved using an optical frequency comb [30, 48, 49]. An optical frequency can be detected by its difference to another optical frequency, provided that the two frequencies are sufficiently close. To detect their difference, the two frequencies are mixed. Assume two sine waves with similar angular frequencies ω_a and ω_b . Mixing them results in the product of sines, which is

$$\sin(\omega_a t) \cdot \sin(\omega_b t) = \frac{1}{2} \left(\cos((\omega_a - \omega_b)t) - \cos((\omega_a + \omega_b)t) \right) \quad (1.5)$$

With two optical frequencies, the sum term $\omega_a + \omega_b$ in Eq. (1.5) lies outside of the detector bandwidth. The difference term $\omega_a - \omega_b$, in contrast, can be detected if it is sufficiently small.

Following the detection of the optical frequency, its low fractional frequency fluctuations must be transferred to the microwave domain. An optical frequency comb is realized by mode-locking a pulsed laser. The reciprocal value of the time interval between laser pulses is known as the *pulse repetition rate*. In the frequency domain, the optical frequency comb consists of many equally spaced lines according to the equation

$$f_n = n \cdot f_{rep} + f_{CEO} \quad (1.6)$$

with n being the mode number and f_{CEO} the carrier-envelope offset frequency that describes the shift between pulse envelope and optical carrier frequency. According to Eq. (1.6), if f_{CEO} as well as the frequency f_n of mode number n are stable, then the repetition rate f_{rep} is stabilized too.

Detecting and locking f_{CEO} requires an octave-spanning frequency comb allowing for so-called *self-referencing* [57]. The microwave frequency f_{CEO} can be detected by frequency-doubling a part of the comb light and mixing it with the fundamental frequencies. Independently of the mode number n , the process of mixing reveals the frequency difference

$$2 \cdot f_n - f_{2n} = 2(n f_{rep} + f_{CEO}) - (2n f_{rep} + f_{CEO}) = f_{CEO} \quad (1.7)$$

As f_{CEO} can be isolated and detected, it can be locked with a feedback loop. The same is true for f_n , which is mixed with the optical frequency standard. In consequence, f_{rep} is locked as well. It has the same low fractional frequency fluctuations as the optical frequency standard it is referenced to.

1.2.3 The Passive Optical Atomic Clock

A passive optical atomic clock consists of the two elements described above: a passive optical frequency standard and a self-referenced optical frequency comb. The combination of these two elements is illustrated² in Figure 1.1 below. The rubidium two-photon optical clock is

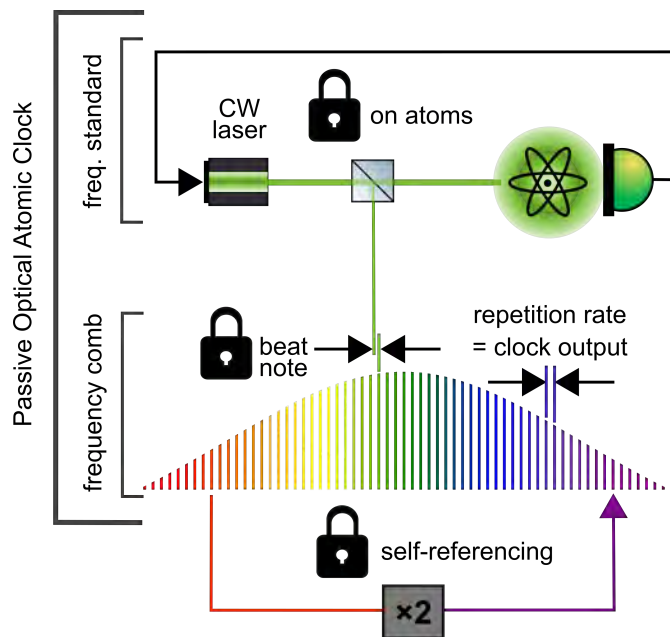


Figure 1.1: Scheme of a passive optical atomic clock. The stability of an optical frequency standard (top) is transferred from the optical to the microwave frequency domain by an optical frequency comb (bottom). CW = continuous-wave (laser).

an example of a passive optical atomic clock. This manuscript treats a rubidium two-photon optical frequency standard. While the frequency stability is not transferred from the optical to the microwave frequency domain, this would be possible with the addition of a self-referenced frequency comb. The frequency standard uses a continuous-wave (CW) laser to address the two-photon transition in rubidium atoms, which are confined in a hot atomic vapor cell.

²For the creation of the illustrations in this thesis featuring optical setups, the author gratefully acknowledges the Inkscape optical component library created by Alexander Franzen: <http://www.gwoptics.org/ComponentLibrary/>

1.3 Performance Metrics

An atomic clock is described by two important frequency characteristics: accuracy and stability. Moreover, for many practical applications it is also relevant how transportable a device is and how much power it consumes.

1.3.1 Frequency Accuracy

Accuracy describes the *degree of conformity of a measured or calculated value to its definition* [69]. Frequency accuracy thus designates the offset of a frequency from a *nominal frequency*. This frequency offset can be given either as an absolute number, or in relative terms as [69]

$$f_{\text{offset}} = \frac{f_{\text{measured}} - f_{\text{nominal}}}{f_{\text{nominal}}} \quad (1.8)$$

Frequency accuracy is particularly important when a clock or frequency standard is used for the realization of the second, the meter or another base unit of the International System of Units (SI).

1.3.2 Frequency Stability

Stability, in contrast, is a measure of *how well an oscillator can produce the same time or frequency offset over a given time interval* [69]. With respect to frequency, the question is by how much the frequency offset changes over time. The mean value of the frequency offset is irrelevant.

In the time domain, the most popular metric for frequency stability is the Allan Deviation (ADEV) [5]. It can be calculated either from phase or frequency data. The Allan Deviation is the square root of the Allan Variance (AVAR). Expressed using fractional frequency fluctuation $y(t)$ (see Eq. 1.3), Allan Variance $\sigma_y^2(\tau)$ is defined as [95]

$$\sigma_y^2(\tau) = \frac{1}{2(M-1)} \sum_{i=1}^{M-1} [y_{i+1} - y_i]^2 \quad (1.9)$$

The AVAR $\sigma_y^2(\tau)$ is calculated over different sampling intervals of length τ , where τ is known as the integration (or averaging) time. Within each sampling interval, M values of fractional frequency fluctuation averages y_i are considered. Strictly speaking, Allan Deviation $\sigma_y(\tau)$ expresses fractional frequency *instability* rather than *stability*.

Besides the classic Allan Variance, also other estimators exist, such as for instance: Overlapping Allan Variance, Modified Allan Variance, Total Variance and Time Variance. Among the listed estimators, in this thesis Overlapping Allan Variance (OAVAR) is used along with the classic AVAR. OAVAR makes better use of the full data set than the classic AVAR. For each

integration time τ , it namely forms all possible samples within the data set. This means that neighboring samples are overlapping with each other. Although these samples are not fully independent, OAVAR improves the confidence of the stability estimate compared to the classic AVAR, resulting in smaller error bars for the same amount of data. For the formulas defining OAVAR for frequency and phase measurements, the reader is referred to [95].

Frequency stability is commonly divided into short-term and long-term stability. Short-term stability usually refers to integration times $\tau < 100$ s, whereas long-term stability is used for $\tau > 100$ s, and in particular for $\tau > 1$ day [69].

The short-term instability of an atomic clock, if detection-noise-limited, follows [24]

$$\sigma_y(\tau) \propto \frac{1}{SNR \cdot Q} \cdot \frac{1}{\sqrt{\tau}} \quad (1.10)$$

with Q the quality factor calculated with the detected linewidth γ (see Eq. (1.4)) and SNR being the signal-to-noise ratio.

The long-term stability, in contrast, is in general limited by other noise sources, and typically by the stability of frequency shifts or drifts. The light shift, which is introduced in chapter 5, is a prominent example of such a noise source affecting long-term frequency stability.

1.3.3 Size, Weight and Power

A metric that gives an indication of how mobile a device is, is summarized under the acronym *SWaP* that stands for *Size, Weight and Power*. The words *Size* and *Power* designate volume and power consumption, respectively. The *SWaP* is given as the product of these three properties and is commonly expressed in units of $\text{cm}^3 \cdot \text{kg} \cdot \text{W}$ [110]. While in principle, also optical lattice [9, 19, 43, 78], ion [21], fountain [39, 45, 55, 56], or other clocks operated in the laboratory could be characterized by their *SWaP*, this metric is generally only meaningful for portable devices.

The required *SWaP* strongly depends on the targeted application. On the low end of the *SWaP* spectrum, we find chip-scale atomic clocks (CSAC) [47, 60, 61] whose *SWaP* can be as low as $10^{-1} \text{cm}^3 \cdot \text{kg} \cdot \text{W}$ [110]. On the other end of the scale, a cornerstone is given by the active hydrogen maser with a *SWaP* of about $10^{10} \text{cm}^3 \cdot \text{kg} \cdot \text{W}$ [110]. Transportable cold-atom clocks [53, 62, 92, 104] fall in the same performance range. At least two models based on magneto-optical trapping and Ramsey interrogation (see 2.2.3) are commercially available. For the moment, however, the active hydrogen maser dominates this market segment.

In an industrial perspective, an additional consideration is the cost of manufacturing. Sometimes the acronym is thus extended to *SWaP·C* by adding the letter *C* for *cost*.

2 Compact Atomic Clocks

The rubidium two-photon clock is a promising technology for both miniature [77, 83] and compact optical clocks and frequency standards. Given that the frequency standard built and tested in this thesis falls in this second category, the discussion of the rubidium two-photon clock and alternative technologies is restricted to compact devices. The following paragraphs give a brief summary of the rubidium two-photon clock regarding performance benchmarks and ongoing efforts to industrialize it. A more extensive discussion of the state of the art follows in chapter 5 and focuses on the topic of light shift mitigation.

2.1 Compact Rubidium Two-Photon Clocks

Compact rubidium two-photon clocks target fractional frequency instability at 1 day of integration time in the 10^{-15} regime [74]. The active hydrogen maser also falls in this range of performance. With its proven reliability, it is nowadays the prevalent technology. However, with a volume of ≈ 400 liters and a weight of ≈ 250 kg [110], it is not suitable for applications where portability and SWaP are paramount.

Experimental realizations of compact clocks and standards have demonstrated the strong potential of the rubidium two-photon technology [3, 65, 74, 84, 90, 91]. Short-term frequency instability lies generally between below $2 \times 10^{-13} / \sqrt{\tau}$ [3, 84] and $5 \times 10^{-13} / \sqrt{\tau}$ [65]. Fractional instability below 10^{-13} has been demonstrated [3, 84], but leads to a trade-off with long-term stability due to the light shift (see chapter 5).

For timekeeping applications, however, long-term frequency stability is vital. At 1 day integration time, drift-removed fractional frequency instability of 5×10^{-15} was shown for experimental realizations of the two-photon clock [65, 74]. While the conventional realization is the single-color two-photon clock, also the two-color two-photon clock (see 4.4.1) has demonstrated similar frequency stability [3].

Industrial developments of the rubidium two-photon clock are under way. At 1 day integration time, fractional and drift-removed instability of 3×10^{-15} was demonstrated for a single-color

two-photon laboratory prototype [99]. A pre-industrial version of the same system was realized in an ensemble of three 19-inch 3U rack-mount chassis and showed a similar performance. Another single-color¹ two-photon clock is already commercially available, but with a higher fractional frequency instability specified to $\leq 5 \times 10^{-15}$ at 1 day integration time.

Also the two-color two-photon clock is being industrialized. A pilot unit² integrated in a single 19-inch 4U rack-mount chassis is available for pre-order. It targets a 3×10^{-15} fractional frequency instability at 1 day integration time.

2.2 Alternative Technologies

A handful of other compact clock technologies also target fractional frequency instability at 1 day integration time in the 10^{-15} regime. Three alternative technologies are presented here. Like the rubidium two-photon clock, they feature a relatively high technology readiness level. Moreover, for the selected technologies, steps have been made towards space qualification. Possible applications are the use as a GNSS satellite on-board clock [10, 54, 71] or onboard a space station [29].

The first technology presented below is based on molecular iodine (I_2). The iodine optical clock, like the rubidium two-photon clock, is a vapor-cell-based passive optical atomic clock. The second technology, the rubidium pulsed optically pumped clock, is a new take on a well-established microwave clock technology. The third technology, the cold-atom Ramsey clock, is also a microwave clock but features a magneto-optical trap. Other technologies not included in this selection are the mercury ion clock [22, 106], the acetylene-based optical clock [32], or the ytterbium cell atomic clock [2]. For a review of more examples of emerging technologies, the reader is referred to [72].

2.2.1 Optical Iodine Clock

The optical iodine clock is a nearly mature technology that has demonstrated fractional frequency instabilities in the lower 10^{-15} regime [97, 101] and below [112]. As a vapor-cell-based passive optical clock, it shares common features with the rubidium two-photon clock. Both clock types need a frequency comb to transfer frequency stability from the optical to the microwave domain. And both technologies require stringent control of the vapor pressure for achieving 10^{-15} fractional frequency instability [74, 97].

The iodine clock is based on modulation-transfer spectroscopy of a rovibronic³ transition in molecular iodine. A pump beam and a probe beam are aligned in a colinear counter-

¹Infleqtion, <https://www.infleqtion.com/tiqker>, webinar video, minute 48.

²QuantX Labs, <https://quantxlabs.com/wp-content/uploads/2024/09/TEMPO.pdf>

³Rotational, vibrational and electronic degrees of freedom interact simultaneously in a molecule.

propagating fashion. In contrast to the rubidium two-photon clock, the laser beams pass the iodine vapor cell multiple times to increase interaction length. The rovibronic transition is at 532 nm wavelength, which means that it can be addressed with a frequency-doubled industry-developed low-noise laser at 1064 nm wavelength. For short integration times, the iodine clock clearly outperforms the active hydrogen maser. At 1 s integration time, fractional frequency instability below 10^{-14} has been demonstrated [101, 112].

The technological readiness of the iodine optical clock is endorsed by the fact that a first commercial model⁴ has recently entered the market. The SWaP of this device is reported to 29 liters, 20 kg, and 80 W ($= 4.6 \times 10^7 \text{ cm}^3 \cdot \text{kg} \cdot \text{W}$). The manufacturer specifies frequency instability to 2.5×10^{-14} at $\tau = 1 \text{ s}$ and 5×10^{-15} at $\tau = 1 \text{ day}$.

Furthermore, the technology is also being developed with regard to space qualification. The German Aerospace Center (DLR) has performed a successful sounding rocket flight with an iodine optical reference aboard [31, 100]. Moreover, DLR plans to launch two iodine optical references and an optical frequency comb to the International Space Station (ISS) in the framework of the COMPASSO mission. The launch is planned for the year 2027 [112] and should provide an in-orbit validation of the clock technology. Finally, together with an industrial partner, DLR is also developing a new iteration of the iodine clock that targets the fulfillment of the stringent requirements of use in GNSS satellites [112].

2.2.2 Pulsed Optically Pumped Rubidium Clock

Like the rubidium two-photon and the iodine clock, the pulsed optically pumped (POP) rubidium clock makes use of a vapor cell. But unlike these two optical atomic clocks, the rubidium POP frequency standard relies on an industry-developed microwave frequency technology [33, 34]. But by preparing the atomic states in a different manner, the frequency stability is further improved.

Traditional rubidium microwave clocks are based on continuous-wave double resonance, where state preparation, interrogation, and detection happen simultaneously. The POP scheme [44, 79] allows to reduce the light shift effect that limits the double resonance scheme. A more than two order of magnitude reduction of the light shift has been demonstrated [44].

By using key elements of a technology that has been studied extensively, the rubidium POP clock reduces technical risks, which is an asset with regard to space applications. An engineering model of the physics package has been manufactured by Leonardo S.p.A., and two instances have passed a formal ESA review process. Moreover, they have successfully undergone environmental and performance testing [44]. The most probable fractional frequency instability after 1 day is reported to 6×10^{-15} . In periods when environmental parameters are sufficiently stable, the potential for instabilities below 10^{-15} was observed [44]. The SWaP of the final prototype is expected to 17 liters, 10 kg and 60 W ($= 1 \times 10^7 \text{ cm}^3 \cdot \text{kg} \cdot \text{W}$).

⁴VectorAtomic, VA EG-30, <https://vectoratomic.com/>

2.2.3 Cold-Atom Ramsey Clocks

Cold-atom Ramsey clocks probe a microwave transition in caesium [81] or rubidium [20, 29] atoms, which are given by the ground state hyperfine splitting. The operation principle is commonly divided into four steps [81], namely cooling and trapping, state preparation, interrogation and detection. At the beginning of the first phase, atoms are loaded into a magneto-optical trap. While being trapped with coils, they are laser-cooled and repumped with two different lasers. In the subsequent step of state preparation, the trapping coils are turned off along with the repumping and cooling lasers. The repumping laser is switched off shortly before the cooling laser in order to prepare the atoms in the ground state for the following interrogation step. In this phase, the atomic cloud freely expands in the microwave cavity. The Ramsey method [94] is applied using two temporally separated microwave pulses that interrogate the clock transition. In the final detection phase, a fluorescence signal is detected by turning on the cooling laser addressing the atoms in the excited state of the microwave clock transition. An error signal is derived that serves to correct the local oscillator frequency.

A commercial model⁵ with a frequency instability of 2×10^{-15} at $\tau = 1$ day has been developed. Instability at 1 second integration time is specified to $\leq 4 \times 10^{-13}$. With about 680 liters, 135 kg and 200 W ($= 1.8 \times 10^{10} \text{ cm}^3 \cdot \text{kg} \cdot \text{W}$), it has a SWaP no smaller than the one of an active hydrogen maser. However, it has very good frequency accuracy specified to a few 10^{-15} .

Also a more compact and transportable model⁶ is commercially available from another manufacturer. Fractional frequency instability is specified to about 3×10^{-15} at $\tau = 1$ day, while at 1 second it is specified to $\leq 7 \times 10^{-13}$. With approximately 40 liters, 31 kg and 80 W ($= 1 \times 10^8 \text{ cm}^3 \cdot \text{kg} \cdot \text{W}$), it offers a much lower SWaP than the above-mentioned cold-atom clock.

⁵ μ QUANS, MuClock, <https://www.muquans.com/product/muclock/>

⁶SpectraDynamics, cRb-Clock, <https://spectradynamics.com/products/crb-clock/>

3 Overview of Thesis Structure

The remainder of this thesis is composed of three parts: Theoretical Background, Experiment, and Conclusion.

The Theoretical Background part starts by outlining the working principle of the rubidium two-photon clock in chapter 4. Following the discussion of the two-photon clock, chapter 5 focuses on the AC Stark effect (light shift). It analyses the state of the art of light shift mitigation for the rubidium two photon-clock and motivates the choice of an experimental approach. Finally, as an optical fiber link is required to characterize the optical frequency standard built in this thesis, chapter 6 explains the basis of fiber link stabilization for optical frequency transfer. Moreover, a method is suggested to combine two optical frequencies in the same fiber and stabilize the transfer of both frequencies simultaneously.

The Experiment part then starts in chapter 7 with the practical implementation and experimental validation of the fiber link stabilization with two optical frequencies. The following chapter 8 presents the design of the rubidium two-photon optical frequency standard featuring a mitigation laser at 1556.2 nm wavelength. In addition, it describes how the frequency standard is characterized using an optical reference. Chapter 9 then uses the described setup to measure the AC Stark shift sensitivity coefficients at 778.1 nm and 1556.2 nm wavelength. It also presents a proof-of-concept demonstration validating the technical feasibility of the selected mitigation approach. The approach is then implemented in a complete system and evaluated in chapter 10. Potential technical limitations are quantified and the capability of the system to compensate the effect of an external perturbation is tested. The focus of this chapter lies on frequency stability, whereas the following and concluding chapter 11 investigates frequency accuracy. A measurement of the optical transition frequency is presented and dominant sources of systematic frequency shifts are discussed.

Finally, the Conclusion part is composed of two chapters. Chapter 12 summarizes the key findings of the Experiment part for both the rubidium two-photon optical standard and the optical fiber link. The final chapter 13 puts these findings into context and provides an outlook on future research directions.

Theoretical Background **Part II**

4 Rubidium Two-Photon Optical Clock

This chapter presents the working principle of the rubidium two-photon clock. It starts by discussing the 5S-5D two-photon transitions in rubidium and how they can be addressed using Doppler-free spectroscopy. It is then described how the clock laser (local oscillator) is modulated and locked on the atomic transition. The chapter continues by briefly discussing two alternative two-photon architectures, namely two-color and direct comb interrogation. Finally, different phenomena shifting the resonance frequency of the two-photon transition are presented.

4.1 Two-Photon Transition

4.1.1 Atomic Structure

Rubidium, just like caesium, is an alkali metal. A single electron is located on its outermost shell. With rubidium having 37 electrons, this is the fifth shell. From its $5S_{1/2}$ ground state, the electron can reach different higher states by absorbing one or multiple photons. Single-photon transitions are for example $5S_{1/2} \rightarrow 5P_{1/2}$ and $5S_{1/2} \rightarrow 5P_{3/2}$ referred to as the D1 and D2 lines, respectively [103]. Possible two-photon transitions are $5S_{1/2} \rightarrow 5D_{3/2}$, $5S_{1/2} \rightarrow 5D_{5/2}$, and $5S_{1/2} \rightarrow 7S_{1/2}$.

For the application to a frequency standard, the most attractive one is the $5S_{1/2} \rightarrow 5D_{5/2}$ two-photon transition. Compared to other two-photon transitions and for a given interrogation beam intensity, it provides the highest fluorescence signal amplitude. Its energy level diagram is shown in Figure 4.1.

The thick dashed horizontal line in Figure 4.1 is in the exact middle between the $5S_{1/2}$ ground and the $5D_{5/2}$ excited state. It marks the intermediate virtual state of the two-photon transition. Its spacing from either ground or excited state represents the energy of a photon with 778.1 nm wavelength. Two photons at this wavelength can excite an electron from the ground to the excited state. From the excited $5D_{5/2}$ state, a part of the electrons will first decay to the $6P_{3/2}$

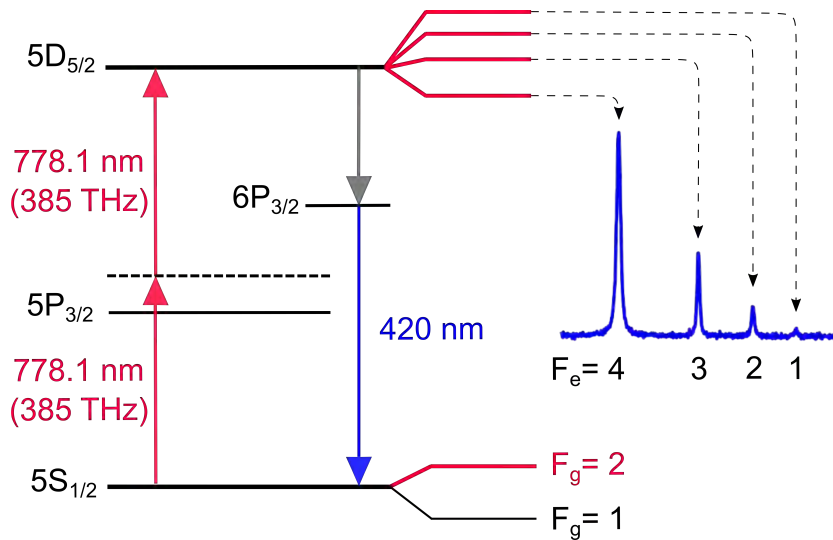


Figure 4.1: Fine (left) and hyperfine (right) structures of the $5S_{1/2} \rightarrow 5D_{5/2}$ two-photon transition. The hyperfine structure is plotted for ^{87}Rb along with a recorded fluorescence spectrum for the hyperfine components $F_g = 2 \rightarrow F_e = 4, 3, 2, 1$ in blue.

and then from there back to the $5S_{1/2}$ ground state. On this decay path, fluorescence photons with 420 nm wavelength are emitted. In a conventional two-photon clock, this fluorescence is detected as it indicates that the clock laser is resonant with the atomic transition.

The excitation of the two-photon transition is possible thanks to the vicinity of the virtual state to the real $5P_{3/2}$ state. The smaller the spacing is between the two, the higher is the transition rate and thus the fluorescence rate. Unfortunately, only the $5D \rightarrow 6P \rightarrow 5S$ decay path contributes to the 420 nm fluorescence. But from both the $5D_{5/2}$ and $6P_{3/2}$ states, the electrons can decay to other lower states not depicted in Figure 4.1. A look at the so-called branching ratios reported by [50] shows that only 35% of the electrons in the $5D_{5/2}$ state decay to the $6P_{3/2}$ state, from which again only 31% decay to the $5S_{1/2}$ ground state. Therefore, about one out of ten electrons in the excited state gives rise to a detectable photon at 420 nm wavelength. And according to more recently reported branching ratios [8], as little as one out of 14 excited electrons contributes to the 420 nm fluorescence. Alternatively, the 776 nm wavelength fluorescence arising from the $5D_{5/2} \rightarrow 5P_{3/2}$ decay can be detected, which has been tested in experiment [11]. A much larger fraction of 67% of the electrons in the excited state generates this fluorescence.

The sought-after features of the two-photon transition are hidden in its hyperfine structure. The one of the isotope ^{87}Rb is plotted on the right hand side of Figure 4.1. When exciting the two-photon transition with a single laser beam, the hyperfine structure is covered by the thermal motion of the atoms. This effect is known as Doppler broadening. However, when the transition is addressed using a Doppler-free spectroscopy method, the hyperfine structure can be resolved and appears as the blue fluorescence spectrum in Figure 4.1.

4.1.2 Doppler-Free Spectroscopy

Consider a laser beam propagating along the z -axis. It is directed through a hot atomic vapor cell filled with rubidium atoms. A photon from this beam encounters an atom within the rubidium vapor. In the perspective of the atom, the photon frequency is shifted, unless the velocity component of the atom along the z -axis is zero ($v_z = 0$). In consequence, for all atoms having $v_z \neq 0$, the atomic resonance condition is shifted. Still in the perspective of the atom, a photon with energy $\hbar\omega$ has the Doppler-shifted energy $\hbar\omega(1 \pm v_z/c)$. As the thermal motion of the atoms follows a Gaussian distribution, the hyperfine structure of the two-photon transition is covered by a background of the same shape.

To avoid this Doppler background, two major methods have been developed: saturation absorption [93] and two-photon spectroscopy [23]. In saturated absorption spectroscopy, only the atoms at rest ($v_z = 0$) contribute to the signal. For two-photon spectroscopy, in contrast, there is no selection of atoms with respect to their velocity component along the z -axis. Two-photon spectroscopy can thus achieve a higher signal-to-noise ratio than saturated absorption spectroscopy [105].

A two-photon transition can be excited with a pair of photons that travel both along the z -axis but in opposite directions. The resonance condition [16] is

$$\hbar\omega_{ge} = \hbar\omega \left(1 - \frac{v_z}{c}\right) + \hbar\omega \left(1 + \frac{v_z}{c}\right) = 2\hbar\omega \quad (4.1)$$

with $\hbar\omega_{ge}$ the energy difference between the $5S_{1/2}$ ground and the $5D_{5/2}$ excited state. Eq. (4.1) is fulfilled independently of v_z , which means that all velocity classes of atoms can potentially contribute to the fluorescence signal.

Two counter-propagating beams can be obtained by placing a mirror behind the vapor cell and aligning the incoming laser beam such that its reflection propagates back on the same axis. However, also in this configuration some atoms absorb two slightly off-resonance photons coming from the same side. Therefore, a small residual Gaussian background remains. Nevertheless, the hyperfine structure can usually be clearly distinguished.

4.1.3 Transition Linewidth

The hyperfine structure consists of multiple peaks with a Lorentzian lineshape. The linewidth γ of the strongest hyperfine component, which is measured as the full width at half maximum (FWHM), determines the quality factor of the resonance. The natural transition linewidth is given by the lifetime of the $5D_{5/2}$ state ($\tau_{5D_{5/2}} = 238$ ns [102]). This corresponds to a linewidth of $1/(2\pi \cdot \tau_{5D_{5/2}}) = 660$ kHz for the transition between the ground and the excited state. In the perspective of one photon with its 385 THz frequency, this is 330 kHz. This results in a theoretical quality factor of $Q \approx 1.1 \times 10^9$.

In practice, however, the measured quality factor is always lower than the theoretical one since the measured linewidth is broadened by different effects. A distinction is made between homogeneous and inhomogeneous broadening. Dominant effects are transit-time broadening [15] and broadening due to atom collisions. Many phenomena that shift the atomic resonance frequency also lead to a broadening of the linewidth.

4.1.4 Differences between Isotopes

Rubidium naturally occurs as two isotopes: ^{85}Rb and ^{87}Rb . With a relative natural abundance of 27.8%, ^{87}Rb is more rare than ^{85}Rb with 72.2% [103]. With respect to the transition in question, ^{87}Rb has an advantage over ^{85}Rb with its larger spectral spacing of hyperfine components. For ^{85}Rb , the relevant peak-to-peak spacing is approximately 4.7 MHz¹, whereas for ^{87}Rb it is larger with 14.4 MHz² [85].

Due to the finite spectral spacing between peaks, the tails of the individual line shapes interfere with the ones of their neighboring peaks. In consequence, the different transition lines are pulled together, which is why this effect is known as *line pulling* (see 4.5.6). The further they are apart, the less two neighboring peaks affect each other when their linewidths are broadened. Another risk of closely spaced hyperfine components is that the clock laser would lose its lock and subsequently re-lock on a neighboring peak, which would result in a large jump of clock frequency.

In addition, the relative intensity of the strongest hyperfine component of ^{87}Rb is higher than the one of ^{85}Rb . The difference is small with 37.5% vs. 30.6% for ^{87}Rb and ^{85}Rb , respectively³. For the two reasons explained above, a cell filled with isotopically enriched ^{87}Rb is used.

4.2 Frequency Lock

The frequency of the clock laser (local oscillator) is locked to the strongest hyperfine component of the two-photon transition in ^{87}Rb , namely $(F_g=2) \rightarrow (F_e=4)$. This is achieved through frequency modulation of the clock laser and synchronous detection of the fluorescence signal. A detailed description of the different setup components is given in chapter 8.

The laser frequency can be modulated either directly via its injection current [65] or using an external phase modulator [74]. In the experiments presented here, an electro-optic modulator (EOM) is used. It is driven by a voltage signal with amplitude V_{rf} and frequency f_m . The fluorescence signal is detected with a photomultiplier tube (PMT). Its photocurrent is

¹ $(F_g=3) \rightarrow (F_e=5)$ vs. $(F_g=3) \rightarrow (F_e=4)$

² $(F_g=2) \rightarrow (F_e=4)$ vs. $(F_g=2) \rightarrow (F_e=3)$

³ The indicated percentages represent the intensity of the ^{87}Rb $(F_g=2) \rightarrow (F_e=4)$ and ^{85}Rb $(F_g=3) \rightarrow (F_e=5)$ hyperfine components with respect to the total intensity of all possible hyperfine components of the $5S_{1/2} \rightarrow 5D_{5/2}$ transition for the respective isotope [85].

amplified and converted to voltage using a transimpedance amplifier (TIA). The TIA signal is then demodulated at f_m (synchronous detection) with a demodulator low-pass filter set to a cut-off frequency around $f_m/5$. This results in an anti-symmetric error signal which has its zero-crossings at the local maximum of the fluorescence signal. Finally, the error signal is supplied to a proportional-integral (PI) feedback loop. The resulting control signal is applied on the clock laser injection current in order to keep its frequency referenced to the two-photon transition.

As a passive frequency standard, the rubidium two-photon clock is affected by intermodulation noise [7]. The frequency noise of the free-running clock laser at twice the modulation frequency $S_{\Delta\nu}(2f_m)$ is transferred to the locked laser. With integration time τ , clock laser frequency f_0 and modulation frequency f_m , frequency instability in terms of Allan Deviation is limited to [7]

$$\sigma_y(\tau) = \sqrt{\frac{S_{\Delta\nu}(2f_m)}{f_0^2} \frac{1}{2\sqrt{\tau}}} \quad (4.2)$$

Depending on the fluorescence detection rate, either the shot noise or the intermodulation noise sets a limit to short-term frequency stability. Therefore, when choosing a laser, it is advisable to pay attention to its frequency noise specifications. Lasers available for 1556.2 nm wavelength generally have more attractive frequency noise properties than options for 778.1 nm wavelength.

4.3 Residual Amplitude Modulation

As outlined above, an EOM is used as a phase modulator. It consists of a birefringent crystal, which has an ordinary and an extraordinary optical axis. For simplicity, the distinction between the axes is omitted here. For a more detailed description, the reader is referred to [111]. Modulation depth is proportional to V_{rf} . The modulation is assumed sinusoidal with angular modulation frequency $\omega_m = 2\pi \cdot f_m$. The modulator introduces a time-dependent phase shift $\phi(t)$ in function of the wavelength λ that is composed of three parts

$$\phi(t) = \phi_0 + \phi_{dc} + \delta \sin(\omega_m t) \quad (4.3)$$

which are

$$\phi_0 = \frac{2\pi l}{\lambda} n \quad (4.4)$$

accounting for the phase shift of the crystal as such,

$$\phi_{dc} = -\frac{\pi l}{\lambda d} n^3 r \cdot V_{dc} \quad (4.5)$$

accounting for the contribution of the bias voltage V_{dc} applied to the EOM, and

$$\delta = -\frac{\pi l}{\lambda d} n^3 r \cdot V_{rf} \quad (4.6)$$

expressing the effect of the AC modulation. The crystal is characterized by its length l , height d , refractive index n and electro-optic coefficient r . Finally, the EOM is typically specified by the voltage V_π that induces a phase shift of π .

While the ideal case would be a pure phase modulation, residual amplitude modulation (RAM) is observed in practice. By adding an offset to the error signal, RAM can affect the lock point. Unless this offset is constant over time, RAM thus introduces clock frequency fluctuations. However, RAM can be detected and suppressed by controlling V_{dc} [120].

4.4 Alternative Two-Photon Approaches

The working principle outlined in the paragraphs above describes the conventional single-color two-photon frequency standard. It is a relatively simple system with one CW laser. However, by exciting the two-photon transition with a single wavelength, the transition rate is quite low (see 4.1.1). Moreover, an optical frequency comb is needed to transfer the stability of the CW laser from the optical to the radio frequency domain. As possible alternatives to the conventional single-color method, the two-color two-photon architecture [2, 3, 42, 88, 89] and direct comb interrogation [37, 107, 119] have emerged. Both of these approaches are briefly discussed below.

4.4.1 Two-Color Two-Photon Frequency Standard

Rather than with two photons at the same wavelength, two-color two-photon interrogation excites the atomic transition with one photon at about 780 nm and another one at around 776 nm wavelength. By employing two different wavelengths, two-color architectures can massively increase the number of emitted fluorescence photons. However, this advantage comes at the expense of a more complex setup, residual Doppler broadening, and a larger AC Stark shift sensitivity.

With two resonant photons at 778.1 nm wavelength, the virtual intermediate state is blue-detuned from the real $5P_{3/2}$ state by about 1 THz frequency, which in wavelength corresponds to 2 nm. The two-color concept is based on the observation that through a smaller detuning from the real $5P_{3/2}$ state, much higher transition rates are achieved than in the single-color case. The detuning referred to as Δ can be chosen arbitrarily by working with two different wavelengths. This is illustrated in the energy diagram in Figure 4.2.

By reducing Δ , the atomic transition rate is increased, meaning the absorption cross-section gets larger. For example, when the 780 nm laser is red-detuned from the $5P_{3/2}$ state by as little

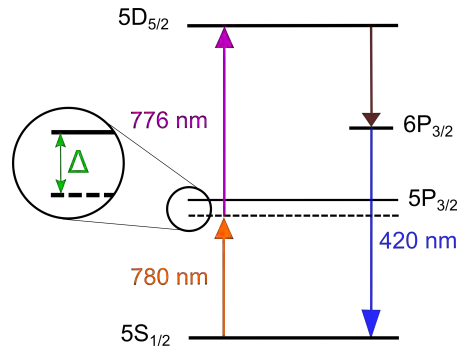


Figure 4.2: Energy diagram showcasing a two-color two-photon scheme with its small virtual state detuning Δ from the real $5P_{3/2}$ state. In this example, the detuning is negative ($\Delta < 0$), but it can be chosen arbitrarily.

as 1.5 GHz, the transition rate is increased by about a hundred thousand times compared to the single-color case [88]. Therefore, short-term frequency stability is improved.

However, the difference in wavelength between the two beams generates residual Doppler broadening. The single-photon natural linewidth of 330 kHz is broadened by approximately 1.5 MHz assuming 90°C cell temperature [88]. In consequence, the quality factor decreases. Nevertheless, the much larger gain in photon detection outweighs the effect of residual Doppler broadening with regard to short-term frequency stability. Finally, a stable frequency output in the optical domain is achieved with sum-frequency generation. As a summary, the principal differences between the single-color and two-color schemes are recapitulated in Table 4.1 below.

Property	Single-color	Two-color
Photon wavelength(s)	$2 \times 778.1 \text{ nm}$	$780 + 776 \text{ nm}$
Stabilized frequency	single-photon frequency	sum frequency
Light shift magnitude	smaller but given	larger but selectable
Sign of light shift	negative	complementary
Doppler broadening	1 st order Doppler free	a few MHz

Table 4.1: Comparative table highlighting key characteristics of single-color and two-color two-photon clocks and standards.

4.4.2 Direct Comb Interrogation

As another alternative to the conventional interrogation scheme featuring a CW laser combined with a self-referenced frequency comb, an architecture known as *direct comb interrogation* has been investigated [37, 107, 119]. In this architecture, the comb lines interrogate the two-photon transition directly. The approach has similarities with two-color interrogation discussed above. As illustrated in Figure 4.3, multiple pairs of comb lines can have a

sum-frequency which is resonant with the two-photon transition. Like the single pair of wavelengths in two-color two-photon interrogation, they cause a small residual Doppler shift. The advantage of this approach is that no CW laser is required. A major difficulty, however,

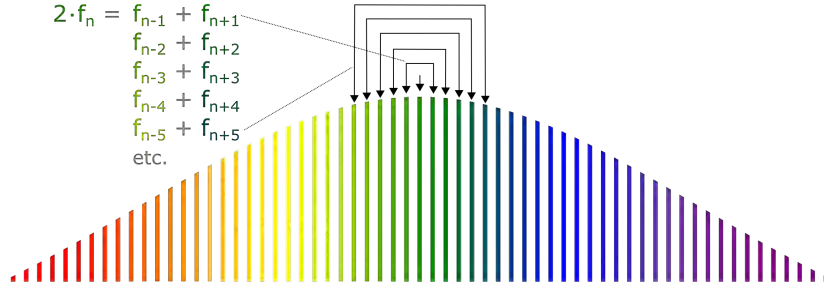


Figure 4.3: The basis of direct comb interrogation: multiple pairs of wavelengths are resonant with the two-photon transition.

is to engineer a suitable optical pulse overlap in the vapor cell. Promising results have been achieved recently [37] with fractional frequency instabilities around 10^{-14} for sufficiently long integration times.

4.5 Resonance Frequency Shifts

A variety of physical phenomena shift the $5S_{1/2} \rightarrow 5D_{5/2}$ resonance frequency. Figure 4.4 gives a classification of the most important effects. By measuring sensitivity coefficients, stability requirements can be found for different operational parameters linked to these effects. Moreover, together with the working point of an operational parameter, the sensitivity coefficients allow to determine the systematic frequency shifts that an individual clock or frequency standard is subject to. A summary of sensitivity coefficients reported in literature is given in Table 4.2. Along with the coefficients, a stability requirement is given for achieving a clock fractional frequency instability of 1 part in 10^{15} .

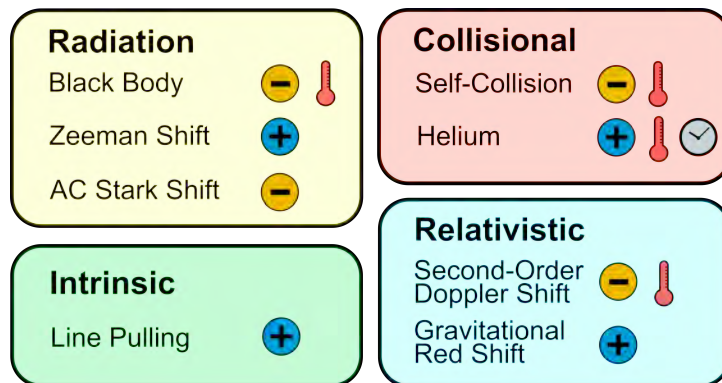


Figure 4.4: Overview of different resonance frequency shifts. An icon indicates the sign of the frequency sensitivity. Temperature dependent phenomena are highlighted with a thermometer icon, whereas a watch dial stands for dependence on operational history.

Shift	Coefficient	Requirement for 10^{-15}	Reference
Self-Collision Shift	$-5 \times 10^{-13}/\text{K}$	2 mK	[83]
Helium Collision Shift	$5.5 \times 10^{-9}/\text{Torr}$	200 nTorr	[83]
Second-Order Doppler Shift	$-1 \times 10^{-15}/\text{K}$	1 K	[83]
Zeeman Shift	$6.5 \times 10^{-11}/\text{G}^2$	3.9 mG = 390 nT	[74]
Black Body Radiation Shift	$-1.3 \times 10^{-15}/\text{K}$	770 mK	[74]

Table 4.2: Summary of sensitivity coefficients reported in literature. Values are indicated in fractional clock frequency and for a vapor cell temperature of 100°C. Not included in the table are the effects of line pulling and gravitational red shift (see Figure 4.4) since they do not depend on operational parameters and are moreover negligible for clock frequency considerations.

Frequency shifts can be positive or negative. Whereas their signs are insignificant for stability, they are primordial for considerations regarding accuracy. Some physical effects which require particular attention with respect to frequency stability are also major contributors to systematic frequency shifts affecting accuracy. These are namely the AC Stark shift, the self-collision shift and the helium collision shift. The AC Stark effect will be treated separately in chapter 5, whereas the other relevant effects are discussed below.

4.5.1 Self-Collision Shift

Collisions between rubidium atoms give rise to both a resonance frequency shift and transition linewidth broadening [117]. This so-called self-collision shift (or temperature shift) is proportional to vapor pressure, whereas the latter is an exponential function of cell temperature. Higher cell temperatures therefore not only lead to a higher systematic shift, but also to a greater sensitivity coefficient. For high cell temperatures around 100°C, tight control of vapor cell temperature is required to avoid adverse impacts on long-term frequency stability [74].

The rubidium vapor pressure P_V in Torr is a function of temperature T (in Kelvin) and is given by [4]⁴

$$\log_{10} P_V = 2.881 + 4.312 - \frac{4040}{T} \quad (4.7)$$

For the ^{85}Rb isotope, the self-collision shift rate was measured to [117]

$$Z_{am} \gamma_{S,Rb} = -13.5(\pm 1) \text{ MHz/Torr} \quad (4.8)$$

Note that the rate given here is converted to a basis of 385 THz frequency. It thus indicates the frequency shift of one 778.1 nm wavelength photon, whereas in the original reference [117] it is given for ω_{ge} the frequency difference between the $5S_{1/2}$ and $5D_{5/2}$ states.

For ^{87}Rb , a similar shift rate was measured [84] as for ^{85}Rb [117]. Nevertheless, also for ^{87}Rb an approximately two times higher rate was reported [74].

⁴Valid for the liquid phase. To obtain the vapor pressure in atm instead of Torr, omit the term 2.881.

4.5.2 Helium Collision Shift

Helium is known to permeate glass due to its small atomic radius [28, 96]. This is also the case with the Pyrex glass vapor cell used in this thesis. Sapphire coatings can help reduce the permeation rate [25]. The total frequency shift is proportional to the helium partial pressure inside the vapor cell. The temperature of the vapor cell determines the permeation constant of the material and thus the instantaneous helium leak rate. Like the self-collision shift, the helium collision shift can pose a limit to frequency stability. But unlike the former, helium permeation in general results in a quasi-linear frequency drift that can be corrected for.

Besides a frequency shift, helium permeation causes broadening of the transition. Although unfavorable for short-term stability, this property can be exploited to estimate the helium concentration in the atomic vapor cell. Both the broadening and the shift rate were measured for the $^{85}\text{Rb } 5S_{1/2} \rightarrow 5D_{5/2}$ two-photon transition [117]. As for the self-collision shift rate, here they are converted to units reflecting the frequency shift of a photon with 778.1 nm wavelength. This conversion results in

$$Z^{am} \cdot \gamma_{B,He} = 25.6(\pm 0.4) \text{ MHz/Torr} \quad (4.9)$$

and

$$Z^{am} \cdot \gamma_{S,He} = +1.03(\pm 0.04) \text{ MHz/Torr} \quad (4.10)$$

for the broadening and shift rates, respectively. Besides helium, also other gases such as argon, krypton, xenon or nitrogen cause shifts and broadening [117]. Helium as the smallest noble gas, however, is generally the main concern.

4.5.3 Second-Order Doppler Shift

The second-order Doppler shift (or relativistic shift) has its origin in the motion of the rubidium atoms and depends thus on cell temperature. As special relativity states, the atom in its higher energy (excited) state has a slightly higher mass than in its ground state. Given that momentum is conserved during the atomic transition, the velocity of the atom must be lower in the excited than in the ground state. This indicates that a small portion of the kinetic energy of the atom, together with the energy of the two photons, has been expended to allow the transition. This leads to a change in resonance condition. The small kinetic energy contribution of the atom lowers the allowed photon energy and thus the resonance frequency. Expressed as an equation, the effect of the relativistic shift on resonance frequency reads [23]

$$2\omega \simeq \omega_{ge} \sqrt{1 - \frac{v^2}{c^2}} \simeq \omega_{ge} \left(1 - \frac{v^2}{2c^2}\right) \quad (4.11)$$

with ω being the photon (angular) frequency, ω_{ge} the (angular) frequency difference between ground and excited states, c the speed of light in vacuum and v the velocity of the atom. The

relativistic shift depends on the square of the atomic velocity, which explains why it is also referred to as second-order Doppler shift.

4.5.4 Zeeman Shift

Magnetic fields are known to cause a resonance frequency shift on the rubidium $5S_{1/2} \rightarrow 5D_{5/2}$ transition through the Zeeman effect. The Zeeman sensitivity coefficient of the rubidium two-photon transition was measured and reported to [74]

$$\delta_{Zeeman} = +1.1 \times 10^{-10} / G^2 \quad (4.12)$$

for the isotope ^{87}Rb and expressed in fractional frequency. To protect the vapor cell from magnetic fields, it is covered with a single-layer mu-metal shielding.

4.5.5 Black Body Radiation Shift

Similar to the Stark shift, the black body radiation emitted by the vapor cell assembly induces a shift of the ground and excited energy levels. Among others, [51] and [75] calculated the black body radiation shift for the two-photon transition. It is of similar magnitude as the second-order Doppler shift. And as the latter, it is of much greater practical relevance to considerations regarding accuracy than stability.

4.5.6 Line Pulling

As outlined in 4.1.4, the individual hyperfine Lorentzian peaks are pulled together due to their spectral vicinity. This effect, however, is small in comparison to other phenomena considered here. For ^{87}Rb its magnitude was calculated to as little as 30 mHz [74] for an spectrum without broadening.

4.5.7 Gravitational Red Shift

As stated by general relativity, time evolves more slowly in a deeper gravitational potential. Near the surface of the Earth, the relative frequency change is about 1.1×10^{-16} per meter of altitude difference [78]. For a system that does not move during measurement, the gravitational red shift is irrelevant. For accuracy considerations, however, it must be accounted for by calculating it for the altitude where the system is operated at.

As mentioned above, the AC Stark effect is the source of a dominant systematic frequency shift that is not discussed above. However, the following chapter is entirely dedicated to the AC Stark shift and its mitigation.

5 AC Stark Shift

This chapter starts by giving a short description of the physical origin of the AC Stark shift and its magnitude in a single-color rubidium two-photon clock. The state of the art of light shift mitigation techniques is discussed. Different approaches are classified, evaluated and contextualized. Finally, based on these considerations, a mitigation approach is selected, namely the one of a 1556.2 nm wavelength mitigation laser.

5.1 Physical Origin

The AC Stark effect describes an optically induced shift of energy levels. Its magnitude depends on light intensity. Therefore, the term *light shift* is a common synonym. The shifting of energy levels results in a detuning of the resonance frequency. The origin of the phenomenon lies in virtual transitions between real states that are caused by non-resonant light. While the $5P_{3/2}$ real intermediate state is essential for the rubidium $5S_{1/2} \rightarrow 5D_{5/2}$ two-photon transition, its presence also leads to a dominant contribution to the light shift. But also other neighboring states contribute. As two-photon transitions rely on the presence of such real states in the proximity of the virtual intermediate ones, it can be argued that the light shift is intrinsic to these transitions [68].

5.2 Impact on Clock Frequency

Both the ground and the excited state are shifted by the AC Stark effect. The atomic polarizability α describes how susceptible a state is to an optical field with angular frequency ω . Its calculation accounts for the transitions which have resonance frequencies close to ω . The closer the resonance frequency of the virtual transition is to ω , the stronger is its impact on α . The atomic polarizabilities for the rubidium $5S_{1/2} \rightarrow 5D_{5/2}$ transition were calculated by [75].

Only the differential shift between the two states is relevant to the atomic resonance frequency. The resonance frequency shift is proportional to the differential atomic polarizability $\Delta\alpha(\omega)$,

which is the difference between the atomic polarizabilities of the excited and ground states. The optical frequency shift is written as [75]

$$\delta\nu(r, z) = \frac{\Delta\alpha}{2c\epsilon_0 h} \cdot I(r, z) \quad (5.1)$$

with $I(r, z)$ being the optical intensity in function of r and z , which are the respective coordinates of radial distance from and position along the optical propagation axis, c the speed of light in vacuum, ϵ_0 the permittivity of free space, and h Planck's constant.

5.2.1 Sensitivity Coefficient

For experimental studies, Eq. (5.1) can be simplified. The product of fundamental constants and differential atomic polarizability is grouped as

$$k(\lambda) \equiv \frac{\Delta\alpha}{2c\epsilon_0 h} \quad (5.2)$$

Assuming a Gaussian beam profile, intensity is averaged over the beam cross-section to

$$I_0 = \frac{P}{\pi w_0^2} \quad (5.3)$$

with P being the optical power of the beam and w_0 its $1/e^2$ intensity radius. Owing to the relatively weak transition rate of the two-photon transition, photon absorption in the atomic vapor is negligible with respect to the intensity of the laser beam. The beam intensity can be considered constant along the propagation axis z . These two simplifications allow to rewrite Eq. (5.1) as

$$\delta\nu = k(\lambda) \cdot I_0 \quad (5.4)$$

The quantity $k(\lambda)$ in Hz/(mW/mm²) is in the following referred to as the *AC Stark shift sensitivity coefficient*. For a two-photon clock, it is a function of λ_{laser} , which is the wavelength of the interrogation laser. Since it is locked to the two-photon transition, we have $\lambda=778.1$ nm.

Based on the above-mentioned differential polarizability calculation, the AC Stark shift sensitivity coefficient for 778.1 nm wavelength was calculated and reported to [75]

$$^{calc} k_{778} = -178.5 \text{ Hz}/(\text{mW}/\text{mm}^2) \quad (5.5)$$

Assuming a 1 mm beam diameter ($2w_0 = 1$ mm), the fractional clock frequency sensitivity is $6 \times 10^{-13}/\text{mW}$. Optical power must thus be stabilized at the μW level to achieve fractional frequency instabilities as low as 10^{-15} . This represents a big technical challenge. Therefore, a light shift mitigation scheme that relieves this constraint would be highly desirable.

The next section discusses and classifies different light shift mitigation methods. First, a literature overview presents approaches that have been suggested and tested. Second, an approach is chosen for experimental studies, namely the one of a 1556.2 nm wavelength mitigation laser. The technical implementation of this approach is then explained in chapter 8.

5.3 Overview of Mitigation Approaches

Since the AC Stark shift is an intrinsic feature of the two-photon transition, the question is how to reduce its impact on both frequency accuracy and stability. A simple answer is to focus on stability while accepting the quantifiable inaccuracy contribution caused by the interrogation beam. Until recently, this was the only approach put in practice, either by stabilizing the interrogation beam intensity as tightly as possible [76] or by additionally massively increasing the beam diameter such that the optical power sensitivity becomes very small [65]. There are good reasons to adopt this strategy. Above all, this allows to maintain the comparatively low complexity of the system. However, as long as the light shift is not compensated as such, a trade-off between short-term and long-term stability exists. The more the short-term stability is boosted by increasing optical power, the more constraining the relative optical power stability becomes for longer integration times. Mitigation of the overall light shift is thus preferable over limiting its adverse effects.

Unlike the strategies described above, which *limit* the impact of the AC Stark effect, a more rigorous approach would cancel or *mitigate* the light shift. In this manuscript the term *light shift mitigation* refers exclusively to methods whose target it is to compensate the atomic resonance frequency shift caused by interrogating the two-photon transition. The ultimate goal of light shift mitigation is to improve both stability and accuracy.

A very relevant observation is that the light shift is proportional to optical intensity (see Eq. (5.1)). This proportionality does not entail alignment and beam shape instabilities. Nonetheless, any mitigation scheme can exploit this property of linearity. By extrapolating the resonance frequency shift to zero optical power, an estimation of the light-shift-unperturbed atomic resonance frequency ν_0 is made. The LO frequency can then be adjusted such that it matches ν_0 . The different methods presented below share the fundamental concept of detection, extrapolation and compensation. A classification of these techniques is given in Figure 5.1 below.

The fundamental question of light shift mitigation is how the LO frequency can be corrected such that it matches the unperturbed atomic resonance frequency ν_0 ¹. One possibility is to adjust the error signal such that the LO is locked to the frequency where ν_0 is suspected. This option is chosen by the two methods on the left hand side in Figure 5.1. In this case, the LO is locked to a frequency which is shifted from the zero crossing of a conventional error signal described in 4.2. The LO signal could also be split into two portions, one of which would

¹In case a frequency-doubled 192 THz oscillator is used for interrogation, this statement considers the doubled LO frequency instead.

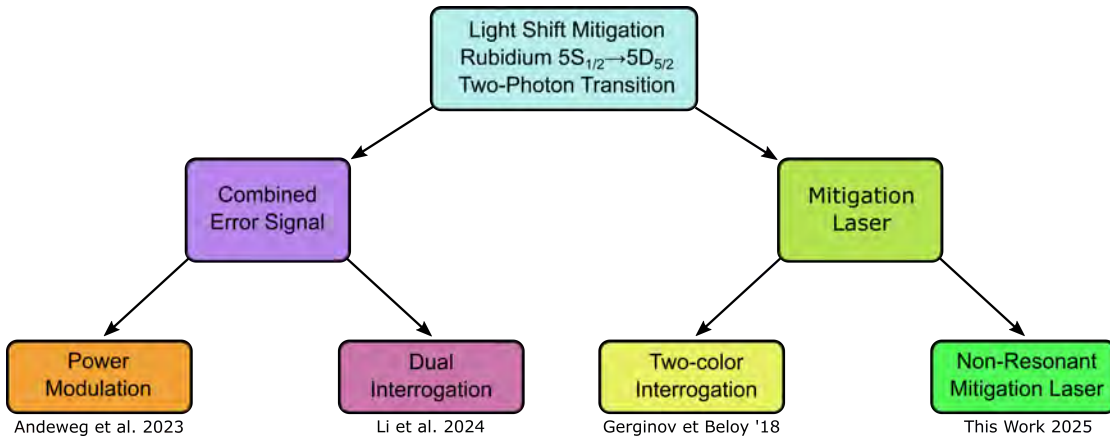


Figure 5.1: Classification of experimentally demonstrated mitigation approaches for the $5S_{1/2} \rightarrow 5D_{5/2}$ two-photon transition in rubidium. The four methods below are discussed in the following paragraphs (from left to right) in 5.4.5, 5.4.6, 5.6.3 and 5.6.4, respectively. Literature references: Andeweg et al. 2023 [6], Li et al. 2024 [67], Gerginov et Beloy 2018 [42].

subsequently be frequency-shifted using a modulator. This would allow to keep the LO at the frequency for which maximum fluorescence amplitude is observed. At the same time, an additional shift is introduced to reproduce the unperturbed atomic resonance frequency. The theoretical framework for the practical implementation of the two above-mentioned approaches was suggested by [116]. The schemes that act on the error signal and that shift the LO frequency with a modulator are referred to as combined error signal (CES) and auto-compensation of shift (ACS), respectively. Whereas the latter has been implemented in a caesium microcell atomic clock based on coherent population trapping [1], the former has been adapted and implemented in rubidium two-photon standards in two different ways. One of these implementations is based on power modulation [6] and the other one on dual interrogation [67].

An entirely different approach is to shift the atomic resonance frequency by controlling the properties of optical fields that interact with the atomic population. Two laser wavelengths can be chosen such that their qualitative effect on resonance frequency is mutually opposite. This principle forms the basis for the two approaches on the right hand side of Figure 5.1. One of these approaches makes use of the two-color two-photon interrogation presented in 4.4.1. The other method adds an additional optical field that is not involved in the interrogation of the clock transition but affects its resonance frequency.

The following paragraphs cover the above-mentioned concepts, starting with the combined error signal approaches in 5.4. Then a short excursus on the reduction of frequency sensitivity to optical power follows in 5.5, before light shift compensation using a mitigation laser is outlined in 5.6. Finally, in 5.7 an approach is selected for implementation.

5.4 Combined Error Signal

The combined error signal (CES) approach [115, 116] is applicable to different types of atomic clocks. Two CES-inspired implementations have been reported for the rubidium two-photon transition. These are namely a power-modulation-based technique [6], and a dual interrogation method [67].

5.4.1 Working Principle

The combined error signal approach relies on the circumstance that a sufficiently large and deliberate change in optical intensity manifests itself in the atomic response, in particular the error signal. On the one hand, the slope of the error signal increases with increasing interrogation power. For the two-photon transition, this effect is due to the quadratic dependence of fluorescence amplitude on laser intensity. On the other hand, the AC Stark effect shifts the zero-crossing of the error signal along the frequency axis. The two mentioned effects are illustrated in Figure 5.2 for the specific case of the two-photon fluorescence signal.

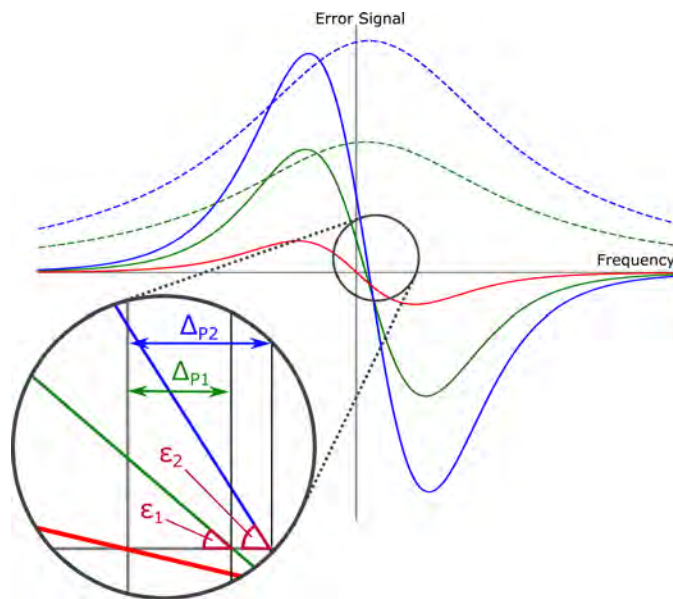


Figure 5.2: Working principle of the combined error signal (CES) approach. Illustration for two signals with higher (blue) and lower (green) optical power. Horizontal axis: frequency, vertical axis: fluorescence (dashed lines) and corresponding error signals (solid lines). The appropriate linear combination (red line) yields a zero-crossing in the origin, where the unperturbed resonance frequency ν_0 is found.

5.4.2 Error Signal Conditions

The practical implementation of CES requires only little hardware. Nonetheless, a set of mathematical conditions must be met [114]. The first necessary condition is that the light

shift Δ_P is proportional to the laser power P

$$\Delta_P = \Delta\nu = c \cdot P \quad (5.6)$$

with c being the light shift coefficient in Hz/mW. The latter can be determined empirically by measuring the clock frequency sensitivity to laser power.

Secondly, the slope of the error signal must follow a so-called pure power-law dependence on optical power. This condition is expressed as follows

$$\tan(\varepsilon) = b \cdot P^\alpha \quad (5.7)$$

Here, $\tan(\varepsilon)$ is the slope of the error signal, which is highlighted in the inset of Figure 5.2, α is an arbitrary exponent, and b is an arbitrary scaling factor.

The third condition is that the atomic transition linewidth γ is much larger than the light shift

$$\gamma \gg \Delta_P \quad (5.8)$$

This last condition assures that a linear approximation is possible around zero. In practice, Eq. (5.8) can be fulfilled with ease. The total light shift of the interrogation laser is generally in the order of a few kHz, whereas the natural transition linewidth γ is 330 kHz (see 4.1.3).

5.4.3 Linear Combination and Calibration Factor

Thanks to the linear approximation around the origin and the two conditions given in Eqs. (5.7) and (5.8), simple algebra allows to combine the genuine error signals $S_{P_1}(\delta)$ and $S_{P_2}(\delta)$. They are joined such that the resulting combined error signal $S_{CES}(\delta)$ equals zero at $\delta = 0$ and nowhere else. One of the genuine error signals is scaled by a calibration factor β and then subtracted from the other one. The appropriate value of β places the zero crossing of the combined error signal into the origin. The combined error signal is thus

$$S_{CES}(\delta) = S_{P_1}(\delta) - \beta \cdot S_{P_2}(\delta) \quad (5.9)$$

As illustrated in Figure 5.2, the desired combined error signal (red) is a linear combination of the two single error signals (green and blue). A possible solution is the difference between the unity-weighted first error signal and the β -weighted second error signal. The calibration factor β is thus nothing else than the ratio between the y-axis intercepts of the two single error signals. It is calculated with the slopes and x-axis intercepts of the straight lines that approximate the two single error signals around the origin. Assuming $P_2 > P_1$ and knowing that the light shift is proportional to P , the ratio between the x-axis intercepts of S_{P_2} and S_{P_1} equals $\frac{P_2}{P_1} > 1$. Finally, by multiplying the ratio of x-axis intercepts $\frac{P_2}{P_1}$ by the ratio of slopes $\frac{\tan \varepsilon_2}{\tan \varepsilon_1}$, it becomes apparent that the ratio of y-axis intercepts between S_{P_2} and S_{P_1} is equal to $(\frac{P_2}{P_1})^{\alpha+1}$. In order to scale the two error signals such that their y-axis intercepts are equal, the

signal S_{P_2} is thus divided by the ratio of their unscaled y-axis intercepts. From this results the calibration factor

$$\beta = \left(\frac{P_1}{P_2} \right)^{\alpha+1} \quad (5.10)$$

As mentioned above, in the two-photon case involving the detection of a fluorescence signal, we have $\alpha = 2$, because the latter scales quadratically with the interrogation laser intensity [24]. From this property, it follows that the theoretical calibration factor in a two-photon system is

$$\beta = \left(\frac{P_1}{P_2} \right)^3 \quad (5.11)$$

With two predefined interrogation powers P_1 and P_2 , the CES method yields a combined error signal S_{CES} that permits to lock the clock laser frequency to the unperturbed atomic transition frequency.

5.4.4 Laser Frequency Noise

In practice, the initial theoretical description of the CES method [115] was found to overlook the impact of laser frequency noise within a modulation cycle [67]. With a discrete change between two optical power regimes, the feedback on the LO frequency would be comparatively slow. Therefore, frequency stability at short integration times would be dominated by the free-running laser frequency noise, which would degrade frequency stability compared to a lock with a much faster feedback. Two different approaches that address this problem have been reported. One possibility described in 5.4.5 consists in continuous rather than discrete power modulation [6]. Another concept outlined in 5.4.6 employs spatial separation of the two different power regimes [67]. The separation is achieved by doubling the atomic vapor cell. Both atomic populations are interrogated simultaneously with a beam stemming from the same laser source, but at different power levels.

5.4.5 Intensity Modulation

Continuous intensity modulation [6] was demonstrated using synchronous detection with a special reference signal. As illustrated in Figure 5.3, optical power was periodically modulated between two extrema. Amplitude modulation was performed with an AOM generating a sine wave at a 2 kHz modulation frequency. At the same time, the LO was frequency-modulated at 100 kHz using an EOM. Since optical intensity fluctuates between an upper and a lower bound defined by the modulation depth, so does the slope of the error signal. As shown in the discussion of CES, appropriate scaling renders its y-axis intercept independent of optical power. Since the error signal is obtained by synchronous detection of the frequency-modulated LO frequency, the latter must be adapted accordingly. A special reference signal is multiplied with the fluorescence signal for demodulation. The reported reference signal

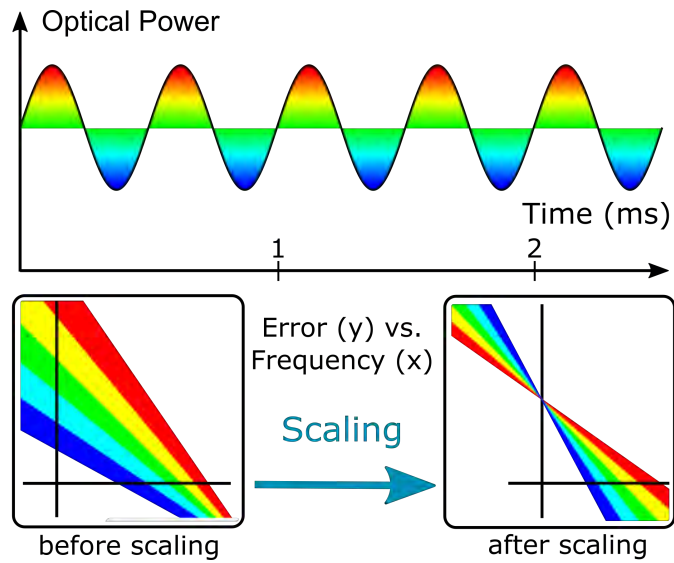


Figure 5.3: Illustration of sinusoidal optical power modulation [6] and error signal scaling for implementing the CES method. Optical power of a single interrogation laser is modulated periodically at a few kHz modulation frequency (top). This results in a continuous frequency shifting and amplitude resizing of the error signal (bottom left). By scaling the error signal with the appropriate reference signal, it is resized such that the light-shift-unperturbed atomic resonance frequency is detected (bottom right).

namely consists of a 100 kHz sinusoidal carrier signal whose envelope is scaled by the inverse cube of the instantaneous laser intensity. Mixing and low-pass filtering the fluorescence with this special reference results in the desired error signal.

In the reported architecture, two lock-ins are intertwined: a fast one and a slow one. The fast one at 100 kHz ensures the LO frequency lock to the atomic transition. In contrast to the conventional frequency lock to the fluorescence maximum (see 4.2), an offset is applied with respect to the fluorescence maximum. The slow lock-in at 2 kHz controls the lock point by adjusting that offset. If the error signal of the slow lock-in is zero, the LO is locked to the frequency at which the AC-Stark-shift unperturbed resonance is suspected.

The described light shift mitigation scheme was tested with a sudden step in laser power which would generate a shift of 14 kHz without mitigation. Using intensity modulation, however, the system stabilized to a clock frequency shifted by 500 Hz from the mean frequency preceding the power step. This corresponds to an extinction factor of 11.5 dB. This figure of merit was achieved after a transition period lasting more than a minute. The servo loop namely takes some time to respond and causes an overshoot of several tens of kHz in clock frequency. The authors see the potential of the technology in clocks with minimized footprint. As this approach requires only little hardware, it could find applications in miniature two-photon standards and clocks.

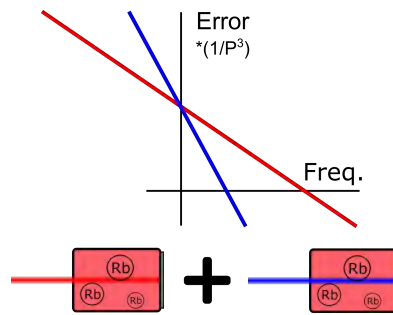


Figure 5.4: Graphical illustration of the dual interrogation method [67] taking advantage of two atomic vapor cells (bottom) that are interrogated simultaneously with a higher (red beam) and a lower (blue beam) optical intensity. By scaling the error signals accordingly (top), they have the same amplitude at the clock frequency for which zero light shift is suspected.

5.4.6 Dual Interrogation

In the approach coined dual interrogation [67], the differentiation between light shift regimes is not made temporally but spatially. As mentioned above, two distinct vapor cells are operated simultaneously. Two beams which are derived from the same laser source interrogate the atomic populations in these cells. However, since they differ in intensity, the associated error signals have different slopes. A combined error signal is obtained from the two individual ones, which are accessible at the same time. The coefficient β is calibrated by measuring optical power in front of both vapor cells and processing the acquired data in a field-programmable gate array.

To demonstrate light shift mitigation, the described system was tested by slowly modulating the laser power reaching one of the cells. Frequency was measured both with and without mitigation. While the ADEV for mitigated operation did not exactly follow a $1/\sqrt{\tau}$ trend, frequency was more stable. For an integration time of 100 seconds, the dual-interrogation method achieved a 10-dB compensation of the introduced perturbation. The authors point out that the repeatability of the method should be investigated in further detail, in particular concerning the electronics and power monitoring

5.5 Reduction of Frequency Sensitivity to Power

Before discussing the concept of the mitigation laser, two methods shall be described that reduce clock frequency sensitivity to optical power. Firstly, an offset locking technique inspired by CES has been reported [66]. Secondly, the beam waist radius represents a design parameter that can be leveraged to reduce the magnitude of the light shift. Both of these approaches are applicable to single-color rubidium two-photon standards and clocks. But since they do not improve frequency accuracy, they are not considered light shift mitigation techniques according to the definition given above (see 5.3). Nevertheless, they can potentially improve frequency stability by relieving the technical constraints on interrogation power stability.

5.5.1 Resonance-Offset Locking

As outlined in the discussion of CES in 5.4, a change in optical power not only impacts the resonance frequency offset, but also the amplitude of the atomic response. The error signal is thus affected by both a shift in its zero-crossing and a change of slope. In the usual case where the LO frequency is locked onto the fluorescence maximum, only the shift of the zero-crossing manifests itself in the LO frequency. However, if the LO frequency is offset-locked to an appropriately selected working point, both effects cancel out. This so-called *resonance-offset locking* method was tested in experiment and found to reduce frequency sensitivity to interrogation power [66]. In the following, its theoretical background shall be outlined.

With the linear approximation of the error signal around its zero crossing, the optical frequency shift $\Delta\nu$ can be described as a function of the error signal slope $\tan \varepsilon$ and the atomic response amplitude $V = \tan \varepsilon \cdot cP$. When introducing a deliberate and constant lock-point offset V_{offset} that is subtracted from the atomic response, optical frequency as a function of interrogation power P is expressed as follows

$$\Delta\nu(P) = \frac{V - V_{offset}}{\tan \varepsilon(P)} = \frac{\tan \varepsilon(P) \cdot cP - V_{offset}}{\tan \varepsilon(P)} \quad (5.12)$$

The optical frequency shift $\Delta\nu$ and the error signal slope $\tan \varepsilon$ have been defined previously in Eqs. (5.6) and (5.7), respectively. The constant offset V_{offset} must be chosen such that the first-order sensitivity of optical frequency ν to interrogation power P is zero, meaning

$$0 \equiv \frac{d\Delta\nu}{dP} = \frac{d}{dP} \left(\frac{bP^\alpha \cdot cP - V_{offset}}{bP^\alpha} \right) = c + V_{offset} \cdot \frac{\alpha}{b} \cdot P^{-\alpha-1} \quad (5.13)$$

Rearranging Eq. (5.13) results in the desired expression for the constant atomic response offset

$$V_{offset} = -\frac{b \cdot c}{\alpha} \cdot P^{\alpha+1} \quad (5.14)$$

Offset-locking to this value eliminates the frequency sensitivity to optical power in the first order. The same mechanism applies to the self-collision shift.

5.5.2 Reducing Optical Intensity

The interrogation laser intensity can be reduced by choosing a larger beam profile, which decreases the magnitude of the light shift. But at the same time, reduced intensity also results in decreased fluorescence photon density and thus degrades short-term frequency stability. Nevertheless, if a larger beam profile is combined with higher laser power, the overall AC Stark shift is reduced without compromising on short-term stability, which is demonstrated below.

Assume a first beam with optical power P_0 and waist radius w_0 , and a second beam with optical power $P_a = a \cdot P_0$ and waist radius $w_0^a = a \cdot w_0$, where $a > 1$ is an arbitrary real number.

The fluorescence amplitude F is proportional to the beam surface area πw^2 and to the square of optical intensity I^2 . The ratio of fluorescence amplitude between the two beams is therefore

$$\frac{F_a}{F_0} = \left(\frac{\pi w_a^2}{\pi w_0^2} \right) \cdot \frac{I_a^2}{I_0^2} = (a^2) \cdot \frac{\frac{P_a^2}{(\pi w_a^2)^2}}{\frac{P_0^2}{(\pi w_0^2)^2}} = (a^2) \cdot \frac{a^2}{a^4} = 1 \quad (5.15)$$

The same shot-noise-limited short-term stability is thus expected for both beams.

The light shift reduction is proportional to the intensity ratio of the two investigated beams, namely

$$\frac{\Delta\nu_a}{\Delta\nu_0} = \frac{I_a}{I_0} = \frac{\frac{a P_0}{\pi a^2 w_0^2}}{\frac{P_0}{\pi w_0^2}} = \frac{1}{a} \quad (5.16)$$

In contrast to the number of detected fluorescence photons, the light shift is reduced by the scaling factor a . Therefore, increasing beam waist and optical power by the same factor reduces the total light shift while maintaining short-term stability at the same level.

The illustrated principle is applied by [65] to drastically reduce the overall light shift to as little as $-183(\pm 55)$ Hz or about 5×10^{-13} in fractional terms. The drawback is that the beam profile is enlarged so much that the interrogation beam path length in the atomic vapor must be extended to collect enough photons. This is done in [65] by employing not only one but two vapor cells that are each 50 mm long.

5.6 Compensation with a Mitigation Beam

5.6.1 Concept of a Mitigation Beam

In contrast to the combined error signal techniques discussed above, approaches involving a mitigation beam are strongly based on hardware. Most importantly, two laser beams of different wavelength are required.

Assuming that the two laser beams address the same population of atoms, the resonance frequency shift can be expressed as

$$\Delta\nu = k_A \cdot I_A + k_B \cdot I_B \quad (5.17)$$

where I_A and I_B stand for the beam intensities, and k_A and k_B for the AC Stark shift sensitivity coefficients. Note that $\frac{k_A}{k_B} < 0$, meaning the two sensitivity coefficients must have opposite signs. By choosing the wavelengths such that they induce shifts of opposite sign, $\Delta\nu$ can

be brought to zero. In consequence, the LO frequency can reflect the AC Stark unperturbed resonance frequency. This situation is achieved when the ratio of intensities fulfills

$$\frac{I_A}{I_B} = -\frac{k_B}{k_A} \quad (5.18)$$

Put differently, the ratio of sensitivity coefficients defines the ratio of optical intensities required to achieve zero net light shift.

Accuracy

The working principle of a mitigation beam can be imagined as a balance scale such as the one depicted in Figure 5.5. The size of the weights in Figure 5.5 stands for optical power or intensity, whereas their distance from the pivot in the center represents the magnitude of the AC Stark shift sensitivity coefficients. The fact that the weights are placed on either side expresses the opposite sign of the coefficients. When the balance scale is in equilibrium, the clock is accurate. Unless a mitigation laser is used, there is no possible counterweight; a clock with a single beam is per se inaccurate.

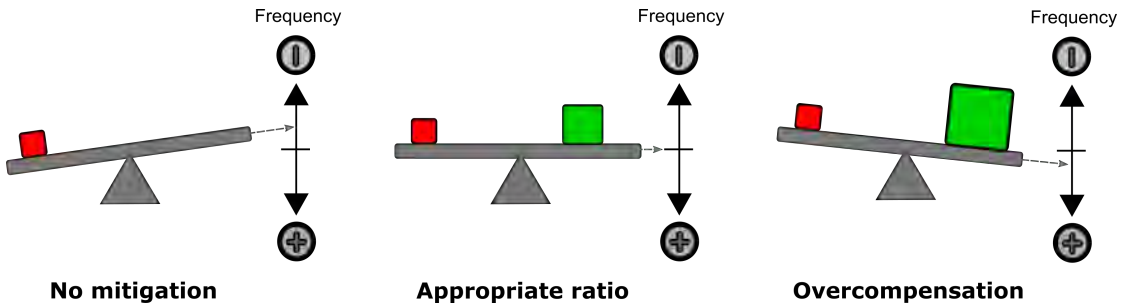


Figure 5.5: Impact of a mitigation laser on frequency accuracy illustrated by the analogy to a balance scale. The tilt angle reflects the atomic resonance frequency offset, whereas the weights and their positions stand for optical intensity and magnitude of the AC Stark shift sensitivity coefficient, respectively. A system featuring only an interrogation laser (red weight, left) is per se inaccurate. The addition of a mitigation laser (green weight, middle) can bring the scale to equilibrium. However, if the mitigation laser intensity is too high (right), this can lead to an overcompensation of the light shift.

Stability

In the picture of the balance scale, frequency stability is represented by the degree to which a given inclination angle stays constant over time. If interrogation power, beam profile and alignment were perfectly constant, frequency stability would be unaffected. Whereas for a single interrogation laser, the light shift impact on stability is dictated by the degree to which intensity fluctuates in absolute terms, for the mitigation laser case the impact on stability depends on the relative stability of the two intensities with respect to each other. Two different strategies to stabilize the optical intensity ratio are presented below in 5.6.2.

5.6.2 Stabilization to the Appropriate Optical Intensity Ratio

Static Intensities

With static intensities, the power of each laser beam is stabilized to a constant value. The power ratio depends on the beam profiles and is chosen such that Eq. (5.18) is fulfilled. Since it is static, this configuration cannot detect the residual light shift during operation. Nevertheless, it can present various advantages over single-laser power stabilization. Firstly, the two power stabilization circuits can share the same voltage reference. Given that the error signal used for power stabilization is obtained by comparing a voltage signal to a reference, a drift in reference voltage causes a drift of the power setpoint and thus a drift in clock frequency. However, if two power stabilization electronic circuits share the same reference, drifts do not impact the ratio of power setpoints. Secondly, the use of two power stabilization units can provide a higher degree of commonality. For instance, supposing that the photocurrent of the photodiode is converted to voltage using a transimpedance amplifier, gain fluctuations can impact the detected voltage and thus optical power. Such gains fluctuations could for example be driven by temperature changes that impact the resistivity of the resistors defining the electronic gain. Thirdly, two beams that share a common path could increase the degree of commonality regarding the optical alignment.

Dynamic Intensities

Alternatively, both beams can be amplitude-modulated together while maintaining a constant intensity ratio between them. For the two-color two-photon standard, common intensity modulation of both beams in combination with synchronous detection of the introduced frequency shift was initially suggested by [42]. A similar principle was explored recently for the single-color two-photon standard [38].

The error signal of the atomic frequency lock reveals information about resonance frequency shifts caused by the amplitude modulation. If the error signal is independent of total optical intensity, this indicates that the overall light shift is zero. This is illustrated in Figure 5.6. When the power of either beam is modulated (left and middle), the atomic frequency response reflects the presence of the light shift. If both beams are modulated with the same modulation depth (right), the frequency response is zero, which indicates that the light shift is compensated. Such a dynamic light shift detection scheme would allow to adjust the intensity ratio continuously.

For the two-photon two-color standard, this concept was demonstrated as a proof of principle. However, rather than a single, two separate acousto-optic modulators were used for applying the same depth amplitude modulation on both wavelengths. An atomic error signal was obtained by demodulating at the amplitude modulation frequency. In the proof-of-concept demonstration, either modulation was switched off separately. This led to an observable change of error signal sign. When both modulations were applied, the error signal fluctuated

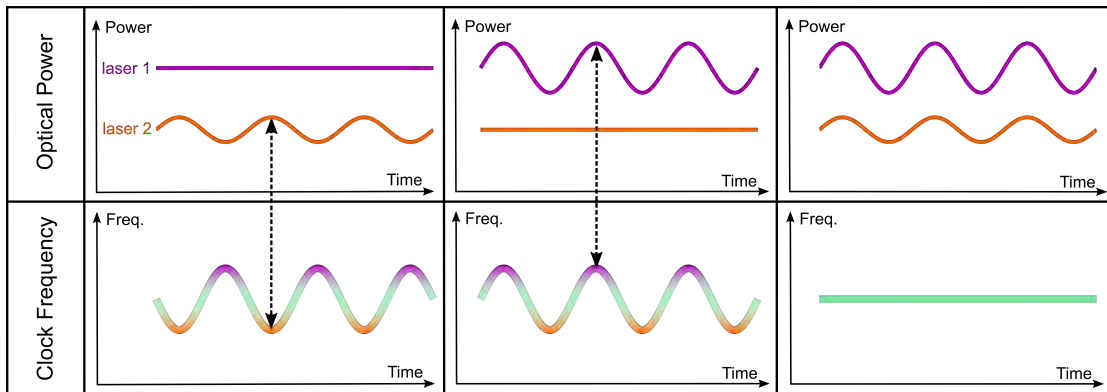


Figure 5.6: Graphical representation of light shift detection through power modulation of two laser beams (laser 1 and laser 2) with opposite AC Stark shift sensitivity coefficients and tuned to the intensity ratio cancelling the light shift. Top half: optical power, bottom half: clock frequency response. In the left and middle third of the figure, optical power is modulated only for laser 2 and laser 1, respectively. In the right third, however, the power of both lasers is modulated with the same modulation depth. As they are tuned to the intensity ratio that cancels the light shift, the clock frequency stays constant.

around zero. Similarly, when the total intensity of 776 nm light was changed, the sign of the error signal was inverted. The error signal obtained in this demonstration had insufficient signal-to-noise ratio. With two lasers having both typical free-running linewidths around 100 kHz, a SNR below 5 was obtained using an amplitude modulation frequency of 200 Hz. The authors expected to improve the SNR by choosing a lower modulation frequency and lasers with more favorable noise properties.

A crucial point in such a dynamic approach is that the same relative modulation depth is applied on both beams. This condition must be met for two independent beams that differ not only in wavelength, but also in optical power. If the relative modulation depths differ, the applied amplitude excursions do not represent the overall intensity ratio, and the point of zero net light shift is not detected correctly.

5.6.3 Application to the Two-Color Two-Photon Standard

The two-color two-photon standard (see 4.4.1) can be leveraged to implement light shift compensation with the mitigation beam approach. In contrast to the single-color case, the two wavelengths are mutually dependent. The intermediate state detuning Δ not only has an influence on the transition rate but also on sign and magnitude of the light shift. Hence, it can be chosen such that the sensitivity coefficients of the two wavelengths fulfill Eq. (5.17).

The 780 nm laser can either be blue [42] or red detuned [86, 88, 89] from the $5P_{3/2}$ state. The choice of Δ is not only guided by the light shift, but also by temperature shifts [86]. Finally, the choice of wavelengths also impacts the magnitude of the residual Doppler broadening.

5.6.4 Application to the Single-Color Two-Photon Standard

The use of a non-resonant mitigation beam was suggested by Martin et al. [75]. Such a mitigation beam can complement a conventional single-color two-photon frequency standard. While the mitigation beam impacts the atomic resonance frequency, it does not contribute to the fluorescence signal. On the one hand, this is a drawback since the energy expended for generating it is used only for light shift mitigation. On the other hand, this represents an advantage because the mitigation beam is not a vital part of the system and the clock or frequency standard can be operated without it.

As the mitigation beam is not in resonance with the clock transition, its wavelength can be chosen from a large range. The only imperative condition is that the sign of the associated sensitivity coefficient is opposite to the one of 778.1 nm wavelength. In particular, three wavelengths were identified by Martin et al. as possible options: 785 nm, 808 nm and 1556.2 nm, which are listed in Table 5.1. The predicted magnitudes of their sensitivity coefficients are sufficiently close to the one of the interrogation wavelength to guarantee technical feasibility. The corresponding AC Stark sensitivity coefficient ratios $|k_A/k_B|$ are listed in Table 5.1.

As the exact sensitivity coefficient of the mitigation beam is a function of wavelength, a mitigation laser would ideally be stabilized in frequency. In this respect, 1556.2 nm wavelength is a special case as it can be easily frequency-locked to 778.1 nm by frequency-doubling.

λ_B (nm)	$ k_A/k_B $
785	2.9
808	5.7
1556.2	10.8

Table 5.1: Suggested options [75] for mitigation laser wavelength λ_B along with the corresponding ratio of interrogation to mitigation AC Stark shift sensitivity coefficients $|k_A/k_B|$.

5.7 Choice of a Mitigation Approach

In the selection of a strategy for the experimental study of light shift mitigation, different aspects are considered. Multiple elements such as Size, Weight and Power (SWaP) and repeatability play a role. Moreover, some approaches are less suited for implementation in an optical frequency standard due to the lack of an optical frequency comb.

5.7.1 Size, Weight and Power

Protocol-focused strategies such the ones inspired by CES present the advantage that they require little additional hardware. The increased complexity of the electronics that they require would not be expected to contribute significantly to SWaP. In particular, for miniature optical frequency standards, low SWaP is essential.

When considering a compact optical clock, the optical frequency comb (including self-referencing) is part of the SWaP budget. In this case, concepts using multiple laser beams can make sense. Considering solely optical power expended for atomic interrogation, the two-photon two-color approach presents an intrinsic advantage over single-color systems. However, the SWaP increase related to sum-frequency generation would need to be considered when comparing two-color with single-color two-photon systems. For non-resonant mitigation beam options, 1556.2 nm wavelength is particular since it can be implemented with no additional laser source.

5.7.2 Repeatability

A potential concern is the extent to which light shift mitigation can be reproduced, either between individual systems of the same architecture or between different power-ups of the same system. Almost all of the above-mentioned approaches are potentially susceptible to photodiode ageing. For mitigation laser concepts with static intensities, changes of photodiode responsivity could be of concern since they would affect the power measurement for each wavelength and thus the actually achieved intensity ratio. Assuming that responsivity changes are different for each wavelength, the resulting net light shift would also change over time. In the case of CES-inspired approaches, the calibration coefficient β depends strongly on measured power. More specifically, if the linearity of the response is affected, the resulting bias could be important since β is a cubic function of the power ratio between operational regimes (Eq. (5.11)). Finally, the only potential exception to the concern of photodiode aging would be a mitigation laser approach with optical intensity modulation. Due to the direct detection of the net light shift via the atomic response, the measured optical power levels become irrelevant. However, instead of the photodiode responsivity, the modulation depth achieved for each wavelength could change over time and impact frequency repeatability.

Additionally, in CES-inspired approaches, the offset-lock on resonance frequency may compromise on repeatability. Unless the determination of the lock-point offset is highly repeatable, the LO might be locked to a different frequency each time the system is rebooted or perturbed. The mitigation laser concepts, in contrast, can be expected to be more robust in this respect since they allow to accomplish an offset-less frequency lock on the fluorescence maximum.

For two-color interrogation, an additional challenge concerns the selection of the comb line used to reference at least one of the single beams. When the comb is fully referenced, the AC Stark shift sensitivity coefficient is determined by the number of the comb mode that the 780 nm laser is locked to. Therefore, if the laser frequency is referenced to another comb mode than at the previous start-up, the power ratio required for zero net light shift is different. Moreover, not only the frequency of the 780 nm beam would change, but also the one of the 776 nm beam, given that their sum frequency is stabilized on the two-photon transition. Frequency jumps between start-ups due to the described effect have been observed in practice [2].

5.7.3 Application to an Optical Frequency Standard

As pointed out above, CES-inspired approaches would suit well their application in an optical frequency standard. However, they would need to fulfill the requirements of the targeted application regarding frequency accuracy and repeatability.

A mitigation laser based single-color two-photon system could be realized quite easily within an optical frequency standard without output in the microwave frequency domain, whereas the two-color approach without an optical frequency comb would be more complex to implement. While the lines of the frequency comb comprised in a full-fledged optical clock provide a frequency reference for the 780 nm laser, this point of reference is lacking in a two-color optical standard. In consequence, the frequency of the 780 nm laser would have to be offset-locked to the $5S_{1/2} \rightarrow 5P_{3/2}$ transition, which not only requires a separate beam passing through the atomic vapor, but also a modulator capable of introducing a several GHz frequency shift. In a potential application that requires an optical frequency reference with superior accuracy, the single-color approach could provide a simpler, cheaper and more compact technical solution.

5.7.4 Selection and Chapter Conclusions

Considering the different aspects discussed above, a mitigation laser in combination with single-color interrogation is chosen. Such a non-resonant mitigation laser has the advantage that it maintains the reduced technical complexity of a single-color two-photon system. At the same time, good repeatability is expected since the frequency lock is offset-free.

Such an approach has shortcomings regarding SWaP. In the potential further technical development of such an architecture, the power need of the mitigation laser would have to be evaluated with respect to other power needs of the system, in particular the ones of cell temperature stabilization and a potential optical frequency comb.

The mitigation laser wavelength is selected to 1556.2 nm. This choice assures excellent frequency stability for the mitigation beam. The resulting constant AC Stark shift sensitivity coefficient, however, comes at the expense of a more demanding dichroic combination of beams. The wavelengths 785 nm and 808 nm would be easier to combine with the 778.1 nm interrogation beam.

Regarding intensity stabilization, static setpoints are chosen. Such an approach, in contrast to dynamic intensity operation, does not rely on equal modulation depth for both wavelengths. Static power levels, however, leave the door open for slow power modulation for calibration. By modulating optical power slowly, the net light shift could be detected in the optical frequency by comparing it to a reference.

As mentioned previously, alternative mitigation approaches could provide different advantages for other types of applications. The selection of the approach studied in this thesis is made with regard to a compact optical frequency standard.

For the characterization of this frequency standard, an optical fiber link is required. Therefore, the following chapter briefly discusses the theory of optical fiber link stabilization. The design and practical implementation of the system are described in chapter 8.

6 Optical Fiber Link Stabilization

This chapter discusses the theoretical basis of optical fiber link stabilization. In addition, a method is suggested to combine two optical frequencies in the same fiber and stabilize their transfer simultaneously.

6.1 Indirect Stabilization using Multiplexing

Doppler Cancellation

A popular scheme for fiber link stabilization is known by the names of *Doppler cancellation technique* and *active noise compensation* [12, 70, 82]. This method compensates frequency shifts in real time. Contrary to other techniques, the acquired data does not need to be post-processed. Moreover, apart from the ultra-stable laser whose transfer is stabilized, no other laser source is required.

The basic layout of the Doppler cancellation scheme is presented in Figure 6.1. The light of an ultra-narrow linewidth laser is sent from the local end (left) to the remote end (right) of the fiber link. A portion of the transmitted light is then reflected back from the remote end by a fibered mirror. The back-reflection thus travels through the same fiber as the transmitted signal, but in the opposite direction. Under the assumption that the signal acquires the same noise on its way forth (from the local to the remote end) as on its way back (from the remote to the local end), the fiber noise is detectable on the return signal. The comparison of the return signal to a portion of light that has not travelled through the link reveals the quasi-instantaneous fiber noise.

The scheme can be viewed as an unbalanced Michelson interferometer with a reference arm being orders of magnitudes shorter than the test arm. The very short reference arm enables the interferometer to sense the variations of optical path length.

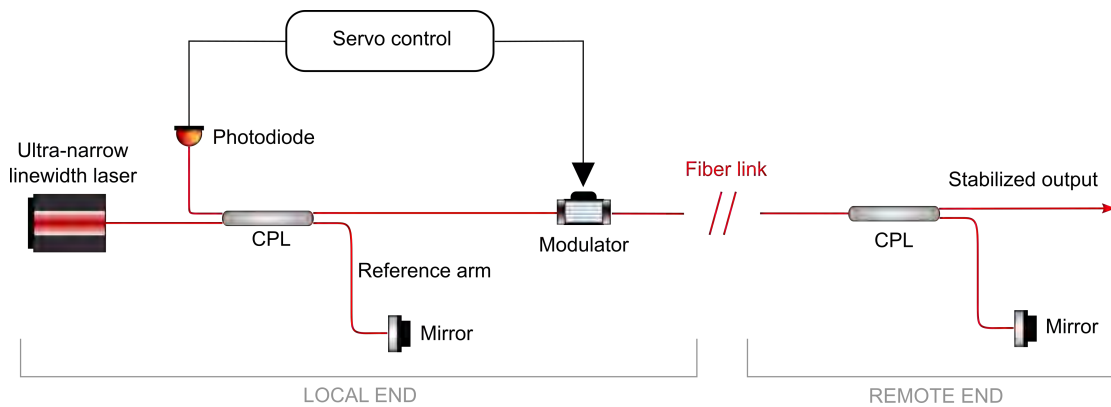


Figure 6.1: Basic layout of the Doppler cancellation scheme. The optical frequency transfer from the local to the remote end of the fiber link is stabilized through fiber noise detection and compensation by a frequency modulator at the local end. Red lines depict optical fiber, whereas black lines stand for electrical signals. CPL = fiber coupler.

Extending the Concept to two Wavelengths

In the Doppler cancellation scheme presented above, the laser that is used to sense the fiber noise is the one that is transmitted over the link. Nonetheless, it would be an advantage if the same fiber link could be used to transfer and stabilize multiple optical frequencies at once. On the one hand, fiber noise compensation has been demonstrated previously for optical frequency combs [52, 70, 73]. As a frequency comb spectrum consists of a plethora of optical frequencies, transferring its light comes down to simultaneously transmitting many different optical frequencies.

On the other hand, a fiber link featuring the stabilized and simultaneous transfer of two optical frequencies has been demonstrated for an application in quantum cryptography [26]. For the use in a Twin-Field Quantum Key Distribution (TF-QKD) protocol, a sensing laser and a reference laser were phase-locked via an optical frequency comb.

Both of the above-mentioned multi-frequency compensation schemes rely on an optical frequency comb. Another approach suggested here, in contrast, makes use of two independent CW lasers with no need for an optical frequency comb. The underlying idea is to take advantage of the small relative wavelength difference between the two signals. This property can be exploited if a *primary signal* and a *secondary signal* are multiplexed into the same fiber. The noise compensation is implemented using the primary signal in combination with the Doppler cancellation scheme presented above. Although fiber noise cancellation is tailored to the primary signal, it is expected to be beneficial also for the secondary signal. The relative similarity of the two wavelengths namely leads to a commonality of the fiber noise. Apart from wavelength, optical path length variations are determined by physical fiber length fluctuations. These are the same for both signals. Moreover, also the fiber refractive index has an influence on optical path length. If the refractive index is similar for both wavelengths, indirect fiber noise compensation for the secondary signal is effective.

In the conventional Doppler cancellation scheme, the modulator introduces a variable phase or frequency shift that compensates the instantaneous link noise. This means that the modulator phase shift is tailored to the fiber noise of the primary signal. At the same time, the modulator acts on the two multiplexed signals simultaneously and equally. As their fiber noise differs, the fiber noise of the secondary signal cannot be fully compensated. This leads to a compensation limit that depends on the relative wavelength difference between the signals. The detailed discussion this theoretical limitation is the subject of the next paragraphs.

6.1.1 Theoretical Compensation Limit

Ratio of Uncompensated to Compensated Noise

The effect of the wavelength difference on the transfer stability between the two signals λ_1 and λ_2 is studied¹ to deduce the fiber noise compensation limit for the secondary signal. This analysis aims at expressing the ratio of uncompensated to compensated frequency shifts as a percentage. Doing so allows to assess if the difference in wavelength between the signals presents a relevant limitation for the practical implementation of the method. Given that it targets frequency comparisons of optical atomic clocks or standards, we are above all interested in time scales ≥ 1 s. The analysis shall therefore be limited to those integration times. We consider the effect that a variable time delay τ_D between the local and the remote end of the link has on the transmitted signal. The frequency at the remote end of the link $f_{out}(t)$ can be expressed as

$$f_{out}(t) = f_{in}(t - \tau_D) \left(1 - \frac{d\tau_D}{dt} \right) \quad (6.1)$$

with $f_{in}(t - \tau_D)$ being the frequency at the local end and the quantity $\left(1 - \frac{d\tau_D}{dt} \right)$ representing the Doppler shift. In an ideal case, the frequency shift resulting from the variable time delay τ_D is fully compensated by the frequency shift introduced by the control loop. In order to get an output frequency that follows the input frequency at a constant delay τ_D , i.e. the condition $f_{out}(t) = f_{in}(t - \tau_D)$ is valid, the effect of the variable time delay must be compensated by the shift added to $f_{out}(t)$. The modulator frequency shift fulfilling this condition is

$$\Delta(t) = f_{in,1}(t - \tau_{D,1}) \cdot \frac{d\tau_{D,1}}{dt} \quad (6.2)$$

The indices 1 and 2 are added to the variables to distinguish between the primary and the secondary signal. The secondary output frequency $f_{out,2}(t)$, to which $\Delta(t)$ is added as well, takes the form

$$f_{out,2}(t) = f_{in,2}(t - \tau_{D,2}) \cdot \left(1 - \frac{d\tau_{D,2}}{dt} \right) + \Delta(t) \quad (6.3)$$

¹The analysis presented here follows closely the one published in Optics Continuum [17].

Let $\delta(t) = f_{out,2}(t) - f_{in,2}(t - \tau_{D,2})$ be the uncompensated frequency shift of the secondary signal. It is due to the circumstance that the modulator shift $\Delta(t)$ is tailored to the primary signal. By combining Eqs. (6.2) and (6.3), the uncompensated shift $\delta(t)$ is expressed as

$$\delta(t) = -\frac{d\tau_{D,2}}{dt} \cdot f_{in,2}(t - \tau_{D,2}) + \frac{d\tau_{D,1}}{dt} \cdot f_{in,1}(t - \tau_{D,1}) \quad (6.4)$$

The terms $f_{in,2}(t - \tau_{D,2})$ and $f_{in,1}(t - \tau_{D,1})$ are subject to the frequency noise of their respective laser source. As the present analysis considers integration times ≥ 1 s, the frequency noise of each source must be evaluated for Fourier frequencies ≤ 1 Hz. The noise of the individual laser sources at these Fourier frequencies is negligible compared to the frequency difference between them. Therefore, in Eq. (6.4) they can be replaced by their time-independent mean values, namely

$$\overline{f_{in,2}} = \frac{c_0}{\lambda_{2,0}} \quad \text{and} \quad \overline{f_{in,1}} = \frac{c_0}{\lambda_{1,0}} \quad (6.5)$$

When τ_D is expressed as a function of the time-variant total fiber length $L(t)$, we find $\tau_D = \frac{n(t) \cdot L(t)}{c_0}$ with c_0 being the speed of light in vacuum and $n(t)$ the fiber effective refractive index. A change of either $L(t)$ or $n(t)$ impacts the optical path length and therefore the time delay τ_D . The change of optical path length $n(t) \cdot L(t)$ can be written as its time derivative $\frac{d(n(t) \cdot L(t))}{dt} = \frac{dn}{dt} \cdot L + n \cdot \frac{dL}{dt} = dL_n$. With this notation, the time derivative of the variable time delay becomes

$$\frac{d\tau_D}{dt} = \frac{dL_n}{c_0} \quad (6.6)$$

Taking advantage of Eqs. (6.4), (6.5) and (6.6), the uncompensated shift is written as

$$\delta = \left(-\frac{dL_{n,2}}{\lambda_{2,0}} + \frac{dL_{n,1}}{\lambda_{1,0}} \right) \quad (6.7)$$

In the same way, the compensated shift $\Delta(t)$ takes the time-independent form of

$$\Delta = \frac{dL_{n,1}}{\lambda_{1,0}} \quad (6.8)$$

The ratio of the uncompensated to the compensated shift is thus

$$\left| \frac{\delta}{\Delta} \right| = \left| 1 - \frac{dL_{n,2} \cdot \lambda_{1,0}}{dL_{n,1} \cdot \lambda_{2,0}} \right| \quad (6.9)$$

This expression must be evaluated numerically in function of wavelengths and effective refractive indices. In general, it can be stated that due to the expected commonality between optical path length changes and wavelength, a relatively high compensation efficiency is possible for the secondary signal.

Chapter Conclusions

An optical frequency that is transmitted over an optical fiber link suffers from fiber noise, which can be compensated using the Doppler cancellation method. A method was suggested to extend this method to two independent optical frequencies. A theoretical analysis showed that it is expected to be applicable in practice. The implementation and evaluation of this method are the subject of the next chapter.

Experiment **Part III**

7 Optical Fiber Link

The rubidium two-photon optical frequency standard and the optical reference used to characterize it are located in two different laboratories. Therefore, an optical fiber link is established to connect them. It consists of multiple patches of polarization-maintaining single-mode fiber.

Whereas the optical fiber link provides a simple means to transfer optical frequencies, it could potentially impede the characterization measurement by introducing additional noise. The total optical path length between the two ends of the fiber link is susceptible to acoustic noise and temperature changes. Unless the fiber link is stabilized, a phase or frequency measurement at the end of the link does not distinguish between fiber noise and noise of the genuine signal. However, fiber noise can be detected and compensated using different techniques such as the Doppler cancellation method (see 6.1).

The first two sections of this chapter discuss the typical fiber noise observed for that link. In particular, timescales relevant to the two-photon standard are considered. This allows to validate the frequency measurements relying on the fiber link. Moreover, the active fiber noise compensation for the case of an ultra-narrow linewidth laser is implemented.

Finally, in the last and principal section of this chapter, the approach suggested in chapter 6 is explored for stabilizing the simultaneous transfer of two distinct optical frequencies. Besides the two-photon signal at 1556.2 nm, an ultra-narrow linewidth laser with 1560.0 nm wavelength is transmitted.

7.1 Layout Plan

Different laboratories in the same building are relevant for the practical implementation of the fiber link. Besides the laboratories housing the frequency standard and the reference, these are namely the rooms where the 1560.0 nm wavelength laser is located at and the one where the stabilization setup is found. The layout plan in Figure 7.1 visualizes how these laboratories are related to each other. For the purpose of characterizing the fiber link, its local and remote

ends are located in the same laboratory, which is labeled *link stabilization*. This laboratory, however, houses neither of the two laser sources. This means that the frequencies of both lasers are transmitted over several tens of meters of fiber before the start of the fiber link. This configuration is possible since for characterization, it is of no importance whether or not the signal at its input has experienced initial fiber noise. The self-heterodyne beat note solely reveals the difference between the two frequencies which are mixed to generate it.

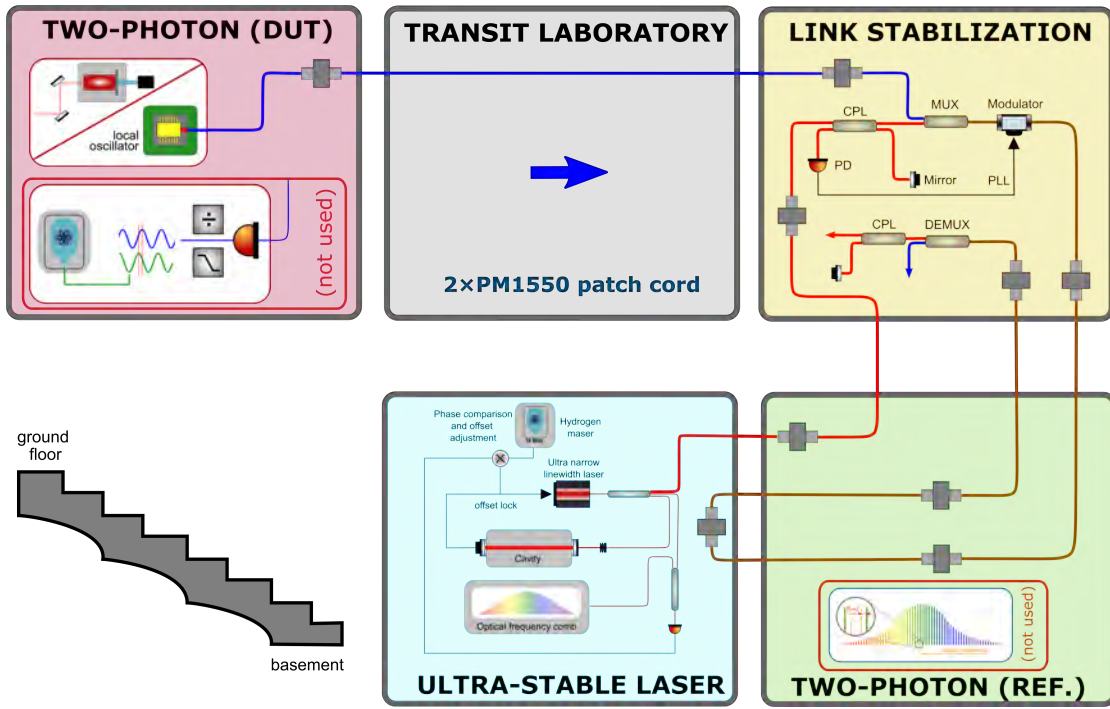


Figure 7.1: Situation plan showcasing the locations of the two-photon standard (DUT = device under test), two-photon clock (reference), 1560.0 nm wavelength ultra-stable laser, and link stabilization setup. Setup parts that are not used for the characterization of the fiber link are marked. Nonetheless, these parts are essential for the measurement of the two-photon optical frequency standard. The configuration that is used for characterizing the frequency standard is depicted in Figure 7.9 at the end of this chapter.

7.2 Transfer Stability without Fiber Noise Cancellation

As the purpose of the fiber link is to enable the characterization of the optical frequency standard, an essential question is whether the typical fiber noise does limit the frequency measurements. In particular, it is worthwhile estimating the frequency transfer stability of a fiber link without noise compensation. Therefore, the setup is configured such that the remote end is reconnected to the local end. At the same time, a part of the light that has not travelled through the link is mixed with the light that has made its way through. Finally, the light that is sent through the link is frequency-shifted by a modulator. The described configuration is depicted in Figure 7.2.

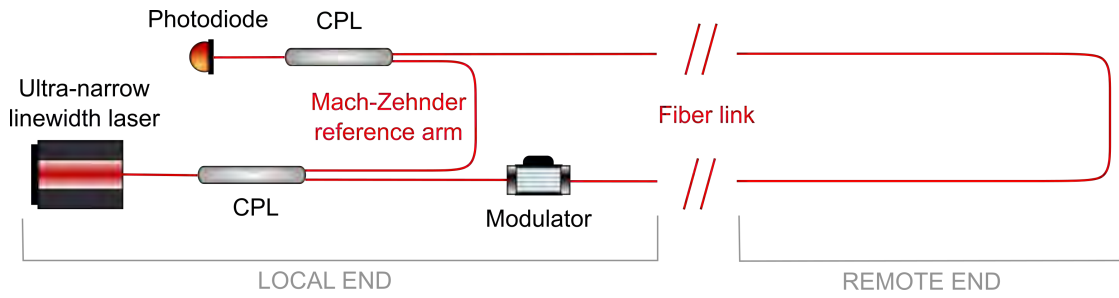


Figure 7.2: Fiber link configuration for the measurement of typical fiber noise. No noise compensation is made. From the remote end (right), the transmitted optical frequency travels back to the local end where it is mixed with a portion of light that has not travelled through the link. This allows to detect the acquired fiber noise with a photodiode.

The link characterization layout depicted in Figure 7.2 can be seen as a Mach-Zehnder interferometer (MZI). Its reference arm is kept intentionally short. In consequence, the test arm senses the variable phase delay introduced by the fiber link. The configuration reveals the additional noise introduced by the fiber link. The change in optical path length is detectable via the heterodyne beat frequency. Frequency is measured with a frequency counter. Based on the acquired frequency data, transfer instability is calculated as Overlapping Allan Deviation (OADEV). The latter is normalized to optical frequency and is plotted in Figure 7.3. The transfer instability is compared to the typical frequency instability of the two-photon standard, which is plotted alongside. The latter was measured using a fiber link of less than half the length of the characterized one, which measures 184 meters.

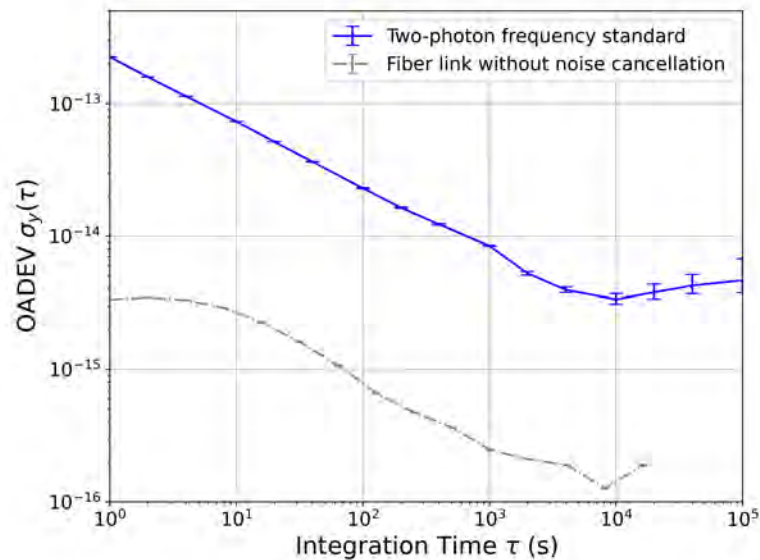


Figure 7.3: Frequency transfer instability of uncompensated fiber link expressed in Overlapping Allan Deviation (OADEV) and compared to the typical frequency instability of the optical frequency standard. With the relatively short fiber link (184 m in total), the typical link noise does not limit the characterization of the optical frequency standard.

As the curves in Figure 7.3 show, the instability of the fiber link is lower than the one of the two-photon standard. This is the case for all investigated integration times. As mentioned above, the characterized link makes its way back and forth, while the link used for characterizing the two-photon standard makes only a part of the way forth. It is concluded that for the measurement of the frequency stability of the two-photon standard, no active compensation of fiber noise is needed.

Even though it is not limiting for the application considered here, fiber noise could become a constraint for future high-performance rubidium two-photon standards in combination with longer fiber links. Therefore, fiber noise is compensated to assess the benefit of active compensation. In addition, the approach outlined in chapter 6 is explored and evaluated.

7.3 Indirect Stabilization of Optical Frequency Transfer

7.3.1 Experimental Setup

For the practical implementation of indirect link stabilization, the two signals are multiplexed into the same polarization-maintaining single-mode fiber. The total fiber link measures 184 meters from end to end. The experimental setup is detailed in Figure 7.4 below.

Primary and Secondary Lasers

The primary laser¹ is based on a whispering gallery mode micro resonator and is distinguished by its free-running ultra-narrow linewidth of 2 Hz at 1560.0 nm wavelength. Approximately 1 mW of its light is used as a seed for a home-built polarization-maintaining erbium-doped fiber amplifier. The latter is similar in design to the pre-amplifier described later in 8.1.2. It is tuned to deliver an amplified output power of 30 mW. In order to characterize the fiber link transfer stability, the amplified primary signal is split into two equal parts (CPL 4). The first part is used for the out-of-loop characterization of the primary frequency transfer stability, whereas the second part is required to stabilize the link. The portion of light used for link stabilization is once again split into two portions (CPL 1). A smaller portion (10% power) is directly reflected and guided on a photodiode (PD IL), whereas a larger portion (90% power) passes an acousto-optic modulator (AOM) before travelling through the main part of the fiber link. After 184 meters of fiber including three additional FC/APC fiber connector interfaces (mating sleeves), the signal reaches the remote link end. For characterization, the remote and local ends are placed in the same laboratory. Whereas 75% of the power reaching the remote end is expended on the out-of-loop stability measurement, the remaining 25% is reflected by a fibered mirror. The reflected light passes the link and the AOM a second time. It then reaches the photodiode at the local end (PD IL). As the AOM shifts the optical frequency by 80 MHz per passage, a 160 MHz self-heterodyne beat note is detected between the local and

¹OEwaves, model OE4028

Multiplexing

The two different wavelengths are multiplexed into the same optical fiber. Two different multiplexing methods are explored: polarization and wavelength-division multiplexing. Either fibered polarization beam splitters (PBS) or dense wavelength-division multiplexer (WDM) filters are used to combine or split the signals. For polarization multiplexing, the two signals propagate on different fiber axes. With wavelength-division multiplexing, in contrast, both signals propagate on the same (slow) axis. At the local end, the signals are multiplexed right before reaching the AOM. At the remote end, they are de-multiplexed before the fiber coupler (CPL 5) and the fibered mirror. In this way, only the primary signal is reflected back to the local end.

Although the two signals share the same 184 meters of polarization-maintaining fiber, in some setup parts, they travel over different fibers. Therefore, the optical path on which the primary signal fiber noise is compensated does not exactly match the one of the secondary signal. In terms of fiber length, approximately 8.5 meters of the primary link are not part of the secondary one. For the 184-m long link, this represents almost 5% of its total length. This ratio is the same for both multiplexing methods. In principle, this length could be reduced by shortening and splicing fibers. However, this would mean that the fibered components cannot be swapped easily. In particular, changing between multiplexing methods would be much more difficult than when using fiber connectors.

Numerical Estimation of Compensation Limit

In the theoretical part, the noise compensation limit due the wavelength difference between signals was derived analytically (see 6.1.1). It is now evaluated numerically for the two wavelengths in question. For the ease of the reader, Eq. (6.9) is repeated as Eq. (7.1) below. It gives the ratio of uncompensated to compensated frequency shifts, namely

$$\left| \frac{\delta}{\Delta} \right| = \left| 1 - \frac{dL_{n,2} \cdot \lambda_{1,0}}{dL_{n,1} \cdot \lambda_{2,0}} \right| \quad (7.1)$$

This expression is dominated either by the unknown ratio $dL_{n,2}/dL_{n,1}$ or by the known ratio of wavelengths $\lambda_{1,0}/\lambda_{2,0}$. To evaluate $dL_{n,2}/dL_{n,1}$ we replace the time-dependent by temperature-dependent expressions. The term dT/dt cancels out in the fraction and we obtain

$$\frac{dL_{n,2}}{dL_{n,1}} = \frac{\frac{dn_2}{dT} \cdot L + n_2 \cdot \frac{dL}{dT}}{\frac{dn_1}{dT} \cdot L + n_1 \cdot \frac{dL}{dT}} \quad (7.2)$$

A thermo-optical coefficient of $dn/dT \approx 10^{-5}/K$ [113] and a coefficient of thermal expansion of $dL/dT = 5.5 \times 10^{-7}/K$ [40] are assumed. Maximum temperature excursions can be expected

in a range of a few Kelvin. Moreover, the approximation

$$\frac{dn_2/dT}{dn_1/dT} \approx \frac{n_2}{n_1} \quad (7.3)$$

is made to simplify Eq. (7.1) to

$$\frac{dL_{n,2}}{dL_{n,1}} \approx \frac{n_2}{n_1} \quad (7.4)$$

Finally, using the Sellmeier equation, the refractive index dispersion for a doped silica glass step-index fiber [87] is calculated. A refractive index difference of $\Delta n_{ch} = n_1 - n_2 = -4.6 \times 10^{-5}$ can be expected due to chromatic dispersion. The wavelengths used here lead to $\lambda_{1,0}/\lambda_{2,0} - 1 = 2.44 \times 10^{-3}$. Therefore, the ratio $\lambda_{1,0}/\lambda_{2,0}$ dominates over $dL_{n,2}/dL_{n,1}$ and the following approximation is valid

$$\left| \frac{\delta_{WDM}}{\Delta} \right| \approx \left| 1 - \frac{\lambda_{1,0}}{\lambda_{2,0}} \right| = 2.44 \times 10^{-3} \quad (7.5)$$

This is the theoretical compensation limit for wavelength-division multiplexing, where both signals travel on the same fiber axis. The non-zero ratio $|\delta/\Delta|$ expresses that the Doppler shifts of the secondary frequency cannot be wiped out completely.

While a theoretical limitation due to wavelength difference exists, with the present setup and wavelengths this limitation would become comparable to the one imposed by non-common fiber parts only as soon as the fiber link is about 3.5 km or longer. Such a length is sufficient for most on-campus applications.

Finally, the study of modal birefringence allows to determine the theoretical compensation limit for polarization multiplexing, where the two signals travel on different fiber axes. Phase modal birefringence and its temperature sensitivity were determined experimentally for a panda fiber [58] similar to the one used here. The same phase modal birefringence $\Delta n_{mod} = 3.7 \times 10^{-4}$ as reported in [58] is assumed. Moreover, chromatic dispersion is neglected, knowing that $\Delta n_{ch} = -4.6 \cdot 10^{-5}$. The effective phase refractive index of the slow axis is approximated by the effective group index of refraction specified for SMF-28e+ and 1550 nm wavelength [27]. We therefore have $n_{1,slow} = 1.4677$ for the slow axis and $n_{2,fast} = n_{1,slow} - \Delta n_{mod}$. Inserting Eq. (7.3) into Eq. (6.8) results in

$$\left| \frac{\delta_{PBS}}{\Delta} \right| \approx \left| 1 - \frac{n_{2,fast} \cdot \lambda_{1,0}}{n_{1,slow} \cdot \lambda_{2,0}} \right| = 2.19 \times 10^{-3} \quad (7.6)$$

Compared to wavelength-division multiplexing, the compensation limit for polarization multiplexing therefore improves by over 10%. This advantage can only be leveraged if the longer of the two wavelengths travels on the slow axis.

Characterization

The link transfer stability is characterized with out-of-loop measurements enabled by a Mach-Zehnder interferometer configuration. The Mach-Zehnder interferometer is intertwined with the Michelson interferometer that senses the fiber noise. Both the primary and the secondary signal are characterized in this fashion, which is highlighted in Figure 7.4. Two photodiodes detect each out-of-loop beat note separately. Both of them are at 80 MHz carrier frequency.

Phase noise measurements permit to gain an understanding of the different noise contributions and the lock bandwidth. These measurements investigate shorter integration times, namely between 1 μ s and 10 s. Frequency measurements, in contrast, investigate longer integration times above 1 s and are presented below.

7.3.2 Frequency Measurements

For the frequency measurements, different instances of the same frequency counter model² are used. They are referenced to the 10 MHz signal of an active hydrogen maser. The acquired frequency data is subsequently normalized with respect to optical carrier frequency. Overlapping Allan Deviation is calculated to express the instability of the optical frequency transfer. The corresponding curves are plotted in Figure 7.5 and are used to compare the two multiplexing methods to each other, as well as to a fiber link without noise cancellation.

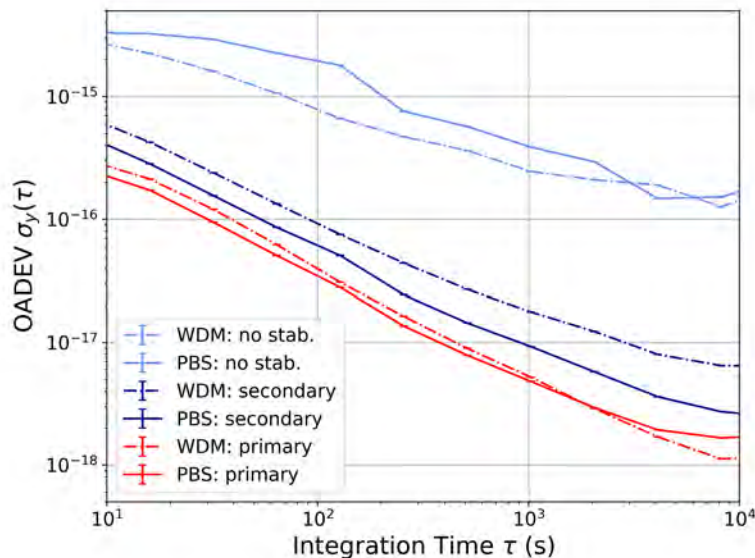


Figure 7.5: Frequency transfer instabilities of the 184-meter fiber link with and without fiber noise compensation. Primary and secondary signals are compared to each other. The OADEVs are normalized to optical carrier frequency. WDM = wavelength-division multiplexer, PBS = polarization beam splitter, no stab. = fiber noise is not being compensated. Figure initially published in [17].

²Agilent, model 53132A, (Δ -type counter with dead time)

Transfer Stability Improvement through Indirect Stabilization

Figure 7.5 shows that both multiplexing methods achieve very similar results for the primary signal. This is the case for all integration times. For the secondary signal, however, polarization multiplexing achieves better transfer stability than wavelength-division multiplexing. The disparity is around a factor of two and is observed at all considered integration times.

Compared to a fiber link without noise cancellation, the transfer stability of the secondary signal is improved with both multiplexing methods. With wavelength-division multiplexing, the measured improvement at 1000 seconds integration time is 11.5 dB or 14-fold. For polarization multiplexing, a somewhat larger 16 dB or 40-fold stability improvement is observed at the same integration time.

Fiber Noise in Common and Non-Common Fiber Parts

In quantitative terms, the stability improvement for the secondary signal is clearly below the limit imposed by the difference in wavelength (Eqs. (7.5) and (7.6) for WDM and PBS, respectively). The stability of indirect compensation is presumed to be limited by the non-common optical fiber segments. As mentioned above, these segments are relatively long in comparison with the actual fiber link of 184 meters length. As the ratio of non-common to common fiber length is the same for both multiplexing methods, the same limitation would be expected. However, this does not agree with observation. A possible explanation for this behavior is provided in the next paragraph. The ratio of common to non-common fiber parts can be used for an order-of-magnitude estimation of the noise compensation limit achievable for the secondary signal. In addition, a clearer picture is provided by phase noise measurements using a very short link of 2 meters instead of the full 184 meters length. These measurements are presented below in 7.3.3.

It is unclear by how much the noise contributions per meter of fiber differ between the different segments along the link and within the setup. Nonetheless, for integration times above 10 seconds, it can be assumed that fiber noise is mainly driven by temperature changes. Given that no fiber segments are thermally insulated, roughly similar fiber noise is expected for fibers in the setup and along the link. For integration times above 10 seconds, indirect compensation would thus fail to cancel roughly 5 percent of the secondary signal fiber noise, since this corresponds to the ratio of uncommon to common fiber. The stability improvement would thus be approximately 20-fold compared to a link without noise compensation. At 1000 seconds integration time, the stability improvement is compatible with this prediction. As pointed out, at 1000 seconds integration time, 14-fold and 40-fold stability improvements are measured for polarization and wavelength-division multiplexing, respectively. The ratio of non-common to common fiber parts does not provide an explanation for the performance disparity among multiplexing methods. However, the port configuration of their multiplexing elements provides a potential explanation. Both the PBS and the WDM have 1-m-long fiber tails and are placed in plastic fiber trays. The trays are equipped with two reels for fiber coiling.

But whereas the primary and the secondary signal exit the WDM from opposite sides, they leave the PBS on the same side. This means that in the PBS configuration, the two fiber ends are spooled on the same reel, whereas in the WDM configuration they are on two different reels. When the fiber ends are spooled on the same reel, an increased fiber noise commonality can be expected. As this is the case with polarization multiplexing, the performance improvement it shows with respect to wavelength-division multiplexing is suspected to be caused by this difference.

7.3.3 Phase Noise Measurements

Phase noise measurements are performed for both the primary and the secondary signal. The same phase noise analyzer³ is used. The measurements are done consecutively. As with the frequency measurements, both multiplexing methods are characterized. For polarization multiplexing only, the 184-meter link is replaced by a 2-meter patch cord. Measuring phase noise with this very short fiber makes it possible to separate the fiber noise of the stabilization setup from the one of the main part of the link.

Polarization Multiplexing

When using polarization multiplexing, the primary frequency (1560.0 nm wavelength) travels on the slow axis, whereas the secondary frequency (1556.2 nm wavelength) is transmitted over the fast axis. Phase noise measurements are made with and without noise compensation. The phase noise spectra without compensation are shown in the top part of Figure 7.6, whereas the spectra with noise cancellation are depicted in the lower part of the same graph.

Without noise compensation (Figure 7.6, top), the spectra of the primary and the secondary signals are very similar in the frequency range from 1 Hz to 1 kHz. As expected, the phase noise of the much shorter 2-meter link is significantly lower than for the 184-meter link. The similarities in 184-meter link spectra of the primary and the secondary signal indicate that the signal acquires acoustic noise along the link, which affects the two wavelengths alike. In contrast, between 1 kHz and 1 MHz, the phase noise for the secondary laser is clearly higher than for the primary one. This is attributed to the higher phase noise of the secondary laser.

For the primary signal with noise cancellation, a difference in servo bandwidth is visible between the shorter and the longer link (Figure 7.6, bottom). It is interpreted as the delay contribution arising from the circumstance that the shorter link has a higher bandwidth than the longer one. Assuming a compounded electronic and AOM delay time of 1 μ s [80] and knowing that the optical delay of the 184-m-long fiber is 0.9 μ s, servo bandwidths of approximately 130 kHz and 250 kHz are expected for the longer and the shorter link, respectively. These values are corroborated by the servo bumps in the bottom part of Figure 7.6.

³Rohde & Schwarz, model FSWP50

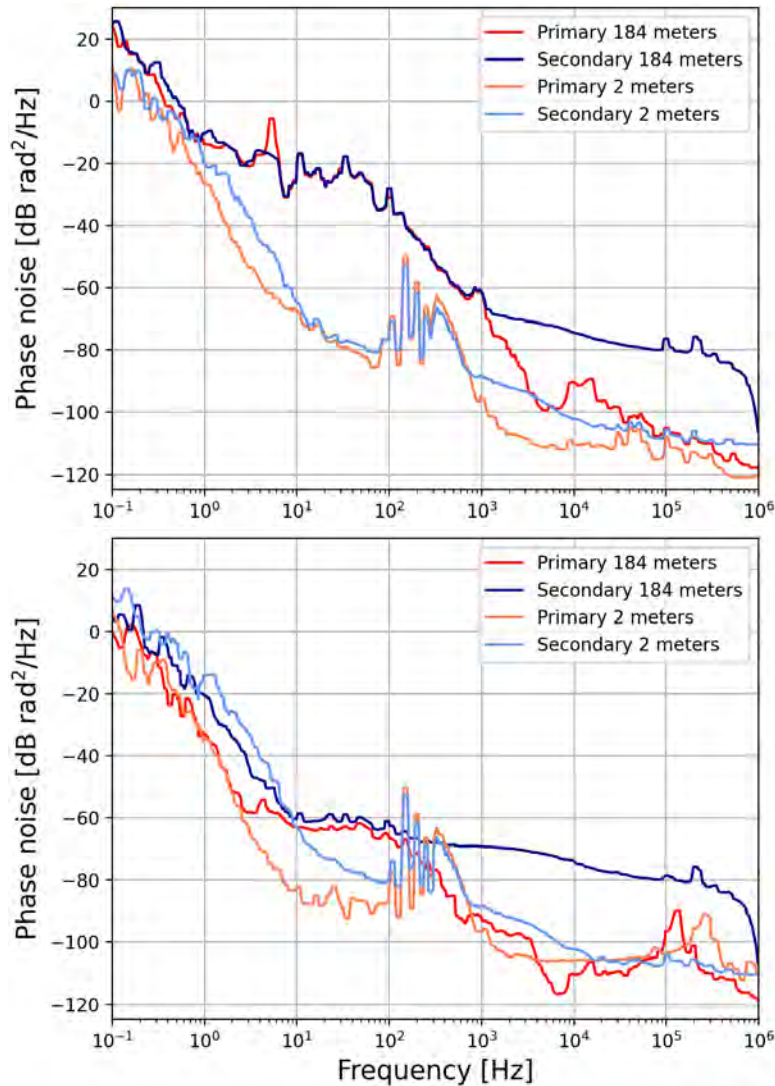


Figure 7.6: Phase noise measurements for polarization multiplexing without (top) and with noise compensation (bottom). For the longer 184-meter fiber link, fiber noise compensation clearly reduces the phase noise for frequencies below 1 kHz.

Fiber Noise from Non-Common Fiber Segments

Figure 7.7 plots the phase noise difference between the link without and with noise cancellation. Assessing the reduction in phase noise achieved for both of the investigated link lengths makes it possible to separate the fiber noise caused by the main part of the link from the noise caused by the setup. For the longer 184-meter link, in most of the spectrum within the phase-locked loop (PLL) bandwidth, a clear noise reduction is visible. For the short 2-meter link, in contrast, the observed reduction in fiber noise is weak. No reduction is discernible for the secondary signal (purple curve fluctuating around zero). Only a very small reduction could be expected given that the ratio of common to non-common fiber is weak (2 m of fiber in common vs. 8.5 m not in common). Indirect compensation has thus a negligible impact on

the secondary signal. Contrary to the secondary, the primary signal fiber noise is reduced at almost all frequencies below 100 Hz. This measurement, however, does not allow to extract the compensation limit set by the wavelength difference (see Eq. (6.9)) since the practical limit is due to the non-common fiber parts.

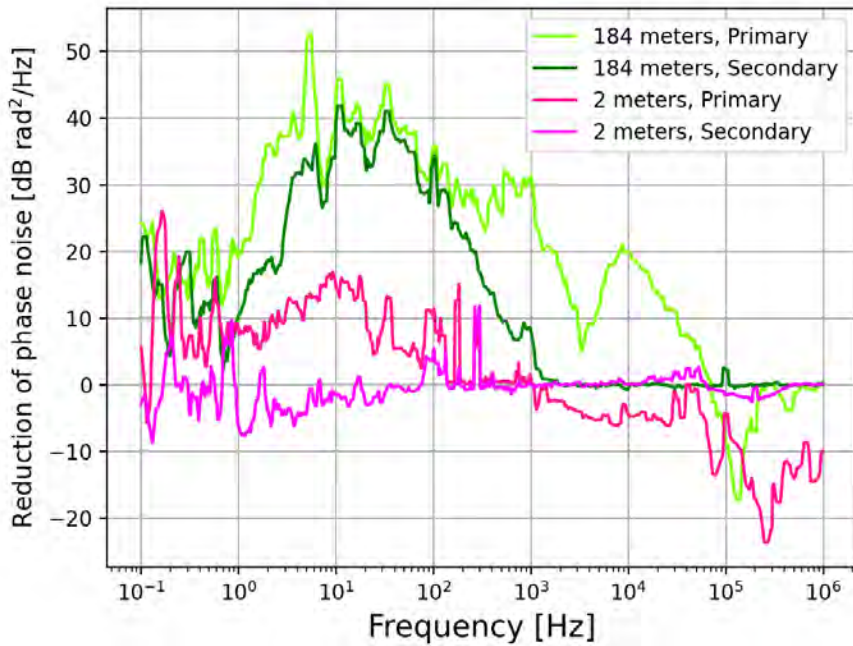


Figure 7.7: Reduction of phase noise achieved through noise compensation for the primary signal. Plot established by subtracting phase noise spectra on the bottom from the ones on the top of Figure 7.6. Measurements are made out-of-loop, at 80 MHz carrier frequency, and using polarization multiplexing.

Wavelength-Division Multiplexing

For wavelength-division multiplexing, the phase noise spectra with and without noise compensation are plotted in Figure 7.8. Apart from the out-of-loop measurements, also the in-loop measurement is plotted (in gray). In contrast to the out-of-loop measurements, its carrier frequency is 160 MHz. The in-loop phase noise spectrum shows the same servo bump slightly above 100 kHz as observed with polarization multiplexing. The out-of-loop measurements are very similar to the ones for polarization multiplexing: the phase noise of the secondary signal is reduced in the frequency range below 1 kHz when the link is stabilized. And as with polarization multiplexing, the self-delayed noise of the secondary laser limits the noise compensation for frequencies above 1 kHz. The presented phase noise measurements demonstrate that both wavelength-division and polarization multiplexing make it possible to cancel link noise of the secondary signal.

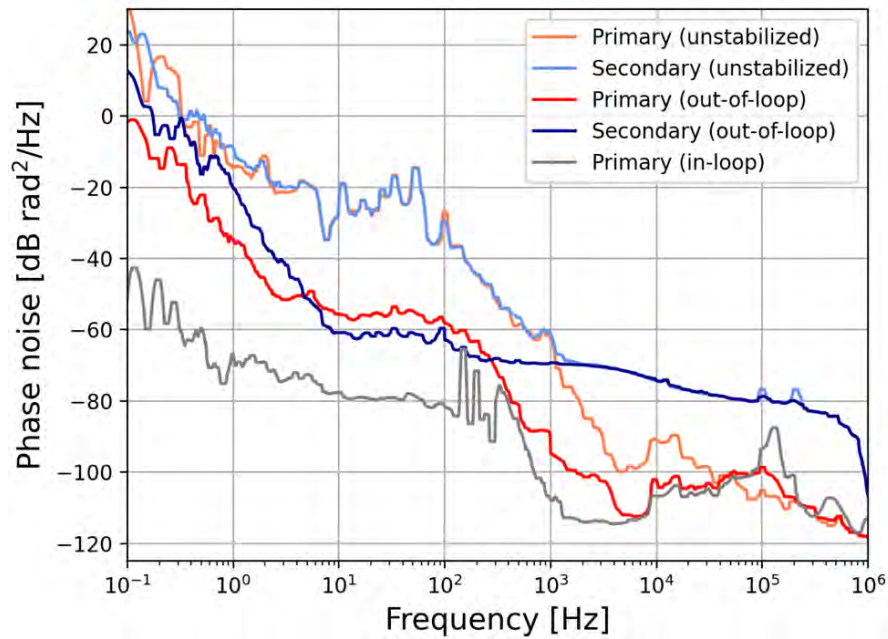


Figure 7.8: Phase noise measurements for wavelength-division multiplexing and the 184-meter fiber link without and with noise compensation. As for polarization multiplexing (see Figure 7.6), phase noise is reduced for both signals at frequencies below 1 kHz.

7.3.4 Configuration for Characterization of the Optical Standard

The indirect stabilization method discussed above is demonstrated with continuous-wave lasers. For the characterization of the optical frequency standard, however, the light of a pulsed laser is used. A portion of light from the frequency comb is transmitted according to the situation plan shown in Figure 7.9. As demonstrated above (Figure 7.3), no fiber noise cancellation is necessary for guaranteeing a reliable measurement in this configuration.

7.3.5 Chapter Conclusions

Indirect stabilization of optical frequency transfer achieves a marked reduction in fiber noise for the secondary signal. At 1000 seconds integration time, stability is improved by 16 dB using polarization multiplexing. The wavelength difference between the primary and the secondary signal has been identified as a theoretical limit of the scheme. Nonetheless, this limit was assessed to lack practical relevance for the characterization of the 184-meter fiber link.

Due to its simplicity and versatility, the investigated scheme might find other applications in frequency metrology. In particular, it may represent a user-friendly alternative to more complex schemes involving an optical frequency comb.

The fiber link between the different laboratories is used to characterize the optical frequency standard built and tested in this thesis. It features an additional 1556.2 nm wavelength beam for light shift mitigation. The design of its different elements is discussed in the next chapter.

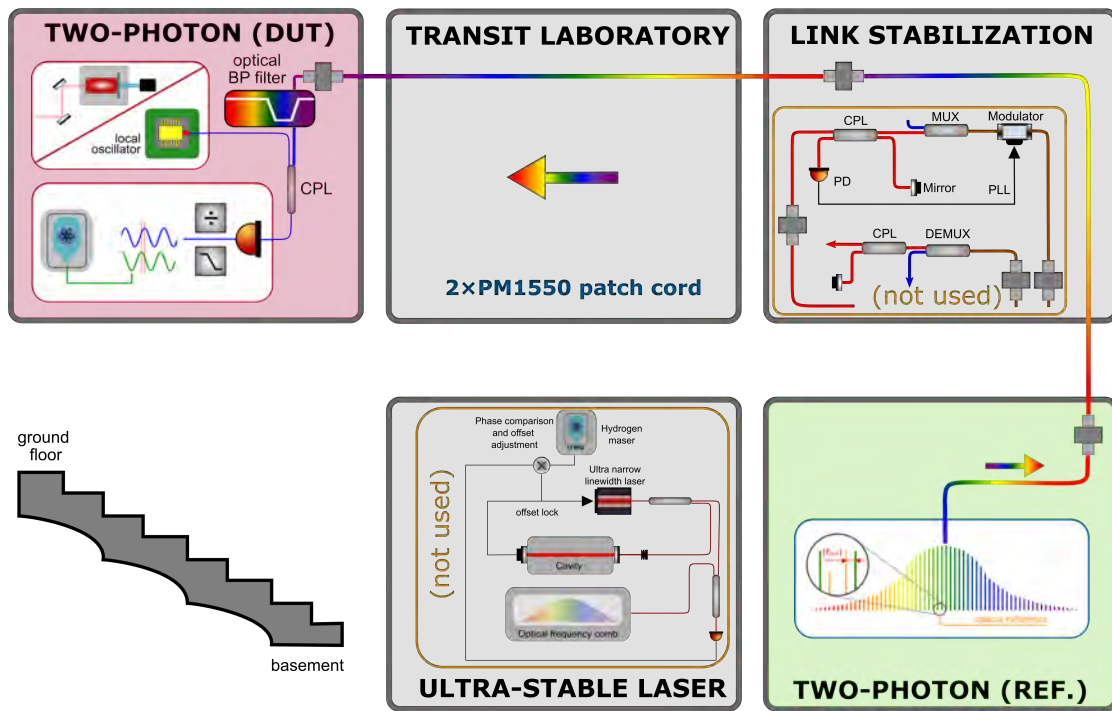


Figure 7.9: Fiber link configuration used for characterizing the stability of the optical frequency standard. Contrary to the characterization of the fiber link relying on the configuration presented in Figure 7.1, fiber noise is not compensated. Moreover, the light of an optical frequency comb is transmitted rather than a CW laser. The unused setup parts are marked.

8 Optical Frequency Standard Setup

As outlined in chapter 5, a non-resonant mitigation laser is chosen to study light shift mitigation. The system designed to investigate this approach is an optical frequency standard, which is described here below. Its stable frequency output lies in the optical frequency domain. More specifically, it is the frequency of the CW laser referred to as *clock laser*, which is approximately 192 THz (1556.2 nm wavelength). The stability of this frequency is measured in the optical frequency domain using a frequency comb. The latter is not part of the optical frequency standard, but of the characterization setup. This distinction explains by the circumstance that unlike in the case of an optical clock (see Figure 1.1), the frequency comb does not convey the relative frequency stability of the clock laser from the optical to the microwave frequency domain. Instead, the absolute frequency difference between the clock laser and the closest comb mode is made accessible by beating the two lasers. Nevertheless, the frequency comb itself is part of an optical clock since it is locked to another rubidium two-photon frequency standard. By locking a mode of the self-referenced frequency comb to the second optical standard, that standard is accessible as a frequency reference in the optical domain. The frequency comb thus allows to characterize the rubidium two-photon standard under test.

The main building blocks of the optical frequency standard and the characterization setup are showcased in Figure 8.1. The frequency standard is shown on the upper, whereas the characterization part is displayed on the lower part of the scheme. The optical frequency standard consists of a fiber optics and a free-space part. Both of them additionally comprise control electronics that are not shown in the scheme. In the free-space part, which is surrounded by an insulating and light-tight wooden box, the interrogation and the mitigation beam are made to overlap. They subsequently interact with the rubidium vapor confined in a hot atomic vapor cell. Moreover, the fluorescence signal resulting from Doppler-free two-photon spectroscopy is detected with a photomultiplier tube.

The characterization setup consists of the above-mentioned optical frequency comb as well as another part operating in the microwave frequency domain. It filters, amplifies and divides the beat note of the comb and the frequency standard. The above-mentioned elements are described in further detail below, starting with the fiber optics part of the two-photon standard.

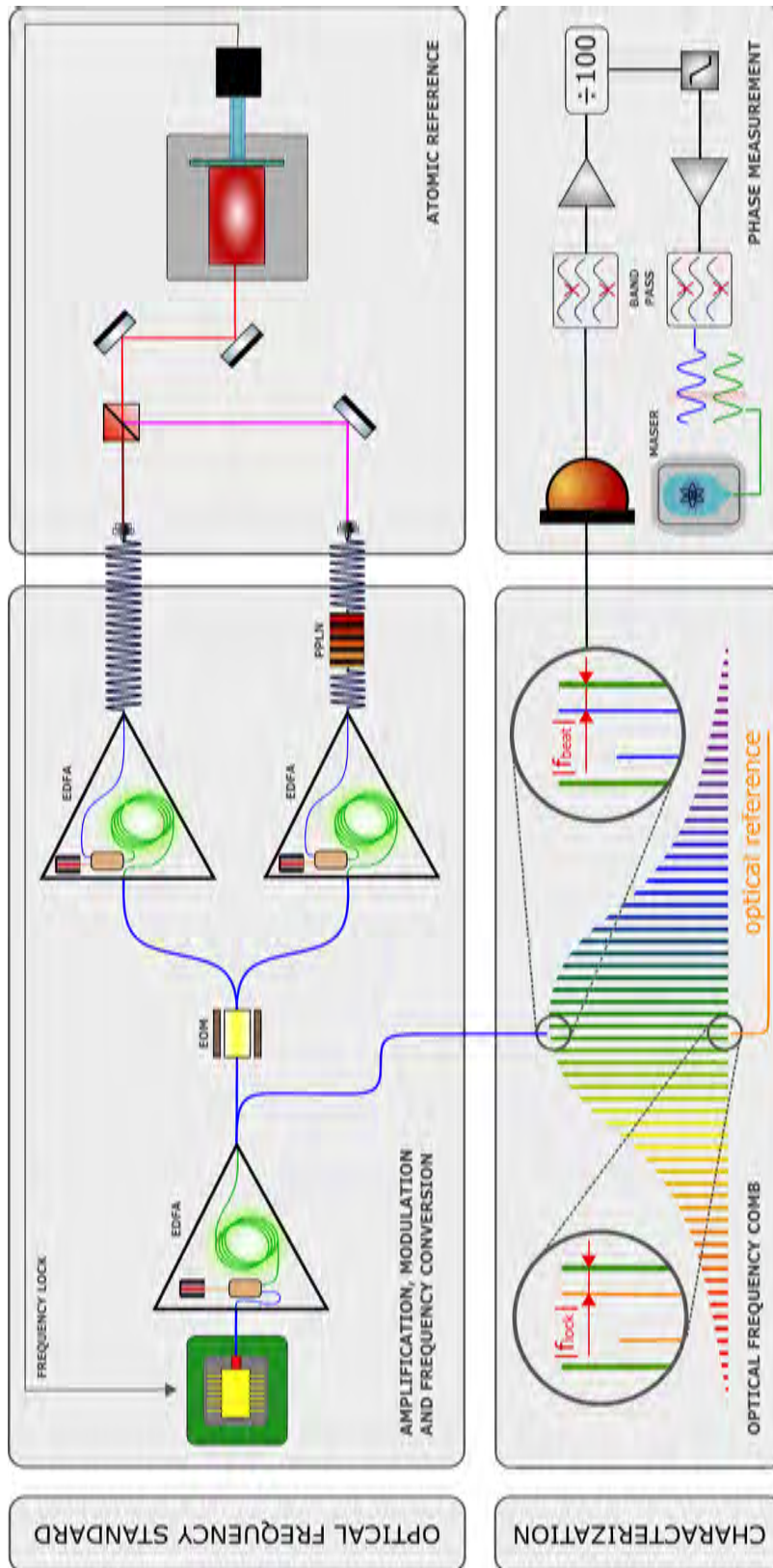


Figure 8.1: Overview of the system units composing the optical frequency standard (above) and the characterization setup (below). The optical frequency standard comprises a fiber optics (top left) and a free-space part (top right). The characterization setup consists of an optical frequency comb (bottom left) and a RF part (bottom right) dedicated to phase comparison to an active hydrogen maser 10 MHz sine wave signal, which serves as a reference. PPLN = periodically poled lithium niobate (crystal).

8.1 Fiber Optics Part

The fiber optics part prepares the clock laser light for the free-space part where two-photon spectroscopy is done. It fulfills three tasks, namely: frequency modulation of the laser light enabling synchronous detection, amplification using home-made erbium-doped fiber amplifiers (EDFA), and the frequency conversion from 1556.2 nm to 778.1 nm wavelength using a commercial periodically poled lithium niobate (PPLN) module. At the heart of the fiber optics part lies the clock laser. Its output is amplified in two stages.

8.1.1 Clock Laser

The clock laser provides the seed for both the interrogation and the mitigation beam. A 1556.2 nm wavelength narrow linewidth butterfly package External Cavity Diode Laser¹ (ECDL) is selected. It has a manufacturer specified linewidth of less than 1.25 kHz, which is sufficiently narrow to avoid significant contributions to the broadening of the detected atomic transition linewidth. Laser current and temperature are controlled with a low-noise laser controller.

Whereas laser current modulation serves to keep it locked on the two-photon transition, the temperature setpoint of the controller is not modulated during operation. Instead, initial manual tuning of this setpoint brings the frequency-doubled clock laser in spectral vicinity of the atomic resonance frequency.

8.1.2 Pre-Amplifier

The clock laser is amplified in two stages, starting with the pre-amplifier presented schematically in Figure 8.2. Like the other EDFAs that are presented later on, the pre-amplifier is polarization-maintaining. It provides approximately 120 mW of CW power at 1556.2 nm wavelength. At its input, a fiber coupler picks off roughly 10% of the unamplified power. This portion of about 2 mW enables laser health monitoring without reconfiguring the setup. The

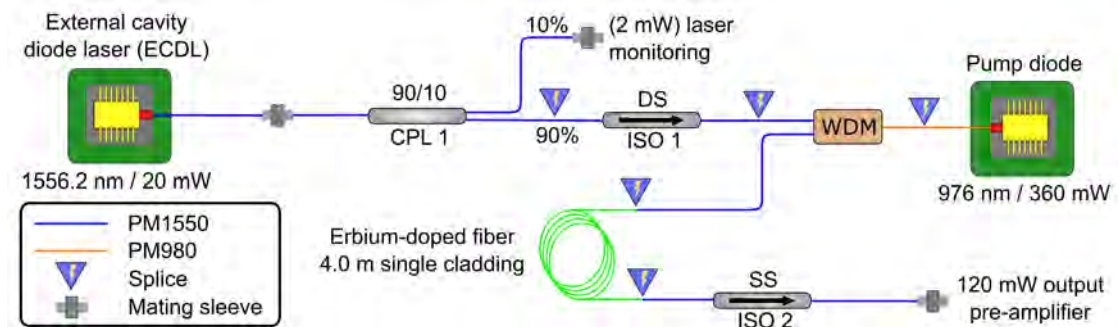


Figure 8.2: Home-made pre-amplifier in forward pumping configuration driven by a 360 mW laser diode. ISO = isolator, SS = single stage, DS = dual stage, CPL = fiber coupler, WDM = wavelength-division multiplexer.

¹Redfern Integrated Optics, model RIO Planex™RIO0195-5-01-3-BH9

remaining 90% of optical power reach the input of the pre-amplifier where a dual-stage isolator protects the source from potential back-reflections. Following isolation, a wavelength-division multiplexer (WDM) combines the seed at 1556.2 nm wavelength with the light of a laser diode at 976 nm wavelength. This pump diode delivers 360 mW of power and is driven with a low-noise butterfly laser controller. A single-cladding polarization-maintaining erbium-doped fiber is the gain medium of the pre-amplifier. Its length (4.0 m) is chosen such that the output power at the seed wavelength is maximized by balancing amplification and absorption processes. One of its two ends is spliced to the output of the WDM where seed and pump are combined. At its second end, the amplified laser light exits the erbium-doped fiber. This configuration is commonly known as forward-pumping. The pre-amplifier output is protected with a single-stage fiber isolator, which avoids that back-reflections from the next stage are amplified and reach either the pump or the seed laser. An FC/APC fiber connector is spliced to the output of the single-stage isolator. This allows to disconnect and reconnect the pre-amplifier from the subsequent second fiber optics stage, whose architecture is detailed below.

8.1.3 Power Splitting and Amplification

The second amplification stage is depicted in Figure 8.3. It is connected to the output of the first amplification stage with a mating sleeve joining two FC/APC connectors. At the beginning of the second stage, a portion of light is branched off through the 25% output of a 75/25 fiber coupler. The 30 mW that are split off in this way are provided to the characterization setup. The transmitted 75% or about 90 mW of clock laser light pass subsequently an electro-optic modulator (EOM). The latter modulates the clock laser at $f_m = 100$ kHz modulation frequency. By setting the amplitude of the driving signal accordingly, a modulation depth of approximately 70 kHz results on the 192 THz carrier. The DC voltage bias V_{DC} of the EOM is controlled in order to suppress residual amplitude modulation (RAM) (see 4.3).

Following the EOM, the modulated light is split into two portions of about 45 mW. Each portion is amplified with its own EDFA, whereby the two EDFAs are built in the same architecture. In contrast to the pre-amplifier, here the gain medium fibers are doped with both erbium and ytterbium atoms (Er/Yb-doped) and they have a double rather than a single cladding. The pump diodes deliver up to 9 W of optical power and are usually operated at a few amperes of electrical current. Moreover, in contrast to the pre-amplifier, the EDFAs described here are built in a backward-pumping configuration, meaning that the pump and the seed propagate in opposite directions. Therefore, the residual pump light must be rejected from the fiber cladding at the seed input end of the doped fiber, which is accomplished by bending the stripped fiber end and applying a low refractive index re-coating on the splice. This arrangement is known as cladding mode stripper (CMS) and discards the remaining pump light propagating in the outer fiber cladding by scattering it off from the fiber re-coating. The pump current of each EDFA is controlled individually by applying a modulation on the corresponding current source. This architecture allows for independent power control of both the interrogation and the mitigation beam, which is vital to master their intensity ratio and

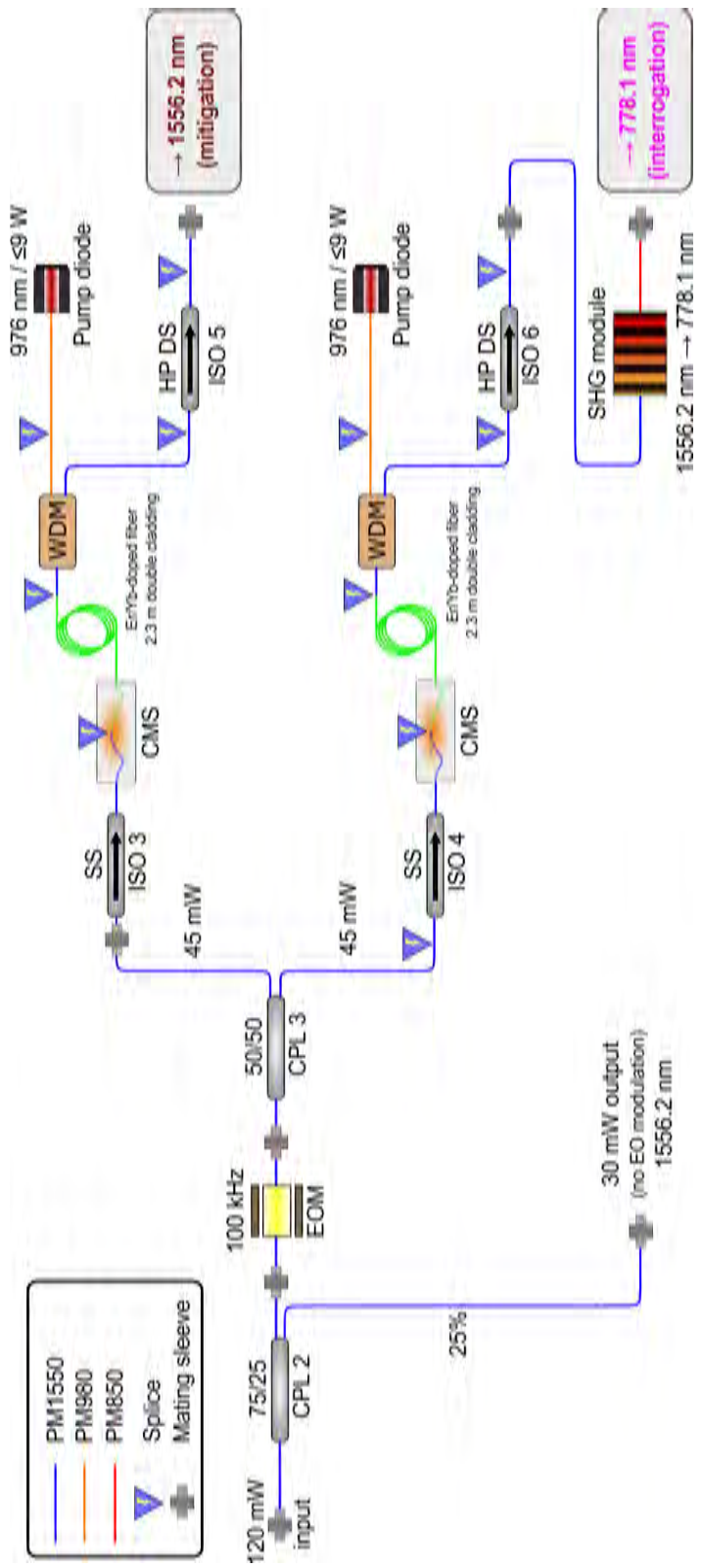


Figure 8.3: Second amplification stage including frequency modulation and frequency doubling. The two outputs on the right are connected to the free-space part. ISO = isolator, SS = single stage, DS = dual stage, CPL = fiber coupler, WDM = wavelength-division multiplexer, SHG = second-harmonic generation, CMS = cladding mode stripper, EOM = electro-optic modulator.

thus their net light shift. Whereas the output of the amplifier above in Figure 8.3 is directly launched in free-space, the output of the amplifier below is converted from 1556.2 nm to 778.1 nm wavelength. This is achieved with a commercial fibered frequency doubler module consisting of a periodically-poled highly non-linear lithium-niobate crystal, which is depicted in the lower right-hand corner of Figure 8.3. Optimal phase matching and thus maximized conversion efficiency is achieved by actively controlling the crystal temperature. A setpoint around 80°C is determined in an initial measurement and is not adapted during operation.

The amplified and frequency-modulated light at both wavelengths is delivered to the free-space atomic reference. As indicated in the top left corner of Figure 8.3, PM1550 and PM850 fiber is used for 1556.2 nm and 778.1 nm wavelength, respectively.

8.2 Atomic Reference

The atomic reference is implemented in a free-space optical setup and is represented schematically in Figure 8.4 below. Its primary functions are to combine the two different beams, to accomplish Doppler free two-photon spectroscopy, and to detect the fluorescence signal. A secondary function is the detection of laser power and residual amplitude modulation (RAM). Two photographs of this setup part are provided in Figure 8.5. In the scheme in Figure 8.4,

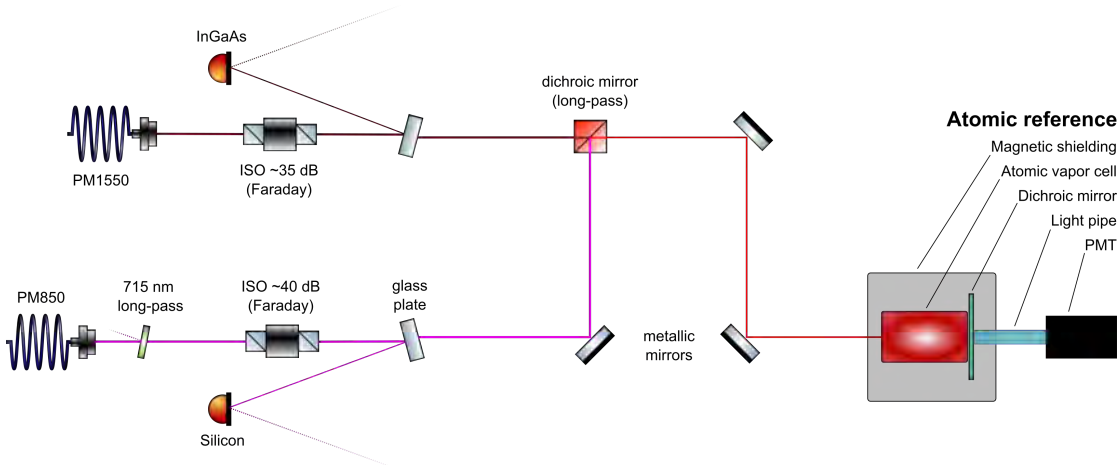


Figure 8.4: Atomic reference implemented in free space. The interrogation and mitigation beams are made to overlap with each other using a dichroic mirror. Optical power is measured at both wavelengths by sampling a portion of each beam and detecting it with a photodiode. The setup will be extended for a proof-of-concept demonstration of light shift mitigation (see Figure 9.1) and for implementing relative intensity stabilization (see Figure 10.1).

the 778.1 nm beam is drawn in magenta, whereas the 1556.2 nm beam is sketched in brown. The combined beam is represented by the color red. As depicted on the left-hand side of the scheme, the 778.1 nm beam is launched into free space by a fiber collimator. The collimator is immediately followed by an optical long-pass filter with a cut-off wavelength of 715 nm. Such a filter is inserted to reject an unwanted spectral component stemming from the non-

linear frequency conversion in the PPLN crystal. This spectral component appears as green light and is suspected to be the third harmonic of the 1556.2 nm fundamental arising from sum-frequency generation of the second-harmonic and the fundamental frequency. As it would otherwise be detected by the PMT and degrade the signal-to-noise ratio, it is filtered out. The long-pass filter is slightly tilted to avoid back-reflections from a surface normal to the propagation axis. Following the filter, a Faraday isolator blocks the back-reflection coming from the vapor cell. Its transmission is measured to be close to 80%, as specified by the data sheet. A small portion of the transmitted beam is then reflected by a 15 mm thick glass plate. The sampled beam is directed to a silicon photodiode that is used both to measure 778.1 nm power and to detect RAM. After the beam sampler, a metallic mirror reflects the beam onto the long-pass dichroic mirror whose task it is to combine it with the 1556.2 nm beam. The latter is launched into free space by a second fiber collimator shown in the top left corner of Figure 8.4. After the collimator, the 1556.2 nm wavelength beam passes a Faraday isolator. Like for the interrogation beam, a small portion is then picked off using a 15 mm thick glass plate. The sampled beam is directed onto an InGaAs photodiode. The transmitted beam, in contrast, reaches the long-pass dichroic mirror where it is combined with the interrogation beam. The combined laser beam is then directed to the atomic vapor cell. It is reflected by two gold mirrors before it passes the front hole of the single-layer magnetic shielding protecting the vapor cell. The two mirrors provide the necessary degrees of freedom (angle and position) for a precise alignment of the counter-propagating beams. For achieving the spatial overlap of the two beams, the required degrees of freedom are given by the interrogation beam collimator mount and the mirror directing the interrogation beam on the long-pass dichroic mirror. All of the planar mirrors in the setup are made of gold because this metal has a high reflectivity at both 778.1 nm and 1556.2 nm wavelength. The counter-propagating beam alignment enables Doppler-free two-photon spectroscopy. Behind the cell, both wavelengths are reflected by a custom dielectric short-pass dichroic mirror². Whereas the back-reflection of the interrogation beam is vital for eliminating the Doppler shift, the back-reflection of the mitigation beam is not essential. However, it increases the impact of the mitigation beam by a factor of almost two. Besides reflecting 778.1 nm and 1556.2 nm, the dichroic mirror also provides high isolation at these two wavelengths. Moreover, it is transparent at 420 nm in order to allow for the transmission of the atomic fluorescence signal. The fluorescence is collected by a light pipe that guides it onto the photocathode of a PMT. The photocurrent is amplified and converted to voltage by a trans-impedance amplifier unit. This signal is then provided to a digital lock-in amplifier for demodulation. As mentioned above, the fiber optics and the free-space setup parts are connected over optical fiber. More specifically, polarization-maintaining fiber couplers are used. Whereas this leads to a small power loss, it facilitates the beam alignment because the counter-propagating back-reflections can be detected. For this, however, the Faraday isolators must be temporarily removed from the setup. Couplers with splitting ratios of 90/10 and a 99/1 are used for 778.1 nm and 1556.2 nm wavelength, respectively.

²Design and fabrication by Valentin Wittwer, LTF UniNE

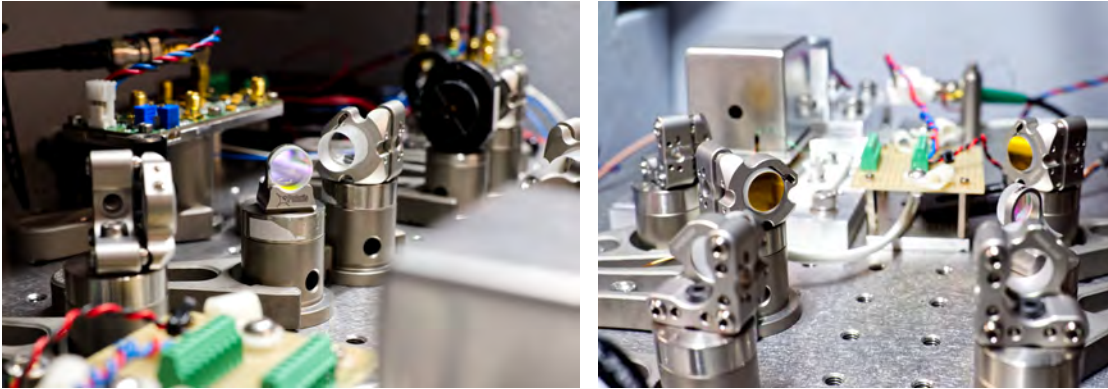


Figure 8.5: Photographs of the free-space setup part. Left: Dichroic long-pass mirror and beam sampler in the middle ground, power stabilization electronics and Faraday isolator in the background. Right: Beam sampler glass plates in the foreground, gold mirrors for the alignment of the counter-propagating beams in the middle ground, vapor cell assembly with magnetic shielding in the background.

8.3 Characterization Setup

As outlined in 7.3.4, the frequency of the optical standard is measured by beating it with a line of the frequency comb acting as an optical reference. A beat frequency f_{beat} results. Unfortunately, the phase comparator at disposal cannot directly measure f_{beat} against the 10 MHz output of an active hydrogen maser. To circumvent this restriction, a higher harmonic of f_{beat} is detected and divided. More specifically, the right-hand side beat note with the 14th harmonic of the repetition rate is detected: $f_{14+} = 14 \cdot f_{rep} + f_{beat}$. The measurement of this beat note is illustrated in Figure 8.6 below.

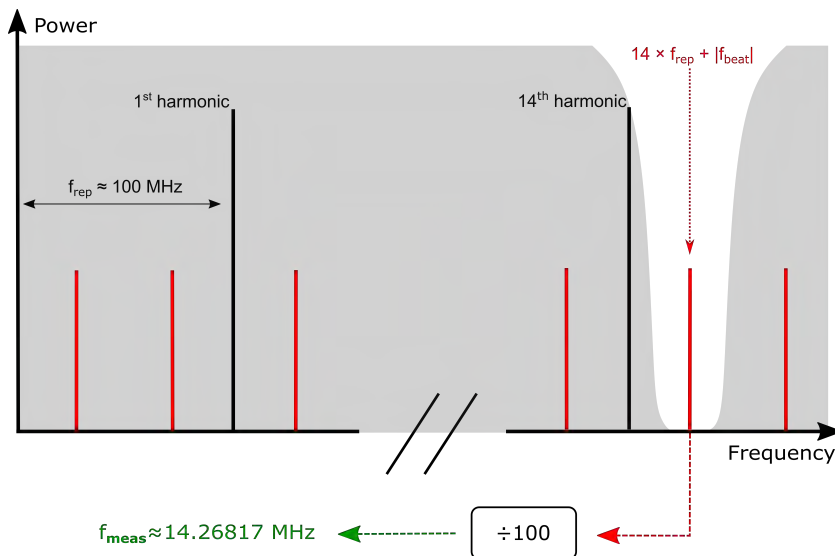


Figure 8.6: Frequency measurement in the RF domain. The beat note to the right of the fourteenth harmonic of the comb repetition rate is band-pass filtered and divided by 100 to result in the signal with frequency f_{meas} that is then measured with a phase comparator referenced to an active hydrogen maser (not shown).

The choice of the harmonic and the division factor is due to two practical restrictions. Firstly, the phase comparator³ requires a signal frequency between 1 MHz and 30 MHz. However, it cannot correctly phase-track the fundamental mode of f_{beat} as its comparatively poor phase noise leads to cycle slips. But if the higher harmonic f_{14+} is frequency-divided by 100, it can be measured. The harmonic and the division factor are chosen such that the divided frequency lies in the measurement range of the phase comparator. Secondly, separating the higher-harmonic beat frequency from the adjacent harmonic of the comb repetition rate requires a narrow bandwidth band-pass filter. The harmonic is thus also selected in function of the filter tuning range.

The full spectrum of beat frequencies is detected by a photodiode, passes a tunable band-pass filter, and is amplified with 60 dB. The frequency $f_{14+} \approx 1426.817$ MHz is isolated and divided by 100 using two daisy-chained programmable frequency prescalers. Each of them is set to a division factor of 10, resulting in a division by 100. The resulting output is a square wave at $f_{meas} \approx 14.26817$ MHz frequency. To obtain a sine wave of sufficient amplitude, the square wave is low-pass filtered, amplified by 20 dB and filtered with another tunable band-pass filter operating in a lower frequency range. The signal is low-pass filtered another time before it is supplied to the phase comparator. As a 10 MHz reference, the phase comparator receives the signal of an active hydrogen maser located in a temperature controlled environment.

8.4 Chapter Conclusions

The setup designed and built for studying light shift mitigation for the rubidium two-photon transition was presented in this chapter. It consists of a fiber optics part used for modulation and amplification, and a free-space part containing the physics package and the dichroic combination of the interrogation and mitigation wavelengths. This setup is operated as an optical frequency standard and allows to measure the AC Stark shift sensitivity coefficients of 778.1 nm and 1556.2 nm wavelength, which is done in the following chapter.

³Picotime-1U-001, Safran Timing Technology SA

9 AC Stark Shift Sensitivity Coefficients

In this chapter, the AC Stark shift sensitivity coefficients of 778.1 nm and 1556.2 nm wavelength are measured and compared to calculated values reported in literature. Moreover, the technical feasibility of the selected mitigation approach is validated with a proof-of-concept measurement.

9.1 Methodology

Before relative intensity stabilization is put in practice, the AC Stark shift sensitivity coefficients are measured for both 778.1 nm and 1556.2 nm wavelength. This is done by varying optical power stepwise while logging the frequency of the optical standard. The frequency response to optical intensity changes permits to determine the respective sensitivity coefficients, which are converted to units of Hz/(mW/mm²).

9.1.1 Measurement Setup

The free-space part of the optical setup used for the measurements is presented in Figure 9.1. It is slightly different from the one presented in the previous chapter. Power is monitored with two commercial photodetectors¹. Like in the setup in Figure 8.4, a small portion of each beam is sampled by a glass plate. However, here each glass plate is preceded by a linear polarizer instead of a Faraday isolator. As the footprint of the polarizers is smaller than the one of the isolators, the setup is more compact. This difference is relevant since the more compact alignment reduces the beam paths for both wavelengths. As the beams diverge, the path length impacts the beam profile within the vapor cell. This means that the power sensitivity coefficients (frequency over power rather than frequency over intensity) are not exactly the same for the two different setup configurations. Finally, a filter wheel equipped with different neutral density (ND) absorptive optical filters is placed in the beam path. It is used to demonstrate light shift mitigation (see 9.3).

¹Thorlabs PDA10CS-EC and PDA05CF2 for 778.1 nm and 1556.2 nm, respectively



Figure 9.1: Free-space setup for the measurement of the AC Stark shift sensitivity coefficients k_{int} and k_{mit} . Two commercial photodetectors measure optical power. An optical filter wheel with different neutral density filters is included to attenuate both beams simultaneously. POL = polarizer, PMT = photomultiplier tube.

Optical power is stabilized for each beam by feeding back on the pump current of the corresponding EDFA (see Figure 8.3). To this purpose, a proportional-integral (PI) feedback loop is implemented with the same digital lock-in amplifier² that is used for synchronous detection and locking of the atomic resonance signal. For each beam, the photodetector DC voltage is used for measuring power and locking it to a selected setpoint. There is no out-of-loop power measurement. The vapor cell temperature is stabilized to 100°C.

9.1.2 Auxiliary Measurements and Calibration

To determine the sensitivity coefficients in terms of frequency over optical intensity, three quantities must be measured. Firstly, the beam profiles have to be determined in order to convert power to intensity. Secondly, the photodetectors must be calibrated to convert voltage to power. Thirdly, a clock frequency measurement is needed. Finally, the power measurements additionally need to be scaled to represent optical power within the atomic vapor cell rather than in front of it. The three measurements and the power normalization are described below.

Beam Profile

Beam waist diameters are measured before the vapor cell assembly is integrated into the setup. The same infrared slit scanning beam profiler is used for both wavelengths. In the setup, the beam profiler is placed such that its sensor plane lies there where the center of the atomic vapor cell will be located at.

²Zurich Instruments MFLI 500 kHz

The measurements confirm that both beam profiles are Gaussian. The manufacturer of the beam profiler specifies its measurement uncertainty to $\pm 5\%$. The two waist diameters ($1/e^2$ intensity) are comparable to each other. They are namely $1.11(\pm 0.06)$ mm and $1.19(\pm 0.06)$ mm for 778.1 nm and 1556.2 nm wavelength, respectively.

Photodetector Calibration

The commercial photodetectors are calibrated through optical power measurements in front of the vapor cell. For both 778.1 nm and 1556.2 nm wavelength, calibration is performed twice using an optical power meter. Each time, a different instance of the same germanium sensor head³ is used. Additionally, for 778.1 nm wavelength a measurement is made using a silicon sensor head⁴. For each photodetector, a calibration coefficient in mW/V is obtained along with its uncertainty range.

The calibration is performed when the wooden box housing the free-space setup is left open. Operating the frequency standard, however, implies a closed box for protecting the PMT from ambient light. After initial calibration, the temperature difference between an open box (calibration, 23°C) and a closed box (operation, 30°C) is found to have a non-negligible impact on the responsivity of the silicon photodetector. The responsivity difference between the two temperature regimes is therefore measured for each photodetector. While for the 1556.2 nm photodetector the mentioned temperature difference has little impact on responsivity (less than 0.5% change), it decreases the responsivity of the 778.1 nm photodetector by as much as $6.0(\pm 0.1)\%$. This factor is therefore considered in the calibration of the silicon photodetector. This leads to the respective calibration coefficients of $2.49(\pm 0.03)$ mW/V and $34.5(\pm 0.4)$ mW/V for the 778.1 nm and the 1556.2 nm photodetectors.

Clock Frequency

Contrary to the description in 8.3, frequency is measured instead of phase. A beat note at around 160 MHz frequency is detected by mixing the frequency standard with the optical frequency comb. The beat is measured with a photodiode, band-pass filtered, and amplified. The beat frequency harmonic at 160 MHz is logged using a frequency counter, which is referenced to the 10 MHz output of an active hydrogen maser. The gate time is set to 1 s. As the beat frequency is not divided, it directly maps the frequency variations in the optical domain (192 THz carrier).

Two measurements are made: one without 1556.2 nm power where 778.1 nm power is varied, and one with varying 1556.2 nm power where 778.1 nm power is kept constant. For each measurement, optical power is increased stepwise to three different levels. In order to exclude potential hysteresis phenomena, power is decreased stepwise to the same levels.

³Thorlabs S132C

⁴Thorlabs S130C

Normalization

Optical intensity is defined as the ratio of optical power to the beam surface area πw_0^2 , where w_0 is the beam waist radius ($1/e^2$ intensity). Intensity values obtained from the photodetector voltages and calibration coefficients are scaled to represent optical intensity within the atomic vapor cell by accounting for the attenuation of its windows. For both wavelengths, transmission is 92% per borosilicate glass window comprising two facets. The incident beams are attenuated by a single window, whereas their reflections pass a window thrice.

9.2 Measurement and Calculation

9.2.1 Frequency Response to Intensity Changes

Optical power is varied and logged as described above. At the same time, frequency is measured. Both quantities are plotted in Figure 9.2. Increasing 1556.2 nm indeed has a qualitatively opposite effect on frequency than increasing 778.1 nm intensity. The observed beat frequency

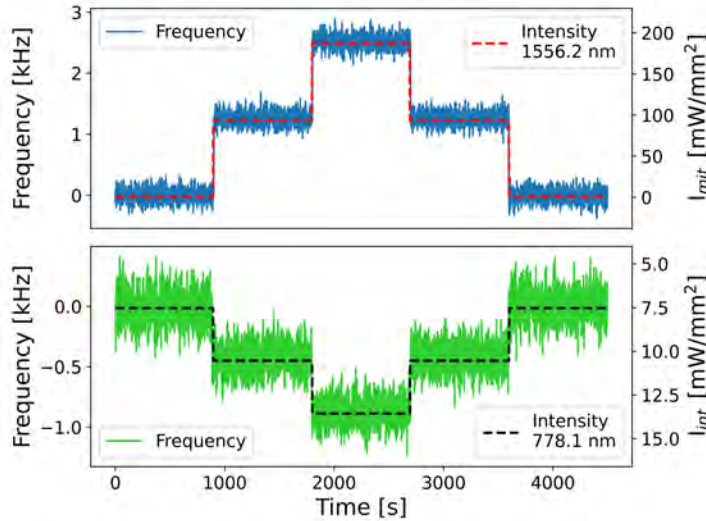


Figure 9.2: Optical frequency response to stepwise intensity changes for two mutually independent measurements for 1556.2 nm (top) and 778.1 nm (bottom). The qualitative difference in the frequency responses confirms that the signs of the AC Stark shift sensitivity coefficients are opposite for 778.1 nm and 1556.2 nm wavelength.

does not allow to determine the signs of the sensitivity coefficients. The spectral positioning of the clock laser with respect to the closest comb mode is unknown. It can be on either side of its closest neighbor. However, the sign of the self-collision shift (see 4.5.1) is known. Therefore, cell temperature is changed while logging the beat frequency. Observing the resulting frequency response in qualitative terms permits to identify on which side of the comb mode the clock laser frequency is found. The coefficient k_{778} is determined to have a negative sign, whereas k_{1556} has a positive sign.

9.2.2 Orthogonal Distance Regression

Based on the frequency measurements shown in Figure 9.2, the sensitivity coefficients are determined through orthogonal distance regression [18]. This statistical method accounts for uncertainty in both horizontal and vertical directions. Here, uncertainty in the vertical direction is due to limited short-term frequency stability, whereas uncertainty in the horizontal direction is composed of the photodetector calibration and the beam waist uncertainties. The regression plots are presented in Figure 9.3. Orthogonal distance regression results in $k_{mit} = +15.9(\pm 1.7)\text{Hz}/(\text{mW}/\text{mm}^2)$ and $k_{int} = -172(\pm 62)\text{Hz}/(\text{mW}/\text{mm}^2)$. Both coefficients are in good agreement with theoretical predictions [75] that are plotted as solid black lines.

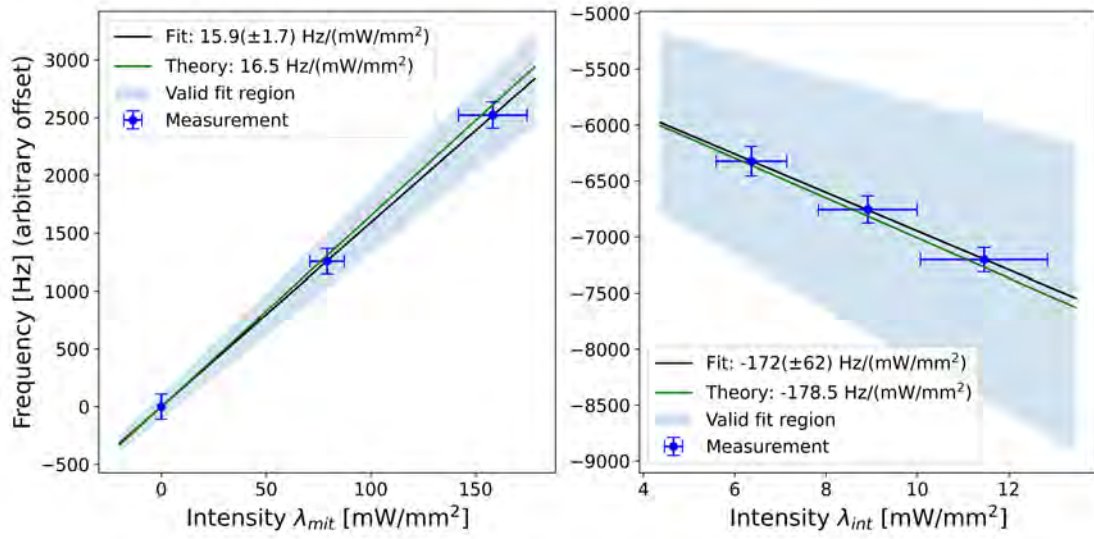


Figure 9.3: Orthogonal distance regression yielding the AC Stark shift sensitivity coefficients for 1556.2 nm (left) and 778.1 nm wavelength (right). Both sensitivity coefficients agree well with calculated values reported in literature [75].

In conclusion, experiment confirms that the coefficients k_{mit} and k_{int} are opposite in sign and differ in value by about an order of magnitude. This validates the feasibility of the non-resonant laser beam mitigation approach using 1556.2 nm wavelength.

9.3 Experimental Observation of Light Shift Compensation

Having measured the two AC Stark shift sensitivity coefficients k_{mit} and k_{int} , the power ratio of the two beams leading to zero net light shift is estimated. The power of the two beams is stabilized such that we have the intensity ratio

$$I_{mit}/I_{int} = -k_{int}/k_{mit} \approx 10.8 \quad (9.1)$$

This ratio makes clock frequency independent of overall optical power (see Eq. (5.18)). This property is verified experimentally by introducing an external perturbation: the combined

laser beam is attenuated with optical neutral density filters. Using the filter wheel shown in Figure 9.1, they are changed stepwise after five minutes (300 s).

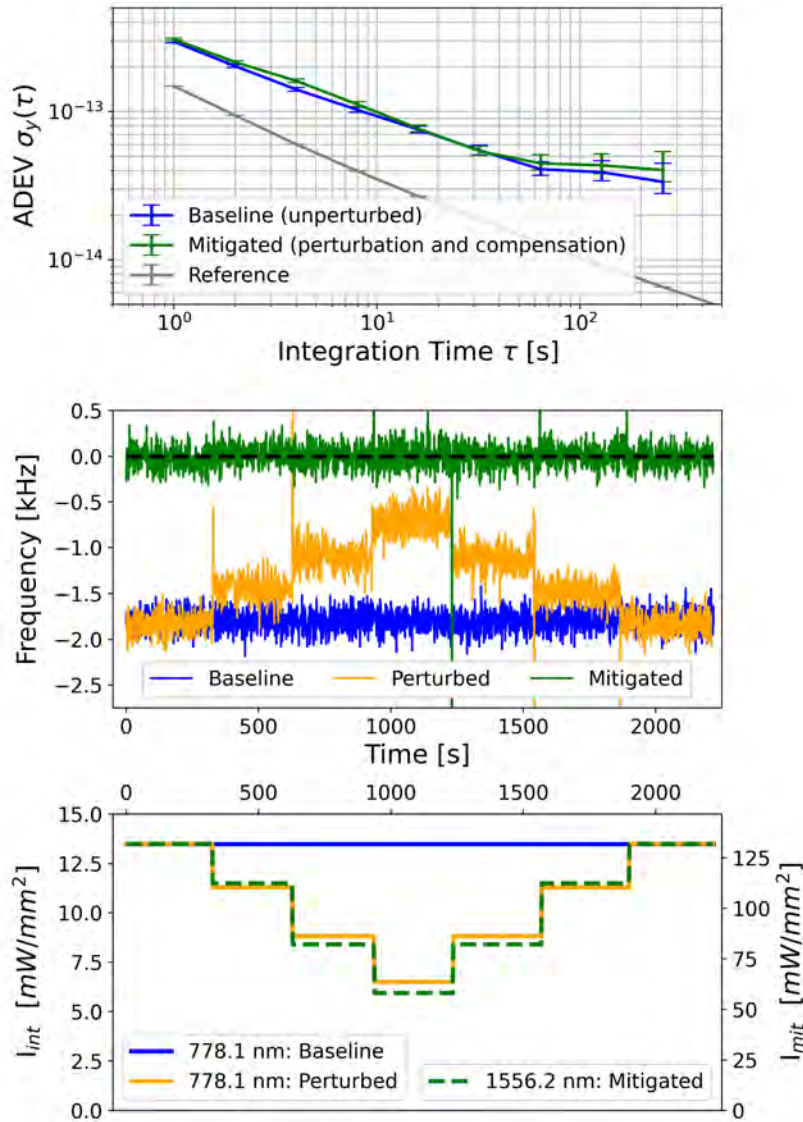


Figure 9.4: Light shift mitigation demonstrated by attenuating the combined laser beam intensity. Top: Allan Deviation, middle: clock frequency, bottom: interrogation and mitigation beam intensities. When a 1556.2 nm wavelength mitigation laser is present, the simultaneous attenuation of the interrogation and mitigation laser intensities has only a negligible impact on clock frequency, as the frequency trace and Allan Deviation labeled *Mitigated* demonstrate.

The measured clock frequency and Allan Deviation are plotted in Figure 9.4. The first measurement is labeled *Baseline* and is performed with the mitigation beam blocked. The filter wheel is set to its empty position. The second measurement is labeled *Perturbed*. It is also done with the mitigation beam blocked. The neutral density filters are swapped periodically, which results in a stepwise change of interrogation beam intensity. The empty wheel position is

used together with three different filters (ND = 0.1, 0.2 and 0.3). Finally, a third measurement, labeled *Mitigated*, is done using the same filter sequence but using the mitigation beam. Since the neutral density filters attenuate both beams by nearly the same factor, their intensity ratio stays approximately constant.

The clock frequency without light shift mitigation reacts on each neutral density filter change by hundreds of Hz, whereas almost no change is observed when the mitigation beam is present. The ADEV for perturbed but mitigated operation is almost identical with the baseline ADEV without the perturbation. This demonstrates that the adequate beam intensity ratio massively reduces the sensitivity of the clock frequency to overall optical power.

9.4 Chapter Conclusions

The AC Stark shift sensitivity coefficients k_{mit} for 1556.2 nm and k_{int} for 778.1 nm wavelength were measured. With $k_{mit} = +15.9(\pm 1.7)\text{Hz}/(\text{mW}/\text{mm}^2)$ and $k_{int} = -172(\pm 62)\text{Hz}/(\text{mW}/\text{mm}^2)$ they agree well with calculated values reported in literature [75]. This finding provides the basis for the subsequent proof-of-concept validation of the light shift mitigation approach using a non-resonant 1556.2 nm wavelength mitigation laser. The simultaneous attenuation of both laser beams demonstrated that the appropriate intensity ratio of the interrogation and mitigation beams can cancel the light shift.

Although the beam powers in the proof-of-concept demonstration are stabilized, strictly speaking their ratio is not. Instead, both beams are individually stabilized to two separate absolute references. To fully leverage the advantages of a mitigation beam, the stabilization should be relative rather than absolute. This means that the power of each beam must be stabilized with respect to the same reference. This configuration is referred to as relative intensity stabilization and is the subject of the following chapter.

10 Relative Intensity Stabilization

In this chapter, the optical intensities of the interrogation and mitigation beams are stabilized using dedicated electronic circuit boards. In particular, a common voltage reference is supplied to both circuit boards, which are used for the power measurements at 778.1 nm and 1556.2 nm wavelength, respectively. This allows to stabilize the intensity ratio of the two beams in the appropriate proportion to each other. The light shift mitigation method is tested by introducing a periodic perturbation of the voltage reference. Moreover, the temperature sensitivity of the optical power stabilization electronics is measured. From the measured temperature sensitivity coefficient, practical frequency stability limits are calculated for typical temperature variations measured in the setup. Finally, the frequency stability of an unperturbed optical frequency standard without mitigation laser is compared to the one featuring a 1556.2 nm mitigation laser.

10.1 Practical Implementation

Relative intensity stabilization is implemented according to the concept described in 5.6. The optical free-space setup is adapted as described in 10.1.1 below. In particular, the electronics for power stabilization are integrated. Their design is described later in 10.1.2.

10.1.1 Optical Setup

The free-space part is modified to the setup depicted in Figure 10.1. The commercial photodetectors are replaced by two power stabilization units, one for each wavelength. Additionally, for out-of-loop power measurements, the commercial photodetectors are reintegrated into the setup. As the beam sampler glass plates are relatively thick (15 mm), they give rise to two well-separated reflections. The reflections from their rear faces are directed onto the photodiodes of the power stabilization units (in-loop). The front face reflections are picked up by D-shaped metallic mirrors, which reflect the beams onto the commercial photodetectors (out-of-loop).

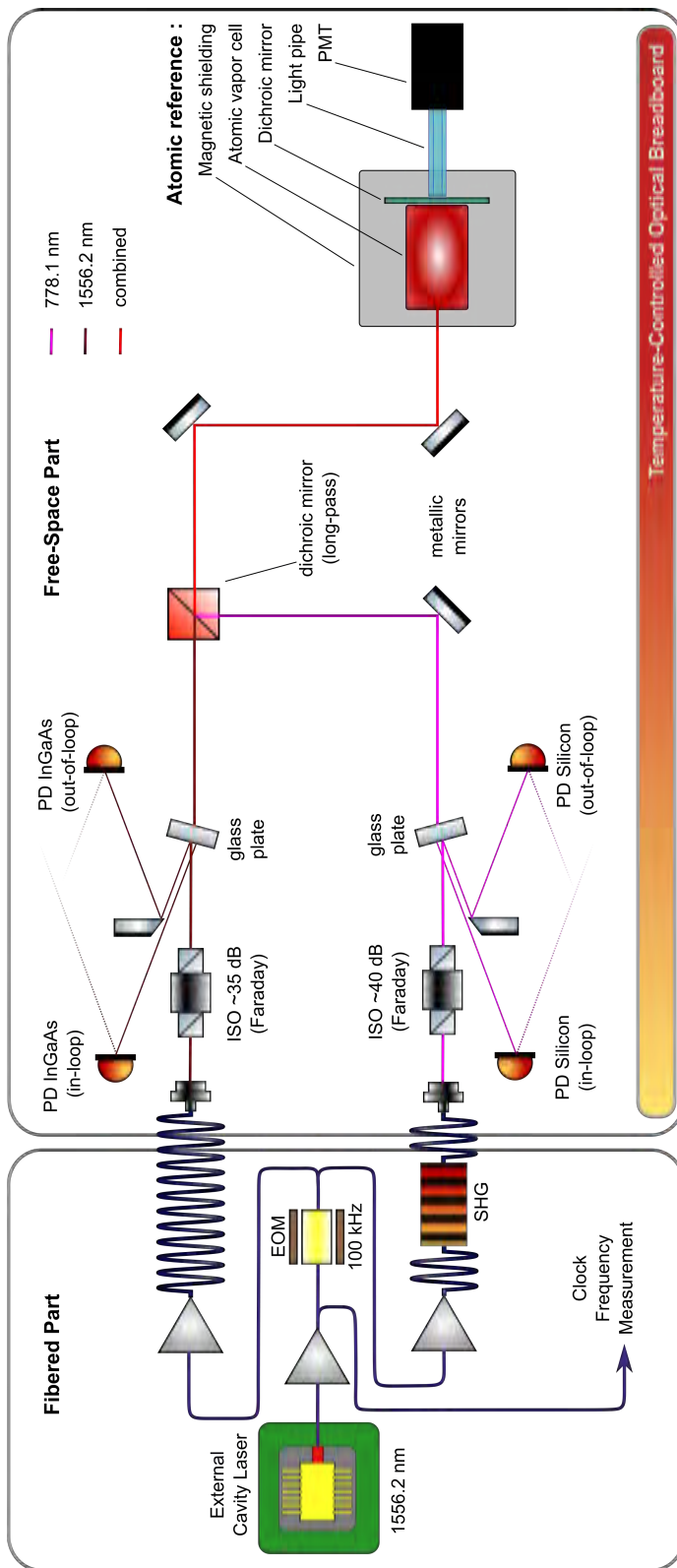


Figure 10.1: Setup for relative intensity stabilization. Optical power of each beam is measured both in-loop and out-of-loop thanks to the use of D-shaped mirrors. The optical breadboard housing the free-space setup (right) is temperature-controlled. EOM = electro-optic modulator, SHG = second-harmonic generation, PD = photodiode, ISO = isolator (with extinction ratio in dB), PMT = photomultiplier tube.

Moreover, the two linear polarizers are replaced with Faraday isolators. While they maintain a well-defined state of linear polarization at their output, they also suppress the inevitable back-reflections due to the counter-propagating beam configuration. However, as their footprint is larger than the one of the polarizers, the fiber collimators are set back by a few centimeters.

Finally, the optical breadboard is placed on top of another, water-cooled breadboard. The water temperature is controlled with a Peltier chiller, which allows to have active temperature control of the free-space setup.

For the measurements presented in the remainder of the manuscript, the cell temperature is decreased to 90°C. The frequency standard is operated using approximately 10.5 mW of interrogation power. Fractional frequency instability is about 3×10^{-13} at $\tau = 1$ s integration time and averages down with $1/\sqrt{\tau}$ over three decades. It reaches a minimum of approximately 4×10^{-15} around $\tau = 10^4$ s.

The out-of-loop interrogation power measurements indicate that frequency stability is not limited by optical power variations. This is corroborated by the fluorescence amplitude measurements. Nevertheless, deliberate perturbations of specific system parameters allow to introduce light-shift-induced frequency responses whose mitigation is studied.

10.1.2 Power Stabilization Electronics

The optical power stabilization aims at achieving low relative intensity noise (RIN), in particular for long integration times. A careful selection of electronic components is paramount [108]. Therefore, for the key components, options with a low temperature sensitivity are chosen. Two printed circuit boards (PCB) are made: one for 778.1 nm and another one for 1556.2 nm wavelength. Both PCBs follow the same basic architecture, which is described below.

A photodiode connected in photoconductive mode is soldered onto the edge of the PCB. It is followed by a trans-impedance amplifier (TIA) that amplifies and converts the photocurrent to a voltage signal. The voltage signal, which is proportional to optical power, is supplied to an operational amplifier acting as a voltage comparator. It compares the photodiode voltage signal to a user-defined setpoint. This setpoint is defined in function of an external voltage reference that is supplied on a differential input. By tuning a potentiometer, the external reference voltage is divided as desired. This potentiometer has a low temperature sensitivity of 10 ppm/°C. The voltage comparator then provides an error signal proportional to the difference between measured power and the user-defined setpoint. The error signal is supplied to a proportional-integral controller implemented by an operational amplifier with an RC-circuit defining the transfer function. Two potentiometers are used to tune its gain and corner frequency. The servo loop outputs the control signal, which is used to modulate optical power.

For each PCB, the control signal is supplied to the corresponding EDFA pump current source; the feedback loop is closed. Whereas the servo loops for the interrogation and the mitigation

power are mutually independent, they are both supplied with the same external reference voltage. However, by choosing each setpoint with the potentiometers, the power ratio P_{mit}/P_{int} is chosen freely.

For 778.1 nm wavelength, a silicon photodiode is used, whereas for 1556.2 nm an InGaAs photodiode is chosen. Sufficiently large active areas avoid that possible beam wandering causes fluctuations in the detected power. Care is taken to align the laser beams onto the photodiode surface in an angle that is not normal. This help to avoid unwanted back-reflections that can degrade the quality of the measurement. Scattered light was namely reported as a critical noise source for high-performance optical power stabilization [63, 64].

For the experiments presented here, both PCBs are supplied with an external voltage reference signal which they share. In a frequency standard designed for a use case beyond research, the internal reference of one unit could be provided as an external reference to the other one.

10.2 Voltage Reference Stability

A weak point of conventional power stabilization is its dependence on an absolute voltage reference (see 5.6.2). Therefore, the stability of different voltage references is measured in 10.2.1. This allows to quantify with which beam properties the voltage reference represents a relevant frequency stability limit via the light shift. In case it sets a limit, its adverse effect could be alleviated by the mitigation laser. This feature is investigated in 10.2.2.

10.2.1 Voltage Reference Stability Measurements

The DC voltage outputs of different devices is logged over the course of several days using a digital multimeter. The measured voltage fluctuations are then converted to expected fractional clock frequency fluctuations. As this conversion depends on the beam profile and power, two different scenarios are assumed. They are listed in Table 10.1. Scenario A assumes a beam diameter of 1.1 mm, which roughly corresponds to the one of the described frequency standard. For the optical power, a conservative assumption of 30 mW is made. Scenario B, in contrast, assumes a smaller beam with 0.2 mm diameter and 6 mW optical power. Such a small beam profile [84] can be attractive in combination with a microfabricated vapor cell as by its higher intensity it compensates the decrease in photon count due to the shorter cell.

Scenario	Optical Power	Beam Diameter	Power Coeff.
A	30 mW	1.1 mm	- 180 Hz/mW
B	6 mW	0.2 mm	- 5 500 Hz/mW

Table 10.1: Power and beam diameter ($1/e^2$ intensity) scenarios.

First, the internal voltage reference on one of the power stabilization units is characterized. In addition, a small linear power supply¹ is measured. This device cannot be considered an actual voltage reference. Instead, it is representative for a device without a voltage regulator suited for this application. Finally, another voltage reference similar to the one in the power stabilization units is characterized. Contrary to the voltage references in the optical standard, it is actively stabilized in temperature.

Measurements are made with a gate time $\tau = 10$ s except for the temperature-stabilized reference where $\tau = 1$ s is used. Based on the scenarios A and B (Table 10.1), the frequency instability limits set by the characterized voltage references are calculated. They are described by the OADEVs in Figure 10.2 below. For reference, the instability of the frequency standard is plotted in gray.

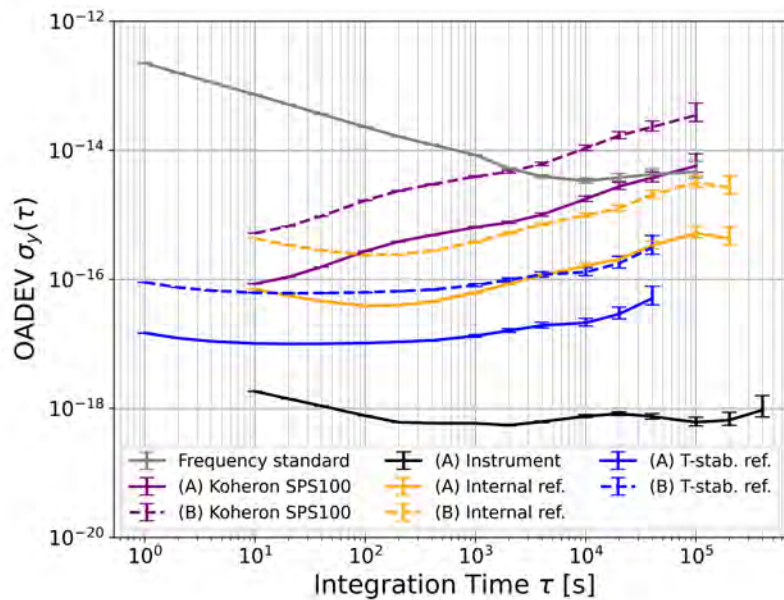


Figure 10.2: Frequency instability limits imposed by measured voltage reference noise. Extra-polated from measurements using beam property scenarios A (solid) and B (dashed) defined in Table 10.1. When a small beam diameter (scenario B) and/or an insufficiently stable voltage reference is used, voltage reference drifts and fluctuations represent a relevant frequency stability limitation. In that case, relative intensity stabilization with a common voltage can alleviate the limitation, which is illustrated in Figure 10.3. T-stab. ref. = temperature-stabilized voltage reference (see text).

According to the dashed purple curve in Figure 10.2, the small linear power supply would impose an instability limit above 10^{-14} for scenario B. Also for scenario A, the limitation would be stringent. This finding confirms the necessity to employ voltage regulators which are adapted to this application. As of the internal reference of the power stabilization unit, its OADEV for the less stringent scenario A stays below 10^{-15} for all of the investigated integration times. This is consistent with the finding that interrogation power stability is not limiting frequency stability of the unperturbed optical standard. For scenario B, however, the voltage

¹Koheron SPS100

reference would set a relevant stability limit. The temperature-stabilized voltage reference would not be limiting in either scenario, as indicated by the two blue curves. Finally, the multimeter does not limit the measurement (black curve). For the sake of readability, the instrument limit is plotted only for scenario A.

10.2.2 Perturbation and Compensation

The reduction of frequency sensitivity to reference voltage achieved through relative intensity stabilization is investigated with three measurements. They are shown in Figure 10.3. In the top part of the figure, fractional frequency stability is plotted in terms of Allan Deviation. In the bottom part, representative segments of fractional frequency measurements are shown.

In a first measurement, the mitigation laser is turned off. A slow sinusoidal perturbation is applied on the reference voltage, which affects the stabilization of interrogation power. This measurement is shown in orange and labeled *Perturbed*. In a second measurement, the same perturbation is applied on the voltage reference. This time, however, the mitigation laser is utilized. This measurement is plotted in green and labeled *Mitigated*. Finally, a third measurement is made without perturbation and without mitigation laser. The corresponding ADEV is plotted in blue and labeled *Baseline*. This last measurement represents the baseline stability that is not limited through the light shift effect.

The ADEVs in Figure 10.3 show that frequency stability for a mitigated perturbation (second measurement, in green) is close to the one of the unperturbed system (third measurement, in blue). The light shift induced by voltage reference changes is almost entirely compensated by the mitigation laser. At 1000 s integration time, stability is improved by over an order of magnitude, indicating that the mitigation laser reduces the clock frequency sensitivity to reference voltage drifts by at least 10 dB. This figure could be even higher. Just like the baseline stability, mitigated operation is limited by white frequency noise. The residual uncompensated contribution of the light shift through the reference voltage perturbation is thus buried in the intrinsic noise of the passive frequency standard.

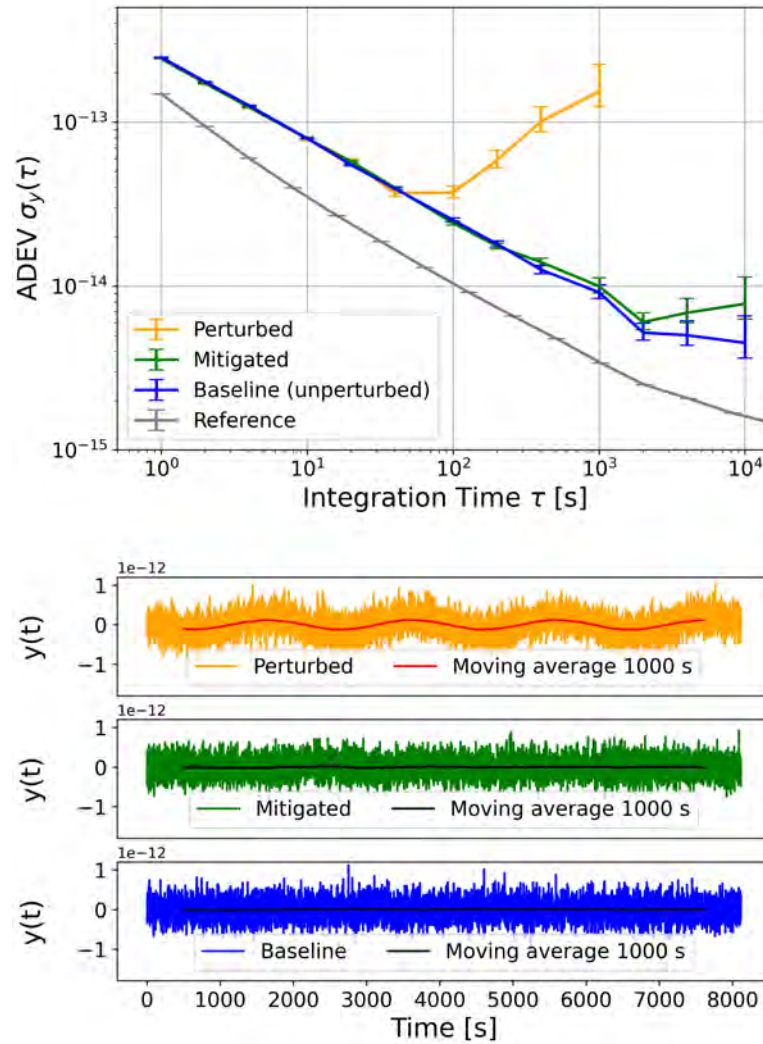


Figure 10.3: Allan Deviation (top) and frequency traces (bottom) for a sinusoidal voltage reference perturbation. Measurements without (orange) and with (green) AC Stark shift mitigation in comparison with baseline stability (blue) without perturbation. Shortened, representative frequency trace segments are plotted.

10.3 Temperature Sensitivity of Electronics

Different effects that potentially limit frequency stability are driven by temperature variations. Unless a sub-system is individually stabilized in temperature, it is subject to the fluctuations of air temperature in the laboratory. This makes it difficult to distinguish different effects that are all correlated with laboratory temperature. For this reason, independent temperature control for the breadboard helps to dissociate effects impacting the free-space setup from the ones impacting the fibered part. Furthermore, temperature control on a smaller scale permits to characterize the temperature sensitivity of individual components. This is done for the power stabilization units in what follows.

10.3.1 Empirical Sensitivity Coefficient

Each power stabilization unit is equipped both with a resistive heater and a negative temperature coefficient (NTC) thermistor. Optical power is then stabilized to an arbitrary setpoint. The temperature of the units is varied by operating the resistive heaters at two different electrical power levels and in off-state. Temperature is logged by measuring NTC resistance. At the same time, the commercial photodetectors monitor optical power out-of-loop. They do not experience the temperature changes applied to the devices under test. This makes their responsivity variations negligible with respect to the ones of the devices under test. The measured temperature and optical power (out-of-loop) are plotted against time in the top part of Figure 10.4 below.

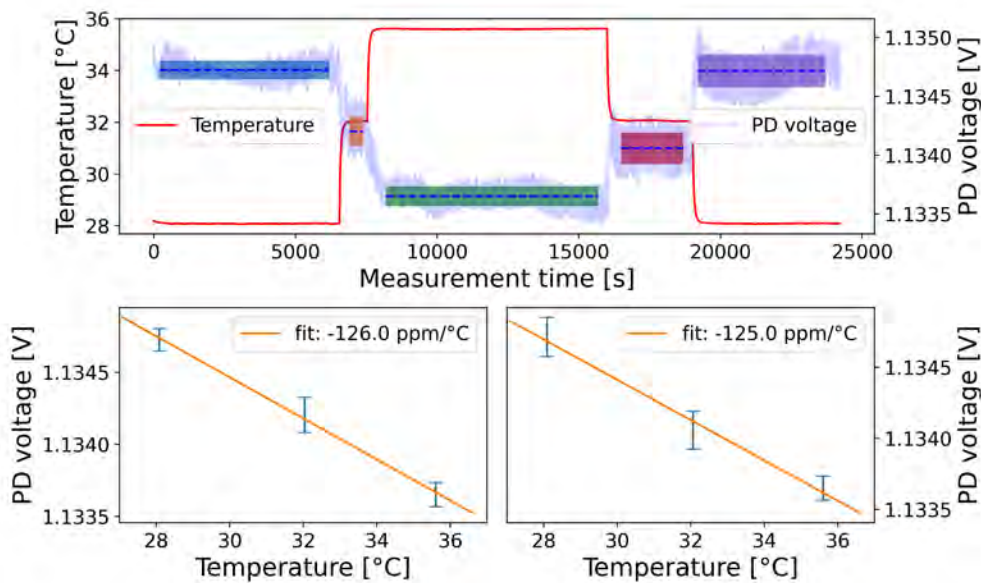


Figure 10.4: Temperature sensitivity of the power stabilization unit for 778.1 nm wavelength. Device temperature and photodiode voltage against time (top), and linear regression for temperature increase (bottom left) and decrease (bottom right). PD = photodiode.

The top part of Figure 10.4 shows that optical power, which is proportional to the measured photodiode voltage, depends on the temperature of the device under test. For each segment featuring steady temperature, photodiode voltage is indicated by a dashed line. The latter is surrounded by a semi-transparent banner highlighting the standard deviation ($\pm 1\sigma$) of the samples within the segment. Simple linear regression is calculated and shown in the bottom part of the figure to express the power dependence on temperature. It gives a sensitivity coefficient of about -125 ppm/ $^{\circ}\text{C}$. A temperature increase (bottom left) and decrease (bottom right) result in the almost identical coefficient, excluding possible hysteresis phenomena.

The compounded empirical sensitivity coefficient of -125 ppm/ $^{\circ}\text{C}$ is compatible with the photosensitivity temperature dependence specified by the photodiode manufacturer. It is higher than the temperature drift coefficients of the relevant electronic components. Therefore,

it is suspected that the temperature sensitivity of the electronics is limited by the temperature sensitivity of the silicon photodiode. The sign of the measured coefficient is negative. This means that the detection efficiency of the device under test (in-loop) increases with increasing temperature.

The power stabilization unit for 1556.2 nm wavelength is tested in the same way. Its temperature sensitivity is found to be much smaller than the one of the 778.1 nm board. This makes it difficult to establish a meaningful value for its coefficient. However, this means that the practical implementation of the concept using 1556.2 nm wavelength is not limited by the power stabilization unit used for the mitigation beam.

10.3.2 Frequency Instability Limits

Clock frequency instability limits are extrapolated from the empirical detection efficiency sensitivity coefficient measured for the 778.1 nm electronic circuit. Based on representative breadboard temperature measurements acquired for a system in operation, the expected impact on clock frequency is quantified assuming certain beam properties. The same scenarios as for the voltage reference measurements are used (Table 10.1). The resulting ADEVs are showcased in Figure 10.5. They are calculated on the basis of two different temperature measurements. In one case, the breadboard temperature is not regulated, whereas in the other case, it is stabilized to approximately 30°C using water cooling. Without regulation, temperature in steady state is slightly above 30°C. For both cases, temperature is plotted as an offset from its mean.

For the less stringent scenario A, the extrapolated instability limits are below or around 10^{-16} for the investigated integration times. This suggests that the temperature dependence of the 778.1 nm board detection efficiency does not represent a relevant performance limitation for the frequency standard. For scenario B, however, the temperature sensitivity of the power detection unit sets an instability limit around 10^{-15} when the breadboard temperature is not controlled. Without air conditioning in a laboratory environment, the limitation could become relevant. Nonetheless, active stabilization of breadboard temperature is sufficient to suppress this effect, given that it improves temperature stability for integration times larger than roughly half an hour. For shorter integration times, the stabilization introduces additional noise, but has no adverse effect on frequency stability.

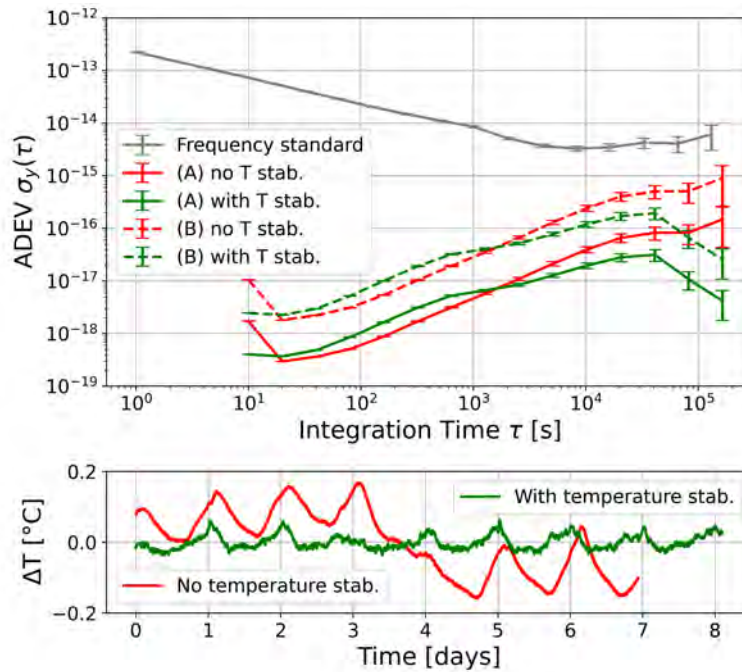


Figure 10.5: Measured breadboard temperature (bottom) without (red) and with (green) active control. Corresponding clock frequency instability limits (top) assuming the beam property scenarios A and B defined in Table 10.1 and the measured power stabilization electronics temperature sensitivity reported in Figure 10.4. It is concluded that the temperature sensitivity of the electronics does not constitute a practically relevant limitation of clock frequency stability.

10.4 Stability Budget

The frequency standard is operated with and without mitigation laser. In both cases, no external perturbation is applied and the optical breadboard temperature is stabilized to a setpoint of 30°C as indicated by the water cooler. Monitoring of different operational parameters allows to establish the stability budget presented in Figure 10.6 below.

The OADEV of the optical reference is plotted in gray in the upper part of Figure 10.6. The OADEVs of the frequency standard without and with the mitigation laser are plotted in blue and green, respectively. Frequency stability is equivalent in the two cases. The optical breadboard temperature is plotted in the lower part of the figure and shows comparable diurnal excursions for both measurements.

Optical power is monitored out-of-loop, but the measurement is not included in the stability budget. The reason for this is an important drift of measured interrogation power, which is likely due to alignment instability of the D-shaped mirrors. Plotted as an OADEV, the light shift extrapolated from the power measurement would result in a limitation roughly compatible with the actually observed frequency stability without mitigation laser. However, when analyzing the clock frequency alongside measured optical power, no correlation can be seen. This makes a clock stability limitation by the light shift unlikely.

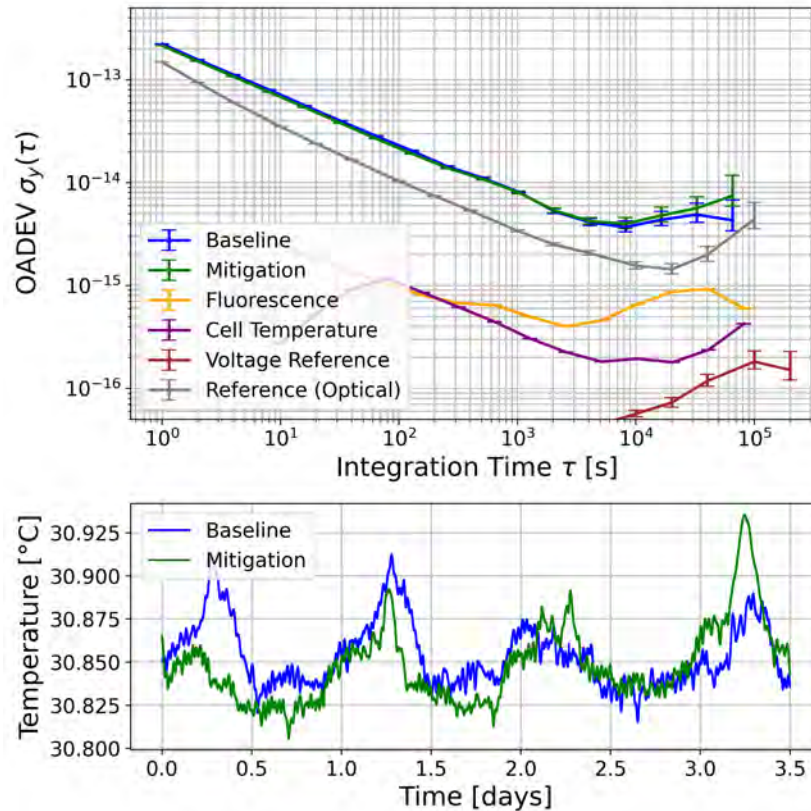


Figure 10.6: Stability Budget (top) and box temperature (bottom) with and without the mitigation laser. Although the temperature of the optical breadboard is stabilized, diurnal variations of up to 100 mK are measured. The addition of the mitigation laser does not degrade clock frequency stability. As frequency stability is not limited by the AC Stark effect, it cannot be determined whether the mitigation laser has a positive impact on attainable frequency stability. The plotted OADEVs (labeled Baseline and Mitigation) are not corrected for the measurement noise of the optical reference (labeled Reference).

Moreover, the interrogation power in the vapor cell is estimated using the measured fluorescence signal amplitude. It indicates that the contribution of the interrogation light shift lies slightly below 1 part in 10^{15} . The contribution due to the self-collision shift, which is determined with an out-of-loop cell temperature measurement, is even smaller. Finally, the clock frequency instability limit due to the voltage reference is indicated. Since optical power is relatively low and the beam waist radius is large, the voltage reference stability is not limiting in the present case.

Rather than by the light shift, frequency stability is suspected to be limited by effects linked to the phase modulation using the EOM. Even though RAM is detected and canceled, the modulator can represent a noise source degrading long-term frequency stability. The detailed analysis of the observed stability limitation, however, is out of scope of this thesis focusing on the light shift. However, it remains an important research topic that needs to be addressed for the further improvement of the two-photon clock.

10.5 Chapter Conclusions

This chapter described the implementation of relative intensity stabilization using a 778.1 nm interrogation and a 1556.2 nm wavelength mitigation beam. As the frequency standard is not limited by the AC Stark effect, it can unfortunately not be determined whether the addition of a 1556.2 nm wavelength mitigation laser has the potential to improve frequency stability. Nevertheless, by introducing a deliberate perturbation of the common voltage reference, reduced clock frequency sensitivity to voltage drifts is demonstrated. Moreover, by measuring the temperature sensitivity of the power stabilization electronics, a potential technical limitation of the method is quantified and qualified as negligible.

Finally, a stability budget of the frequency standard with and without mitigation beam was presented. It is concluded that the addition of a 1556.2 nm wavelength mitigation laser has no adverse effect regarding frequency stability.

Although no improvement of frequency stability can be observed for an unperturbed system with the mitigation laser, it has a beneficial impact on frequency accuracy. This is the subject of the next chapter.

11 Absolute Frequency

This chapter discusses the absolute frequency measurement of the ^{87}Rb $5S_{1/2} \rightarrow 5D_{5/2}$ two-photon transition ($F_g = 2$) \rightarrow ($F_e = 4$) hyperfine component. This transition frequency has been measured and reported previously [13, 36, 51, 83, 85, 119]. The previous measurements shall be compared to the one presented here.

Different effects are known to induce systematic frequency shifts on the $5S_{1/2} \rightarrow 5D_{5/2}$ transition. The magnitudes of these effects are quantified and subtracted from the measured clock frequency. Whereas the previously reported measurements were corrected for the contribution of the AC Stark effect by calculation, no arithmetic correction is done here. Instead, the systematic frequency shift of the interrogation laser is compensated physically by the mitigation laser.

11.1 Absolute Frequency Measurement

To determine the atomic resonance frequency, the absolute frequency of the clock laser f_{CW} is measured first. This is done by averaging over a period of two hours and is described in what follows. In a second step, the different uncompensated systematic transition frequency shifts are estimated in 11.2. Finally, the second harmonic of the clock laser frequency is corrected for these uncompensated shifts in 11.3. This results in the atomic resonance frequency, which is then compared to previously reported measurements.

11.1.1 Optical Frequency Domain

When locking the frequency comb, the mode number n of the comb line that is offset-locked to the reference clock laser determines the range of possible repetition rates. The repetition rate that serves as the microwave frequency output of the reference optical clock is brought to 100 MHz as closely as possible.

The approximate frequency f_{CW} of the CW laser which is frequency-locked on the atomic transition is known thanks to literature values [13, 36, 51, 83, 85, 119]. Both the AC Stark effect and the self-collision shift impact f_{CW} by a few kHz each. A single comb line, in contrast, corresponds to a shift of f_{CW} of 200 MHz.

Nez et al. [85] have measured the frequency of the ($F_g = 2$) \rightarrow ($F_e = 4$) hyperfine component of the ^{87}Rb $5S_{1/2} - 5D_{5/2}$ transition to 385 284 566 366.3 (8.0) kHz. Half of this value is assumed for the fundamental CW laser, namely $f_{CW} = 192\,642\,283.183$ MHz. This optical frequency beats with the closest comb mode, producing the frequency f_{lock} , which is of either positive or negative sign. The beat note f_{lock} is locked to an arbitrary value. The relation between f_{CW} and its nearest comb line with mode number n is written as

$$f_{CW} = (\pm |f_{CEO}| + n \cdot f_{rep}) \pm |f_{beat}| \quad (11.1)$$

The carrier-envelope-offset frequency f_{CEO} is fixed to 10 MHz. The sign can be chosen freely. The mode number of the comb line closest to the CW laser is found by dividing the CW frequency by the repetition rate

$$n = \text{mod}(f_{CW}/f_{rep}) = 1\,926\,423 \quad (11.2)$$

Knowing n , the offset of f_{CW} from $n \cdot f_{rep}$ is calculated. By rearranging Eq. (11.1) we find

$$f_{CW} - n \cdot f_{rep} = \pm f_{CEO} \pm f_{beat} = -16.817 \text{ MHz} \quad (11.3)$$

Eq. (11.3) defines the target beat frequency f_{lock} that leads to the desired repetition rate of 100 MHz. In practice, f_{lock} must be smaller than half of the repetition rate, which is 50 MHz. Moreover, f_{lock} must not be too close to zero as this would make detection and filtering difficult. A beat frequency around 30 MHz is desirable. By choosing the sign of f_{CEO} as positive and the one of f_{lock} as negative, Eq. (11.3) is fulfilled with $|f_{beat}| \approx 26.817$ MHz. The negative sign for f_{lock} indicates that the clock laser frequency will be found to the left of the n^{th} comb line, as illustrated in Figure 11.1.

11.1.2 Radio Frequency Domain

The comb repetition rate f_{rep} is determined by comparing it to the output of an active hydrogen maser¹, as described in 8.3. The phase of the maser output at 10 MHz is tracked with respect to an atomic timescale referenced to GNSS. Tracing back the comb repetition rate to GNSS allows to calculate the maser frequency offset and makes an accurate frequency measurement possible.

The sign of f_{CEO} is detected by the optical frequency comb. The frequency f_{CEO} is locked to 10 MHz using a comb-internal oscillator that is provided with a 10 MHz reference signal from

¹iMaser 3000, Safran Timing Technology SA

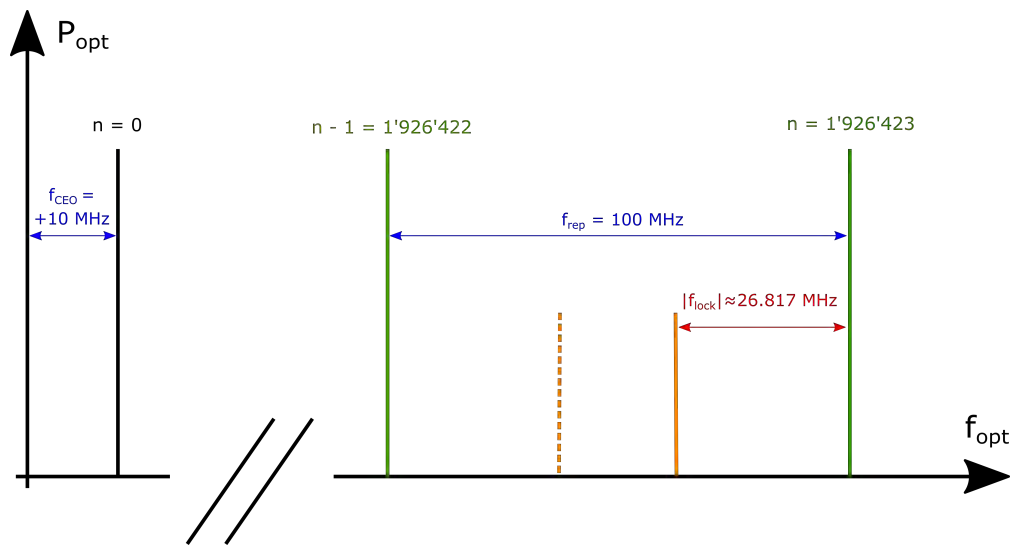


Figure 11.1: Configuration of the frequency comb resulting in a repetition rate of $f_{rep} = 100$ MHz. The optical reference frequency f_{CW} is represented by the solid vertical bar drawn in orange. It is given by the atomic resonance frequency of the two-photon transition and is locked to the closest comb mode by stabilizing the beat frequency f_{lock} (see also Figure 8.1). The sign of f_{CEO} and the parameters f_{lock} and n are chosen freely.

the same active hydrogen maser which is also used to measure the comb repetition rate.

11.1.3 Measurement Chain Referenced to UTC

A multi-level measurement chain establishes a link between the clock laser frequency f_{CW} and GNSS. It allows to trace back the atomic resonance frequency to UTC(r). The different elements of the chain and the links in between are listed in Table 11.1 below. In addition to the elements that have been introduced previously, the measurement chain consists of an atomic timescale and a GNSS receiver. Moreover, publicly available data from BIPM² allows to trace back to UTC(r) the received GNSS timing signals. The individual links of the chain are described in the following paragraphs.

Optical Frequency Standard to Optical Reference

The clock laser frequency is measured by beating it against a mode of the frequency comb that is locked to another rubidium two-photon standard as described in 8.3. A specific harmonic of the resulting beat note is filtered and measured. The frequency of this beat note is composed of a natural multiple of the comb repetition rate and the frequency offset between f_{CW} and the closest comb mode. In particular, it is $100 \cdot f_{meas} = 14 \cdot f_{rep} + |f_{beat}|$.

The mode number n of the comb line contributing to the beat note has been calculated above. Relying on the calculated value of n implies the assumption that the transition frequency

²Bureau International des Poids et Mesures (BIPM), <https://www.bipm.org/en/time-ftp/utc>

Element in chain	Chain link measurement	Phase/time	Sampling
Optical frequency standard ↓	Beat note CW & comb	Phase	$\tau_s = 1$ s
Reference clock (comb line) ↓	$f_{rep}/10$ vs. maser 10 MHz	Phase	$\tau_s = 1$ s
Active hydrogen maser ↓	TIC measurement of PPS	Time offset	$\tau_s = 60$ s
Timescale output ↓	GNSS receiver	Time offset	$\tau_s = 16$ min.
REFSYS UTC(USNO) ↓	BIPM database	Time offset	$\tau_s = 1$ day
UTC _r - UTC(USNO)			

Table 11.1: Overview of the measurement chain that links to UTC(r) the optical frequency of the clock laser f_{CW} . The sampling period τ_s is indicated for the respective phase or time offset measurements. Corresponding frequency offsets between chain links are reported in Table 11.3, while measurement uncertainties are summarized in Table 11.2. CW = continuous-wave (laser), TIC = time interval counter.

measurement is not offset by 200 MHz or a multiple thereof. In relative terms, this corresponds to a natural multiple of 5×10^{-7} . In comparison to the total measurement uncertainty that will be evaluated in what follows, such large offsets are extremely unlikely. It is concluded that, based on previous measurements of the two-photon transition frequency, the comb mode number n is known with satisfactory confidence.

The uncertainty of this measurement is given by the resolution of the phase comparator. At $\tau = 1$ s, it is specified to 2×10^{-12} . The measurement reveals a beat frequency of $f_{beat} \approx 26.821$ MHz. This frequency is very similar to the one imposed for the lock of the optical frequency comb on the reference clock laser, i.e. $f_{lock} \approx 26.817$ MHz. The difference $f_{beat} - f_{lock} \approx 4$ kHz implies that the clock laser frequencies of the device under test and the reference two-photon clock are similar but are both subject to different systematic frequency shifts. No accuracy budget is established for the reference two-photon clock.

Optical Reference to Active Hydrogen Maser

The optical reference is measured against an active hydrogen maser via a self-referenced frequency comb. Its repetition rate $f_{rep} \approx 100$ MHz is divided by 10 and measured against the 10 MHz output of the maser with a phase comparator. In particular, the frequency ratio

between the two standards is evaluated. For the day of measurement it is found that

$$\frac{f_{maser}}{f_{rep}/10} - 1 = +3.1542 \times 10^{-11} \quad (11.4)$$

Uncertainty is given by the frequency instability of the active hydrogen maser at the integration time of 2 hours, which is specified to 2×10^{-15} by the manufacturer.

Active Hydrogen Maser to Timescale

The active hydrogen maser is not steered to GNSS and has thus an a priori unknown frequency offset with respect to UTC. The maser is measured against the output of a timescale. This timescale [46] combines different atomic clocks in order to yield a time output, which is given by a frequency synthesizer providing PPS and 10 MHz outputs.

To measure the frequency offset between the maser and the timescale, their PPS outputs are compared to each other with a time interval counter (TIC). This is done at a sampling period of 60 seconds and over the course of one day. Thanks to this measurement performed on the same day as the one of the optical frequency standard against the optical reference, the evolution of the PPS offset between the maser and the timescale is determined. The slope of the time offset is -2.538×10^{-12} . The frequency ratio between the maser and the timescale is directly deduced from this slope as

$$\frac{f_{timescale}}{f_{maser}} - 1 = +2.538 \times 10^{-12} \quad (11.5)$$

The uncertainty of this measurement is given by the frequency instability of the active hydrogen maser at the integration time of 1 day, which is specified to 2×10^{-15} .

Therefore, the compounded frequency ratio between the timescale and the reference clock frequency is

$$\frac{f_{timescale}}{f_{rep}/10} - 1 \approx \left(\frac{f_{timescale}}{f_{maser}} - 1 \right) + \left(\frac{f_{maser}}{f_{rep}/10} - 1 \right) = +3.408 \times 10^{-11} \quad (11.6)$$

This frequency ratio must be taken into account for scaling the measured clock laser frequency with respect to UTC(r).

Timescale Output to GNSS

The timescale output is traced back to a realization of UTC provided by GNSS. More specifically, GPS system time is used, i.e. REFSYS UTC(USNO). The latter is received by a generic GNSS receiver with a sampling period of 16 minutes. For simplicity, other GNSS constellations are not accounted for. Based on the CGGTTS-Version 2E standard for GNSS time transfer, the timing offset between UTC(USNO) and the timescale is determined.

From the different satellites from which signals are received, the time difference between satellite and system reference time is obtained. As only time and no frequency data is accessible from this comparison, the uncertainty on the frequency offset between the received GPS system time and the underlying UTC(USNO) is estimated. This is done by identifying an upper uncertainty bound.

A conservative estimate for the uncertainty is made based on the observation that within 24 hours, the timing offset stays within a range of 5 ns. The same can thus be said for the measurement interval of 2 hours. In the worst case, a change of timing offset of 5 ns within 2 hours corresponds to a fractional frequency offset of $\approx 7 \times 10^{-13}$.

GNSS to UTC(r)

In a final step, REFSYS UTC(USNO) is compared to UTC and UTCr, which is the rapid realization of UTC, which is disseminated via the BIPM Time Department Data Base. For the day preceding the measurement (MJD=60509), the difference UTCr – UTC(USNO) is reported to +0.2 ns. For the day of the measurement (MJD=60510) and the following day (MJD=60511), the difference is reported to 0.0 ns. Based on this small evolution of time offset, the contribution to the uncertainty of the frequency measurement is quantified to 2×10^{-15} .

Measurement Uncertainty

The measurement uncertainties associated with the chain links described above are summarized in Table 11.2. The dominant source of uncertainty is linked to the received GPS signals. The time offsets between the timescale and REFSYS UTC(USNO) do not directly reveal a frequency offset, but allow to establish the uncertainty bound of $< 7 \times 10^{-13}$ found above. In absolute terms, this represents an uncertainty of < 270 Hz on the ≈ 385 THz frequency of the rubidium two-photon transition.

Chain Link	Given by	Uncertainty
Phase measurement	Phase comparator limit at $\tau = 2$ hours	2.4×10^{-14}
Maser to timescale	Maser frequency stability at $\tau = 1$ day	2×10^{-15}
Timescale to GNSS	Frequency stability of timescale at $\tau = 1$ day	2×10^{-15}
GNSS to UTC(r)	REFSYS UTC(USNO) as by CGGTTS-Version 2E	$< 7 \times 10^{-13}$
UTC(USNO) vs. UTC(r)	Daily time offset as reported by BIPM	2×10^{-15}
TOTAL	(dominated by GNSS)	$< 7 \times 10^{-13}$

Table 11.2: Relative uncertainties in the clock laser frequency measurement with respect to UTC(r) listed for the different links of the measurement chain.

11.1.4 Measurement of Clock Laser Frequency

Using the method described above, the relevant radio frequencies are measured. They are reported in Table 11.3 below. The sign of f_{beat} is determined by tuning optical power and rubidium vapor pressure to induce AC Stark and self-collision shifts whose respective signs are known. A negative sign is found. With this piece of information, the measured frequencies are inserted into Eq. (11.1), which results in the looked after clock laser frequency f_{CW} . The quantity $2 \cdot f_{CW}$ represents the perturbed atomic resonance frequency. It is affected by the systematic shifts that are quantified in the following paragraphs.

Frequency (or other)	With respect to	Value in Hz (or ratio/number)
f_{rep}	maser	100 000 000.000 000
$(f_{timescale}/(f_{rep}/10))$	-	$(3.408 \cdot 10^{-11})$
f_{rep}	GNSS	100 000 000.003 408
f_{CEO}	maser	10 000 000.000 000
f_{CEO}	maser	10 000 000.000 341
$100 \times f_{meas}$	maser	1 426 820 636.258
f_{beat}	maser	26 820 636.258
f_{beat}	GNSS	26 820 514.259
(comb mode number n)	-	(1 926 423)
f_{CW}	GNSS	192 642 283 185 929

Table 11.3: Determination of the clock laser frequency f_{CW} . As the frequency measurement is made with respect to an active hydrogen maser, it must be corrected by the frequency ratio between UTC(r) and the maser. The clock laser frequency f_{CW} represents the atomic resonance frequency including its systematic shifts.

11.2 Systematic Resonance Frequency Shifts

The relevant systematic frequency shifts are estimated either by measurement or by calculation. Unless specified, the calculations refer to the theoretical framework discussed in 4.5. The different systematic shifts are then summed up to establish the accuracy budget in 11.3.

For all effects driven by vapor pressure, an uncertainty of $\pm 3^\circ\text{C}$ is taken for the absolute cell temperature. The latter is assumed to correspond to the selected working point of 90°C .

11.2.1 Self-Collision Shift

The self-collision shift rate is evaluated experimentally by tuning cell temperature to five different setpoints between 80°C and 95°C . For each setpoint, clock frequency is measured

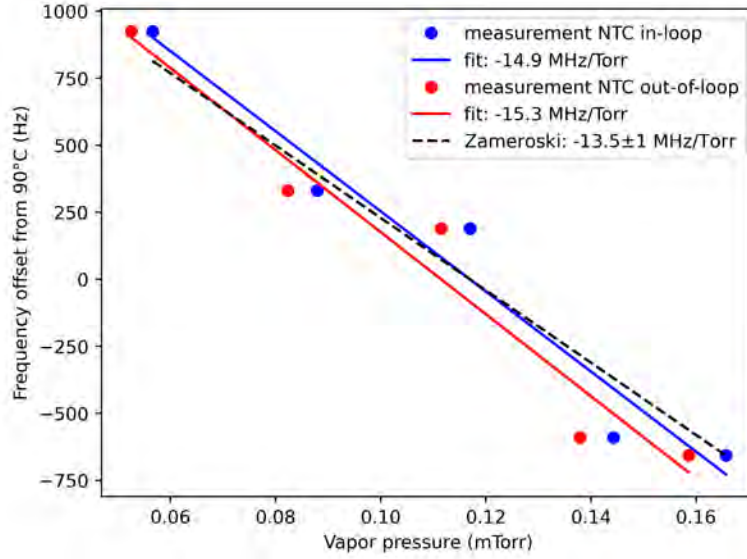


Figure 11.2: Measurement of rubidium self-collision shift. Shift rates are given in terms of 778.1 nm wavelength photon frequency (385 THz). Two temperature measurements using different NTC resistors of the same model lead to similar shift rates that are compatible with the one reported by Zamoski et al. [117].

and averaged over a period of about ten minutes. Frequency is then plotted for the rubidium vapor pressure corresponding to the different temperatures. Vapor pressure is calculated in function of cell temperature using Eq. (4.7).

As shown in Figure 11.2, linear regression gives then the measured self-collision shift rate $^{meas}\gamma_{S,Rb}$. No error bars are plotted in the vertical axis since the standard deviation of measured frequency is negligible with respect to the frequency differences between measurement points. Rather than by frequency, the measurement uncertainty is given by the determination of cell temperature. In the blue data points in Figure 11.2, the cell temperature is assumed to correspond precisely to its setpoint. An out-of-loop measurement using the same type of NTC resistor, which is plotted in red, leads to different temperature values. The NTC resistors are calibrated with the model specific resistance-temperature curve provided by the manufacturer. The self-collision shift rate is calculated by averaging the two measurements, leading to

$$^{meas}\gamma_{S,Rb} = -15.1(\pm 0.2) \text{ MHz/Torr} \quad (11.7)$$

With the cell temperature of 90°C and the assumed $\pm 3^\circ\text{C}$ uncertainty, the frequency shift due to the Rb-Rb collisions is estimated to

$$\Delta f_{Rb-Rb} = -1770(\pm 350) \text{ Hz} \quad (11.8)$$

While the goal of this chapter is the quantification of systematic frequency shifts, it is worthwhile also considering stability. The self-collision shift, as mentioned before, motivates particular attention to cell temperature stability [76]. The derivative of Eq. (4.7) in combination with the shift rate allows to calculate the fractional frequency sensitivity coefficient of cell

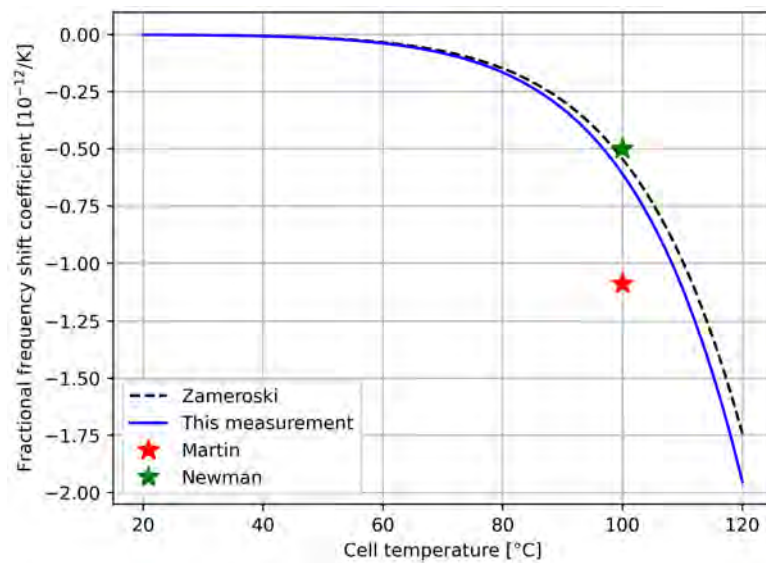


Figure 11.3: Self-collision shift fractional frequency sensitivity coefficient against cell temperature. The coefficient extrapolated for 100°C agrees well with the one reported by Newman et al. [83], which is approximately two times smaller than the one reported by Martin et al. [74]. The sensitivity coefficient is extrapolated from the measurement reported in Figure 11.2.

temperature, which is plotted in Figure 11.3. The extrapolated sensitivity coefficient at 100°C cell temperature corresponds well to the ones reported by [117] and [83] for ^{85}Rb and ^{87}Rb , respectively. In contrast, [76] reported a two times higher sensitivity coefficient for ^{87}Rb .

11.2.2 Helium Collision Shift

The helium concentration within the vapor cell is estimated in two different ways: with a leakage calculation and with a linewidth broadening measurement. The frequency shift corresponding to the estimated helium partial pressure is then estimated with the helium collision shift rate reported by [117] (see Eq. (4.10)). For the linewidth broadening method, the helium broadening rate reported the same source is used (see 4.9).

Leak Rate Calculation

With the vapor cell geometry and material properties³, the helium leak rate is calculated as a function of helium partial pressure difference between the inside and outside of the cell⁴. The helium concentration within the cell is obtained by integrating the leak rate over the total uptime of cell heating. It is assumed that the cell was free of helium at the time of production. Furthermore, the leak rate at ambient temperature is neglected. The helium partial pressure

³Cylindrical glass-blown cell with a 10 mm optical path length, a 9.5 mm inner diameter and a 1.1 mm wall thickness. Material: Pyrex (also known as borosilicate glass)

⁴The initial calculation by Matthieu Pellaton is gratefully acknowledged in this context.

at the time of initial operation $t = 0$ is thus

$$P_{in}^0 = 0 \quad (11.9)$$

Unless the vapor cell is exposed to an environment with increased helium concentration, the helium partial pressure inside the cell will not exceed the partial helium pressure in the atmosphere. The latter is $P_{out} = 3.95$ mTorr [117], which means that the maximum possible helium partial pressure inside the cell is also

$$P_{in}^{max} \equiv P_{out} = 3.95 \text{ mTorr} \quad (11.10)$$

Using the shift rate given in Eq. (4.10), the maximum frequency shift due to helium permeation is calculated to

$$\Delta f_{He}^{max} = Z_{am.} \gamma_{S,He} \cdot P_{in}^{max} = 4010(\pm 140) \text{ Hz} \quad (11.11)$$

The change in helium partial pressure is proportional to the difference of helium partial pressure inside and outside of the cell, meaning

$$\frac{dP_{in}}{dt} = \alpha \cdot (P_{out} - P_{in}) \quad (11.12)$$

Rearranging Eq. (11.12) above leads to the differential equation

$$-\alpha \cdot dt = \frac{dP_{in}}{P_{in} - P_{out}} = \frac{f'(P_{in})}{f(P_{in})} \quad [\text{with } f(P_{in}) = P_{in} - P_{out}] \quad (11.13)$$

that is integrated by letting

$$\ln(P_{in} - P_{out}) = -\alpha t + C \quad (11.14)$$

Taking the exponential form of Eq. (11.14) above leads to

$$P_{in} = P_{out} + C' e^{-\alpha t} \quad (11.15)$$

With the assumption made in Eq. (11.9) that at $t = 0$ the helium partial pressure inside the cell is zero, we find $C' = -P_{out}$. This leads to the time-dependent expression for the helium partial pressure inside the cell

$$P_{in} = P_{out} (1 - e^{-\alpha t}) \quad (11.16)$$

The leak rate α must be determined numerically. It depends on the geometry and material properties of the cell. It is expressed as [96]

$$\alpha = K \frac{A}{d \cdot V} [\text{at } P_{ref}] \quad (11.17)$$

where K is the permeation constant that depends on material and temperature, whereas A , d and V designate the vapor cell surface area, wall thickness and inner volume, respectively. The units used to express the permeation constant K differ among sources. Independently of the chosen units, K expresses the temporal rate of a volume of gas that permeates a substrate with a given surface area and thickness. As the rate is inversely proportional to the substrate thickness and proportional to surface area, the volumetric permeation rate reduces to units of surface per time. However, volume does not quantify by itself the number of particles that have permeated the substrate. This explains by the circumstance that the particle density in a gas is a function of pressure. Therefore, the permeation constant is given for a certain reference pressure defining the mass density of the gas. In the present case, the pressure that defines the number of particles per volume is the one outside the cell. Unlike P_{out} , however, it is the total vapor pressure rather than the helium partial pressure. The reference pressure is therefore defined as

$$P_{ref} \equiv 1 \text{ atm} = 760 \text{ Torr} \quad (11.18)$$

The permeation constant of Pyrex⁵ is taken as the value reported by [59], namely

$$K_{100^\circ\text{C}} = 3.0 \times 10^{-8} \text{ mm}^2/\text{s} \quad (11.19)$$

As the cell was operated at 100°C before switching to 90°C, the permeation constant $K_{100^\circ\text{C}}$ does not need to be scaled with temperature. The leak rate is determined with Eq. (11.17) to

$$\alpha_{100^\circ\text{C}} = 1.72 \times 10^{-8} \text{ s}^{-1} \quad (11.20)$$

Inserting the leak rate into Eq. (11.16) and taking the time of operation at 100°C as $t = 300$ days gives the expected helium partial pressure inside the cell, namely

$$P_{in}(t = 300 \text{ days}) = P_{out} \cdot (1 - 0.64) = 1.42 \text{ mTorr} \quad (11.21)$$

An uncertainty of $\pm 20\%$ is placed on the leakage calculation, which leads to a helium partial pressure of

$$P_{He,A} = 1.42 (\pm 0.28) \text{ mTorr} \quad (11.22)$$

The result of this calculation will be compared to the helium partial pressure obtained from linewidth measurements described in what follows.

⁵The permeation constant itself is the product of the diffusion coefficient and solubility, which are reported for Pyrex in [59].

Linewidth Broadening Measurement

Collisions between helium and rubidium atoms not only shift the atomic resonance frequency, but they also broaden the transition linewidth. A linewidth difference measurement thus allows to estimate the helium concentration within the vapor cell. The atomic linewidth was measured right after the vapor cell had been put in operation. A second linewidth measurement is performed eight days before the absolute frequency measurement. The difference between the Lorentzian fitted FWHM values is interpreted as the line broadening due to helium contamination. As the cell had not been heated before being included in the setup, it is assumed that the amount of helium which permeated into the cell between fabrication and start of operation is negligible. Moreover, it is assumed that the freshly sealed vapor cell was free from helium atoms and other contaminants. Neglecting the potential permeation of other contaminants and their respective collision shifts, the helium collision frequency shift determined by line broadening is

$$P_{He} = \frac{\Delta\gamma_{FWHM}}{Z_{am} \cdot \gamma_{B,He}} \quad (11.23)$$

Both linewidth measurements are done with the same experimental parameters⁶ and result in FWHM linewidths of 441(±3) kHz and 498(±10) kHz for the initial and the follow-up measurement, respectively. This results in a FWHM difference of $\Delta\gamma_{FWHM} = 57(\pm 10)$ kHz. The uncertainty of the linewidth measurement dominates over the uncertainty of the shift and broadening rates. The helium partial pressure inside the cell is estimated to

$$P_{He,B} = 2.23(\pm 0.40) \text{ mTorr} \quad (11.24)$$

which is in the same order of magnitude as the value obtained by leakage rate calculation (see Eq. (11.22)).

Compounded Helium Concentration and Shift

The two helium partial pressure estimations obtained through leakage calculation ($P_{He,A}$) and linewidth measurement ($P_{He,B}$) are weighed equally. This leads to a compounded value of

$$P_{He} = \frac{1}{2}(P_{He,A} + P_{He,B}) = 1.83(\pm 0.49) \text{ mTorr} \quad (11.25)$$

Finally, multiplying P_{He} by the shift rate in Eq. (4.10) results in the frequency shift due to He-Rb collisions

$$\Delta f_{He} = Z_{am} \cdot \gamma_{S,He} \cdot P_{He} = +1880(\pm 500) \text{ Hz} \quad (11.26)$$

⁶10 mW of optical power with a 11 Hz frequency and 50 mVpp amplitude symmetrical triangular ramp on the laser current modulation. This ramp corresponds to a scanning speed of approximately 170 MHz/s.

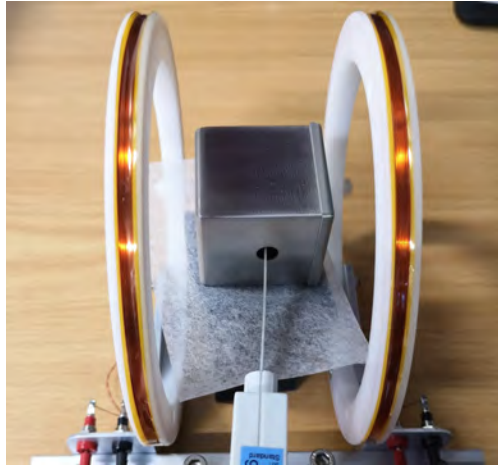


Figure 11.4: The magnetic shielding is tested using a pair of copper coils and a teslameter. The measurement is repeated for three different shielding orientations.

This shift is comparable in magnitude but opposite in sign to the shift due to Rb-Rb collisions (self-collision shift) found in Eq. (11.8).

11.2.3 Second-Order Doppler Shift

The second-order Doppler shift is obtained by evaluating Eq. (4.11) for 90°C cell temperature. Knowing that in a Maxwell-Boltzmann distribution, the mean square speed $\langle v^2 \rangle$ of a particle is equal to $3k_B T/m$ with k_B Boltzmann's constant, T being the temperature and m the particle mass, the relativistic shift is -223 Hz for the 90°C hot atomic vapor. The $\pm 3^\circ\text{C}$ uncertainty on cell temperature results in an uncertainty of ± 3.7 Hz.

11.2.4 Zeeman Effect

Magnetic Shielding Factor

The shielding factor of the single-layer mu-metal cage is measured by applying an external field created by an electrical current flowing through two copper coils. A magnetic flux density of around 16 Gauss is measured between the coils. The magnetic flux density within the magnetic shielding is measured as illustrated in Figure 11.4. This is done for three orientations of the shielding. Since the mu-metal cage has multiple holes for the laser beam, light pipe and screws, its shielding factor depends strongly on the orientation with respect to the magnetic field lines. The Earth magnetic field is assumed to follow perfectly the North-South axis (Neuchâtel: $47^\circ 00' \text{ N}$). In the setup, the vapor cell is inclined by 32° with respect to this axis. Therefore, a weighted shielding factor is calculated that accounts for the projections of the magnetic flux on these two axes. This results in a compounded shielding factor of 41, meaning the stationary magnetic flux density experienced by the atoms in the vapor cell are reduced by 41 with respect to the Earth magnetic field.

Earth Magnetic Field

The estimation of the Earth magnetic field in Neuchâtel is based on two sources. On the one hand, global data acquired by ESA's Swarm satellites [35] is used. This data is recent and covers the entire Earth. On the other hand, data evaluated specifically for Switzerland is used [41]. This data has a high spatial resolution, but dates from the year 1979. As the Earth magnetic field changes over time, the expressiveness of this data is considered equally high as the one from satellite measurements.

The ESA and the Swiss data support an Earth magnetic field of $37 \mu\text{T}$ and $47 \mu\text{T}$, respectively. Therefore, the Earth magnetic field in Neuchâtel is estimated to $42(\pm 5) \mu\text{T}$.

Calculated Zeeman Shift

The total systematic shift due to the Zeeman effect is calculated to

$$\Delta_f^{Zeeman} = +2.7(\pm 0.6) \text{ Hz} \quad (11.27)$$

using the two-photon magnetic sensitivity coefficient in Eq. (4.12), the compounded shielding factor of 41, and the estimation of the Earth magnetic field in Neuchâtel.

11.2.5 Black Body Radiation Shift

The atomic population is immersed in the black body radiation of the mechanical assembly holding and heating the vapor cell. The same 90°C temperature is assumed as for the vapor cell. At 90°C , the black body radiation shifts of -210 Hz and -195 Hz were reported by [51] and [75], respectively. This leads to a frequency shift of

$$\Delta_f^{BB} = -203(\pm 7) \text{ Hz} \quad (11.28)$$

when the two reported values are weighted equally.

11.2.6 Gravitational Red Shift

The optical frequency standard is operated in Neuchâtel at 487 meters altitude. Compared to an observation made at sea level, its frequency is thus blue-shifted. The gravitational red shift is expected to account for

$$\Delta_f^{gravit} = +20.6 \text{ Hz} \quad (11.29)$$

based on the coefficient given in 4.5.7.

11.3 Accuracy Budget

The different frequency shifts and uncertainties estimated above are summarized in Table 11.4. The very small effect due to line pulling (see 4.5.6) is neglected.

Effect	Evaluation	Value [Hz]	Uncert. [Hz]
Self-Collision Shift	measurement	-1 770	±350
Helium Collision	meas./calc.	+1 880	±500
Second-Order Doppler	calculation [23]	-223	±3.7
Zeeman	measurement	+2.7	±0.6
Black Body Radiation	calculation [51, 76]	-203	±7
Gravitational Red Shift	calculation [78]	+20.6	-
Subtotal		-293	± 610
Electronic Shifts	estimation [83]		± 3 850
Measurement Chain			± 270
Total		-292.7	± 3 907

Table 11.4: Accuracy budget listing the above-mentioned frequency shifts summing up to the difference between clock and atomic resonance frequency.

In fractional terms the resulting systematic resonance frequency shift is estimated to less than 10^{-12} . In addition to the uncertainty of the systematic frequency shifts, a fractional 10^{-11} uncertainty is added. The latter accounts for electronic shifts that possibly induce lock-point errors. The same uncertainty range as the one assumed by [84] is taken. Although this factor dominates total measurement uncertainty, it does not affect the magnitude of the systematic frequency shifts.

11.3.1 Correction of Measured Clock Frequency

The clock laser frequency f_{CW} is measured as outlined in Table 11.3. The clock frequency $2 \cdot f_{CW}$ is corrected by the systematic shifts given in Table 11.4. With this correction, the unperturbed atomic resonance frequency is measured to the value reported in Table 11.5.

	Frequency [Hz]
Clock frequency	385 284 566 371 858
Correction (atomic & relativistic)	-293(±610)
Resonance frequency	385 284 566 372 151
Resonance frequency uncertainty	±3 907

Table 11.5: Clock frequency and correction applied in order to determine the atomic resonance frequency.

11.3.2 Estimation of Residual Light Shift

As outlined above, no arithmetic correction is applied for the light shift since it is physically compensated by the mitigation laser. Nevertheless, an estimation of the magnitude of the compensated AC Stark shift is made.

The resonance frequency shift due to the interrogation laser is estimated by extrapolating interrogation power to zero. This leads to an estimated shift of -1317Hz . According to the comparison of two consecutive measurements with and without the mitigation laser, it causes a clock frequency shift of $+1353\text{Hz}$. These values support a light shift extinction of 15.7dB . The absolute frequency shift contribution of the residual light shift is thus expected to be larger than the Zeeman shift, but much smaller than the self-collision, helium collision, black body radiation and second-order Doppler shifts.

11.4 Comparison to Previously Reported Measurements

The measured unperturbed resonance frequency is compared to values previously reported for the $^{87}\text{Rb } 5S_{1/2} \rightarrow 5D_{5/2}$ two-photon transition ($F_g=2$) \rightarrow ($F_e=4$) hyperfine component. Figure 11.5 shows all the other absolute frequency measurements of this transition that have been reported to the best of my knowledge [13, 36, 51, 83, 85, 119]. All of these measurements were corrected for the AC Stark shift. The measurement presented here agrees well with the previously reported unperturbed resonance frequencies. Besides the arithmetically corrected resonance frequencies, also the AC-Stark-shift-uncorrected values are plotted in Figure 11.5. Moreover, the AC Stark shift magnitudes reported for previously reported measurements are given numerically in Table 11.6.

Publication	Year	Shift (Hz)	Uncertainty (Hz)
Nez et al. [85]	1993	-2000	-
Hilico et al. [51]	1998	-5300	< 140
Bernard et al. [13]	2000	-2812	20
		-2960	30
Edwards et al. [36]	2005	-13430	408
		-6579	442
Zhang et al. [119]	2015	-43200	3000
Newman et al. [83]	2019	-23500	3
(This work)	2025	(-1317)	(475)

Table 11.6: AC Stark shift magnitudes and uncertainties of rubidium two-photon clocks and frequency standards that have been used to correct previously reported absolute frequency measurements of the $^{87}\text{Rb } 5S_{1/2} \rightarrow 5D_{5/2}$ two-photon transition ($F_g=2$) \rightarrow ($F_e=4$) hyperfine component. The two publications for which two different values are listed each report on two separate two-photon systems.

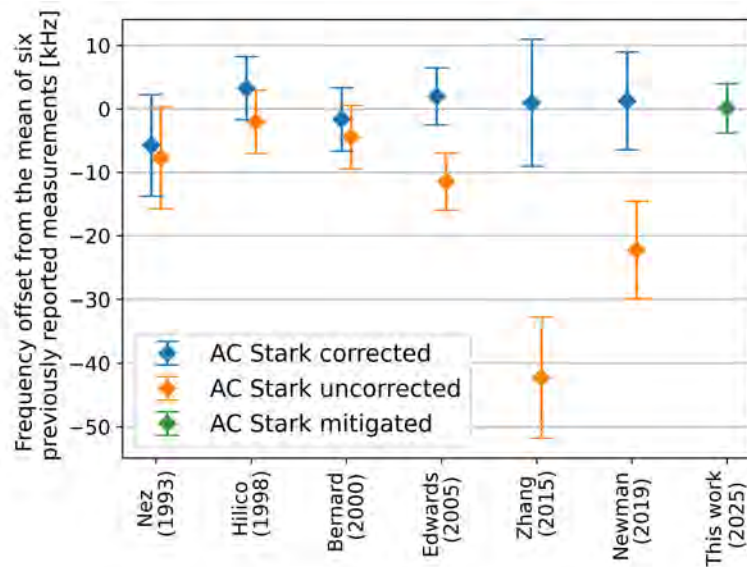


Figure 11.5: Comparison of absolute frequency measurements of the $^{87}\text{Rb } 5S_{1/2} \rightarrow 5D_{5/2}$ two-photon transition ($F_g = 2$) \rightarrow ($F_e = 4$) hyperfine component. The measurement reported here features AC Stark shift compensation with the 1556.2 nm wavelength mitigation laser. Therefore, no arithmetic correction for the light shift needs to be applied.

11.5 Retrace Measurement

According to the definition by [109], *retrace* designates the change of frequency after on/off operation and a specified warm-up time. Moreover, the operating conditions must not be changed after restart. Retrace is of interest for describing the repeatability of a frequency standard, in particular for portable devices.

A retrace measurement is made for the optical standard operated with the mitigation laser in place. The system is powered off for a period of 24 hours. After these 24 hours, a 5 hour warm-up period is initiated. At the beginning of this 5 hour period, the active control of the breadboard temperature to a 30° C setpoint is resumed. Moreover, the vapor cell and the frequency-doubler module are heated up once again and regulated to their respective setpoints. Finally, after the warm-up period, the frequency standard is re-locked manually. Five hours and seventeen minutes after the start of the warm-up period, the phase measurement is resumed. Figure 11.6 presents the optical frequency traces of the ten hours preceding the off-state period and the ten hours following restart.

After warm-up and restart, the clock frequency is offset by 76 Hz. Note that the standard deviation given in brackets is a consequence of the chosen sampling rate (1 Hz) and represents thus an upper bound for uncertainty. As frequency instability is lower at longer integration times, the actual uncertainty is smaller. In fractional frequency, the offset is $\Delta y \approx 2 \times 10^{-13}$. The retrace is thus lower than the uncertainty of the compounded systematic frequency shifts.

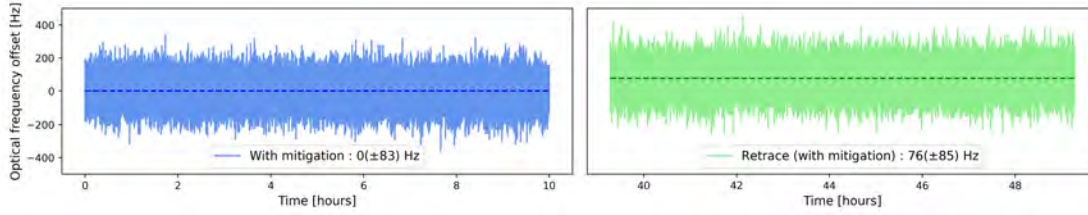


Figure 11.6: Retrace measurement for the frequency standard with mitigation laser. The frequency standard is switched off after a first measurement (left) and turned on again after 24 hours for a second measurement (right). The standard deviation of optical frequency is given in brackets (1 Hz sampling frequency).

11.6 Chapter Conclusions

An absolute frequency measurement of the ^{87}Rb $5S_{1/2} \rightarrow 5D_{5/2}$ two-photon transition ($F_g = 2$) \rightarrow ($F_e = 4$) hyperfine component was presented. Its result is in line with previously reported values for the same transition. But unlike in previous measurements, the AC Stark shift is corrected with a mitigation laser rather than by an arithmetic correction.

The AC Stark shift is ruled out as major contributor to systematic resonance frequency shifts. Instead, the helium collision and the self-collision shift dominate. The self-collision shift is intrinsic but poses only little challenge regarding repeatability. As cell temperature and thus rubidium vapor pressure can be controlled quite precisely, its stabilization to the same setpoint leads to negligible self-collision shift differences among different systems. The helium collision shift, in contrast, requires particular attention. A potential solution could consist in aluminosilicate glass [28] (ASG) vapor cells with or without additional Al_2O_3 coating [25].

Finally, a retrace measurement confirms the repeatability of the light shift mitigation with the 1556.2 nm wavelength laser. A fractional clock frequency offset of $\Delta y \approx 2 \times 10^{-13}$ was measured between two on-states separated by a 24-hour off-state and a 5-hour warm-up period.

Conclusion **Part IV**

12 Summary of Thesis

12.1 Rubidium Two-Photon Clock

A rubidium two-photon optical frequency standard featuring a light shift mitigation scheme based on a 1556.2 nm wavelength beam was designed, built and tested. It was operated with a short-term fractional frequency instability of $3 \times 10^{-13}/\sqrt{\tau}$ and achieved instabilities of a few 10^{-15} at $\tau = 10^4$ s.

The 1556.2 nm mitigation beam is frequency-locked to the 778.1 nm wavelength interrogation beam via second harmonic generation. The two beams are combined in free space. The AC Stark shift sensitivity coefficient at 1556.2 nm wavelength was measured and found to be in good agreement with the theoretical prediction reported by [75]. The same observation was made for the 778.1 nm interrogation wavelength. The beam intensities were then adjusted to the absolute value ratio of their sensitivity coefficients. In this setting, the optical power was attenuated without significantly affecting clock frequency, providing a proof of concept for this mitigation method.

Optical power was then stabilized in a configuration that relies on a common voltage reference for both beams. This architecture reduces the dependence of the clock frequency on the interrogation beam intensity. The voltage reference was then perturbed with a slow sinusoidal modulation in order to simulate a drift. The mitigation scheme reduces the impact of this perturbation on clock frequency by over an order of magnitude. In addition, the temperature sensitivity of the electronic circuits stabilizing optical power was characterized. Their temperature sensitivity was found not to constitute a relevant technical limit of the mitigation method. The overall temperature sensitivity of the power stabilization electronics is dominated by the temperature sensitivity of the silicon photodiode, which measures the interrogation beam power, rather than by the one of the InGaAs photodiode, which measures the mitigation beam power.

Finally, the absolute frequency of the two-photon transition was measured. Different systematic frequency shifts were accounted for by calculation and an accuracy budget was

established. As the light shift is compensated by the mitigation beam, it was not included in the accuracy budget. Nevertheless, the measured resonance frequency was found to agree well with previously reported measurements. With the addition of the mitigation laser, the systematic frequency shift due to the AC Stark effect was canceled, making collision shifts the largest systematic atomic resonance frequency shifts. A retrace measurement demonstrated the high repeatability of the method.

12.2 Optical Fiber Link

A fiber link for stable optical frequency transfer of a primary and a secondary signal was realized. Two optical signals with different wavelengths were combined using either polarization or wavelength-division multiplexing. While the fiber noise was actively compensated for the primary signal using Doppler cancellation, the transfer of the secondary signal was shown to benefit from indirect stabilization. In comparison to a situation without fiber noise cancellation, its transfer stability at 1000 seconds integration time was increased by a factor of 11.5 dB up to 16 dB depending on the multiplexing method that was used.

Theoretical considerations showed that a limitation of the method is given by the relative wavelength difference between the two signals. The noise compensation limit observed in experiment, however, was found to be set by the non-common fiber parts, which account for around five percent of the total link. Finally, it was concluded that the explored method can provide a simple means to stabilize the transfer of multiple optical frequencies at once. In particular, it has the advantages that the secondary signal is entirely subsidiary and that it requires no optical frequency comb.

13 Outlook and Concluding Thoughts

13.1 Rubidium Two-Photon Clock

Key advantages of the explored method include improved frequency accuracy, reduced sensitivity to voltage reference drifts and the property that the clock frequency is essentially independent of optical power. Nevertheless, as long as the frequency stability of an unperturbed system is not shown to be improved with the method, a compelling use case beyond scientific research remains to be identified. For applications in timekeeping, the demonstrated advantages currently do not weigh up for the increased footprint, complexity and power consumption. More importantly, however, the explored scheme breaks new ground for realizing technically more complex schemes featuring a mitigation laser. Based on the knowings acquired for 1556.2 nm wavelength, mitigation laser architectures are a promising path for sustained research efforts. At the same time, frequency stability limitations set by other technical noise sources must be examined.

Future research should focus on mitigation wavelengths closer to the one of the interrogation laser. This would allow to easily multiplex both wavelengths into the same fiber and launch them into free space using the same collimator, which would considerably reduce the footprint of the free-space optics.

On the one hand, relative intensity stabilization with a static beam power for each wavelength would presumably require the mitigation wavelength to be stabilized. Whereas this would be cumbersome in an optical frequency standard like the one explored here, in a full atomic clock, a laser with 785 nm wavelength could be locked to a mode of the frequency comb. An expected challenge would be to always lock it to the same comb mode when the system is rebooted.

On the other hand, intensity modulation could avoid the need to stabilize the mitigation wavelength. Instead, the overall light shift would be detected via the atomic response to common modulation of both beams. Close attention would need to be paid to the differences of modulation amplitude between the two wavelengths. If the individual modulation depths

drift over time, the point of zero light shift would be detected with a variable bias, jeopardizing the long-term repeatability of the method.

Even though a mitigation wavelength closer to 778.1 nm is assessed most promising, the use of a 1556.2 nm mitigation beam should not be excluded. A different architecture could avoid the dichroic combination of the interrogation and mitigation wavelengths in free space. More specifically, a 1556.2 nm free-space beam could be frequency-doubled with a PPLN crystal right in front of the atomic vapor cell. Two diverging beams would result from this configuration: a residual fundamental 1556.2 nm and a second-harmonic 778.1 nm beam. Using a sufficiently short microfabricated vapor cell, also a diverging interrogation beam could provide sufficient intensity to excite the two-photon transition. Such an architecture would work best with direct comb interrogation since a pulsed rather than a CW laser would increase the conversion efficiency of the PPLN crystal.

Further research on mitigation beams should complement sustained efforts on combined-error-signal-based approaches. If multiple alternative solutions can be found, this would allow to implement different techniques best suited to specific applications in view of their accuracy, stability and SWaP requirements. With the high diversity of rubidium two-photon realizations, it is unlikely that one technical solution can be found that is best suited to the whole range of possible systems and applications.

In a broader perspective, the rubidium two-photon clock has good prospects of becoming a technology of choice for demanding applications in time-keeping. In particular, compact two-photon clocks are ready for applications outside the laboratory environment. Besides the light shift, however, other technical challenges remain. Above all, these consist in understanding and mastering side effects of phase modulation and the permeation of impurities into the atomic vapor cell. If these challenges are solved, sustained and skilled engineering can enable the rubidium two-photon clock to outperform the active hydrogen maser in terms of frequency stability, accuracy, SWaP as well as cost of production and maintenance.

13.2 Optical Fiber Link

Although active noise compensation was shown to be nonessential for characterizing the rubidium two-photon optical frequency standard, fiber noise can indeed impede the frequency comparison of rubidium two-photon optical standards when they are separated by a distance in the kilometer range. Stabilization of fiber links used for on-campus applications, which is already required for optical lattice clocks, is likely to be soon needed for compact vapor-cell optical frequency standards. The presented method of dual optical frequency transfer can thereby help to streamline the simultaneous distribution of multiple optical frequencies.

In addition, the same concept could possibly be adapted to free-space optical links. Depending on the targeted use case, it could be implemented in a system relying on CW lasers. A method adapted to free space without the need for an optical frequency comb could provide a

robust and cost-effective solution for the simultaneous transfer of multiple optical frequencies through the atmosphere.

Finally, in the context of time transfer, an adaptation of the method could improve the stability of protocols that do not feature optical phase-locked loops. For instance, the White Rabbit protocol could benefit from a third wavelength channel without data traffic over which a CW laser is transmitted and optically phase-locked between network nodes. The optical phase lock would allow to sense round-trip delay variations caused by the fiber link and separate them from electronic delay contributions by the White Rabbit network switches. Such a hybrid scheme could combine the adaptability of a digital protocol with the high sensitivity of optical phase detection while staying cost-effective and readily deployable.

Geng we myni Uhr blybt stah
Mahnts mi dra das i se ja
Ganz alei erfunde ha
Und de dünkts mi i syg glych
Nid son e tumme Ma
— Mani Matter

Bibliography

- [1] M. Abdel Hafiz et al. “Protocol for Light-Shift Compensation in a Continuous-Wave Microcell Atomic Clock”. In: *Physical Review Applied* 14.3 (Sept. 8, 2020), p. 034015. ISSN: 2331-7019. DOI: 10.1103/PhysRevApplied.14.034015. URL: <https://link.aps.org/doi/10.1103/PhysRevApplied.14.034015> (visited on 08/05/2021).
- [2] E. Ahern et al. *Demonstration of a Mobile Optical Clock Ensemble at Sea*. Number: arXiv:2406.03716. June 21, 2024. arXiv: 2406.03716[physics]. URL: <http://arxiv.org/abs/2406.03716> (visited on 07/29/2024).
- [3] Emily J. Ahern et al. *Tailoring the Stability of a Two-Color, Two-Photon Rubidium Frequency Standard*. Number: arXiv:2410.16654. Oct. 22, 2024. arXiv: 2410.16654[physics]. URL: <http://arxiv.org/abs/2410.16654> (visited on 11/05/2024).
- [4] C. B. Alcock, V. P. Itkin, and M. K. Horrigan. “Vapour Pressure Equations for the Metallic Elements: 298–2500K”. In: *Canadian Metallurgical Quarterly* 23.3 (July 1984), pp. 309–313. ISSN: 0008-4433, 1879-1395. DOI: 10.1179/cmq.1984.23.3.309. URL: <http://www.tandfonline.com/doi/full/10.1179/cmq.1984.23.3.309> (visited on 01/31/2025).
- [5] D.W. Allan. “Statistics of atomic frequency standards”. In: *Proceedings of the IEEE* 54.2 (1966), pp. 221–230. ISSN: 0018-9219. DOI: 10.1109/PROC.1966.4634. URL: <http://ieeexplore.ieee.org/document/1446564/> (visited on 01/06/2025).
- [6] Yorick Andeweg, John Kitching, and Matthew Hummon. “Suppression of the AC Stark Shift in a Two-Photon Rubidium Optical Frequency Standard”. In: *IEEE IFCS-EFTF 2023 Conference Proceedings*. IEEE IFCS-EFTF 2023. Toyama, Japan. URL: <https://www.eftf.org/previous-meetings/>.
- [7] C. Audoin, V. Candelier, and N. Dimarcq. “A limit to the frequency stability of passive frequency standards due to an intermodulation effect”. In: *IEEE Transactions on Instrumentation and Measurement* 40.2 (Apr. 1991), pp. 121–125. ISSN: 0018-9456, 1557-9662. DOI: 10.1109/TIM.1990.1032896. URL: <http://ieeexplore.ieee.org/document/1032896/> (visited on 08/05/2021).

Bibliography

- [8] Parinaz Barakhshan et al. Published: *Portal for High-Precision Atomic Data and Computation* (version 2.0). University of Delaware, Newark, DE, USA. URL: <https://www.udel.edu/atom>.
- [9] Matteo Barbiero et al. “Optically Loaded Strontium Lattice Clock With a Single Multi-Wavelength Reference Cavity”. In: *IEEE Transactions on Instrumentation and Measurement* 71 (2022), pp. 1–9. ISSN: 0018-9456, 1557-9662. DOI: 10.1109/TIM.2022.3165292. URL: <https://ieeexplore.ieee.org/document/9750126/> (visited on 01/15/2025).
- [10] Etienne Batori et al. “GNSS-grade space atomic frequency standards: Current status and ongoing developments”. In: *Advances in Space Research* (Sept. 2020), S0273117720306414. ISSN: 02731177. DOI: 10.1016/j.asr.2020.09.012. URL: <https://linkinghub.elsevier.com/retrieve/pii/S0273117720306414> (visited on 09/01/2021).
- [11] River Beard et al. “Two-photon rubidium clock detecting 776 nm fluorescence”. In: *Optics Express* 32.5 (Feb. 26, 2024), p. 7417. ISSN: 1094-4087. DOI: 10.1364/OE.513974. URL: <https://opg.optica.org/abstract.cfm?URI=oe-32-5-7417> (visited on 02/16/2024).
- [12] Anthony Bercy et al. “Two-way optical frequency comparisons at 5×10^{-21} relative stability over 100-km telecommunication network fibers”. In: *Physical Review A* 90.6 (Dec. 22, 2014), p. 061802. ISSN: 1050-2947, 1094-1622. DOI: 10.1103/PhysRevA.90.061802. URL: <https://link.aps.org/doi/10.1103/PhysRevA.90.061802> (visited on 09/27/2023).
- [13] J.E. Bernard et al. “Absolute frequency measurement of a laser at 1556 nm locked to the 5S1/25D5/2 two-photon transition in 87Rb”. In: *Optics Communications* 173.1 (Jan. 2000), pp. 357–364. ISSN: 00304018. DOI: 10.1016/S0030-4018(99)00689-6. URL: <https://linkinghub.elsevier.com/retrieve/pii/S0030401899006896> (visited on 01/31/2025).
- [14] BIPM. *SI Brochure: The International System of Units (SI)*. URL: <https://www.bipm.org/en/publications/si-brochure>.
- [15] F. Biraben, M. Bassini, and B. Cagnac. “Line-shapes in Doppler-free two-photon spectroscopy. The effect of finite transit time”. In: *Journal de Physique* 40.5 (1979), pp. 445–455. ISSN: 0302-0738. DOI: 10.1051/jphys:01979004005044500. URL: <http://www.edpsciences.org/10.1051/jphys:01979004005044500> (visited on 11/22/2021).
- [16] F. Biraben, B. Cagnac, and G. Grynberg. “Experimental Evidence of Two-Photon Transition without Doppler Broadening”. In: *Physical Review Letters* 32.12 (Mar. 25, 1974), pp. 643–645. ISSN: 0031-9007. DOI: 10.1103/PhysRevLett.32.643. URL: <https://link.aps.org/doi/10.1103/PhysRevLett.32.643> (visited on 11/04/2021).
- [17] Roman Blum et al. “Dual optical frequency transfer through wavelength-division and polarization multiplexing in a 184-meter fiber link”. In: *Optics Continuum* (June 10, 2024). ISSN: 2770-0208. DOI: 10.1364/OPTCON.516673. URL: <https://opg.optica.org/optcon/abstract.cfm?doi=10.1364/OPTCON.516673> (visited on 07/01/2024).

- [18] Paul T Boggs and Janet R Donaldson. *Orthogonal distance regression*. NIST IR 89-4197. Gaithersburg, MD: National Institute of Standards and Technology, 1989, NIST IR 89-4197. DOI: 10.6028/NIST.IR.89-4197. URL: <https://nvlpubs.nist.gov/nistpubs/Legacy/IR/nistir89-4197.pdf> (visited on 01/10/2025).
- [19] Tobias Bothwell et al. "JILA SrI optical lattice clock with uncertainty of 2.0×10^{-18} ". In: *Metrologia* 56.6 (Dec. 1, 2019), p. 065004. ISSN: 0026-1394, 1681-7575. DOI: 10.1088/1681-7575/ab4089. URL: <https://iopscience.iop.org/article/10.1088/1681-7575/ab4089> (visited on 01/15/2025).
- [20] A. Bregazzi et al. "A cold-atom Ramsey clock with a low volume physics package". In: *Scientific Reports* 14.1 (Jan. 9, 2024), p. 931. ISSN: 2045-2322. DOI: 10.1038/s41598-024-51418-8. URL: <https://www.nature.com/articles/s41598-024-51418-8> (visited on 02/12/2025).
- [21] S. M. Brewer et al. " $^{27}\text{Al}^+$ Quantum-Logic Clock with a Systematic Uncertainty below 10^{-18} ". In: *Phys. Rev. Lett.* 123.3 (July 2019). Publisher: American Physical Society, p. 033201. DOI: 10.1103/PhysRevLett.123.033201. URL: <https://link.aps.org/doi/10.1103/PhysRevLett.123.033201>.
- [22] E. A. Burt et al. "Demonstration of a trapped-ion atomic clock in space". In: *Nature* 595.7865 (July 1, 2021), pp. 43–47. ISSN: 0028-0836, 1476-4687. DOI: 10.1038/s41586-021-03571-7. URL: <http://www.nature.com/articles/s41586-021-03571-7> (visited on 01/03/2022).
- [23] B. Cagnac, G. Grynberg, and F. Biraben. "Spectroscopie d'absorption multiphotonique sans effet Doppler". In: *Journal de Physique* 34.10 (1973), pp. 845–858. ISSN: 0302-0738. DOI: 10.1051/jphys:019730034010084500. URL: <http://www.edpsciences.org/10.1051/jphys:019730034010084500> (visited on 09/01/2021).
- [24] Martin Callejo et al. "Short-term stability of a microcell optical reference based on the Rb atom two-photon transition at 778 nm". In: *Journal of the Optical Society of America B* 42.1 (Jan. 1, 2025), p. 151. ISSN: 0740-3224, 1520-8540. DOI: 10.1364/JOSAB.533904. URL: <https://opg.optica.org/abstract.cfm?URI=josab-42-1-151> (visited on 12/29/2024).
- [25] C. Carlé et al. "Reduction of helium permeation in microfabricated cells using aluminosilicate glass substrates and Al_2O_3 coatings". In: *Journal of Applied Physics* 133.21 (June 2023). _eprint: https://pubs.aip.org/aip/jap/article-pdf/doi/10.1063/5.0151899/17922422/214501_1_5.0151899.pdf. ISSN: 0021-8979. DOI: 10.1063/5.0151899. URL: <https://doi.org/10.1063/5.0151899>.
- [26] C. Clivati et al. "Coherent Optical-Fiber Link Across Italy and France". In: *Physical Review Applied* 18.5 (Nov. 3, 2022), p. 054009. ISSN: 2331-7019. DOI: 10.1103/PhysRevApplied.18.054009. URL: <https://link.aps.org/doi/10.1103/PhysRevApplied.18.054009> (visited on 05/30/2023).
- [27] *Corning SMF28e+® Photonic Specialty Fiber.pdf*. URL: <https://www.corning.com/media/worldwide/csm/documents/Corning%20SMF28e%20%2B%20C2%20AE%20Photonic%20Specialty%20Fiber.pdf> (visited on 10/25/2023).

Bibliography

- [28] Argyrios T. Dellis et al. “Low helium permeation cells for atomic microsystems technology”. In: *Opt. Lett.* 41.12 (June 2016). Publisher: OSA, pp. 2775–2778. DOI: 10.1364/OL.41.002775. URL: <http://opg.optica.org/ol/abstract.cfm?URI=ol-41-12-2775>.
- [29] Siminda Deng et al. “Cold atom microwave clock based on intracavity cooling in China space station”. In: *npj Microgravity* 10.1 (June 6, 2024), p. 66. ISSN: 2373-8065. DOI: 10.1038/s41526-024-00407-2. URL: <https://www.nature.com/articles/s41526-024-00407-2> (visited on 02/12/2025).
- [30] Scott A. Diddams, Kerry Vahala, and Thomas Udem. “Optical frequency combs: Coherently uniting the electromagnetic spectrum”. In: *Science* 369.6501 (July 17, 2020), eaay3676. ISSN: 0036-8075, 1095-9203. DOI: 10.1126/science.aay3676. URL: <https://www.science.org/doi/10.1126/science.aay3676> (visited on 01/21/2025).
- [31] Klaus Döringshoff et al. “Iodine Frequency Reference on a Sounding Rocket”. In: *Phys. Rev. Applied* 11.5 (May 2019). Publisher: American Physical Society, p. 054068. DOI: 10.1103/PhysRevApplied.11.054068. URL: <https://link.aps.org/doi/10.1103/PhysRevApplied.11.054068>.
- [32] Stefan Droste et al. “An Acetylene-based Optical Clock with $< 3 \times 10^{-13}$ Fractional Frequency Instability”. In: (2024). URL: <https://ieeexplore.ieee.org/document/10728223>.
- [33] F. Droz et al. “On-board Galileo RAFS, current status and performances”. In: *IEEE International Frequency Control Symposium and PDA Exhibition Jointly with the 17th European Frequency and Time Forum, 2003. Proceedings of the 2003. IEEE International Frequency Control Symposium and PDA Exhibition Jointly with the 17th European Frequency and Time Forum, 2003.* 2003. Tampa, FL, USA: IEEE, 2003, pp. 105–108. ISBN: 978-0-7803-7688-5. DOI: 10.1109/FREQ.2003.1274996. URL: <http://ieeexplore.ieee.org/document/1274996/> (visited on 01/29/2025).
- [34] Fabien Droz et al. “GNSS RAFS latest improvements”. In: *2015 Joint Conference of the IEEE International Frequency Control Symposium & the European Frequency and Time Forum.* 2015 Joint Conference of the IEEE International Frequency Control Symposium & the European Frequency and Time Forum (FCS). Denver, CO, USA: IEEE, Apr. 2015, pp. 637–642. ISBN: 978-1-4799-8866-2. DOI: 10.1109/FCS.2015.7138926. URL: <http://ieeexplore.ieee.org/document/7138926/> (visited on 01/29/2025).
- [35] *Earth’s magnetic field.* In collab. with European Space Agency (ESA). 2024. URL: <https://visuals.earth.esa.int/data/magnetic-field>.
- [36] C S Edwards et al. “Development and absolute frequency measurement of a pair of 778 nm two-photon rubidium standards”. In: *Metrologia* 42.5 (Oct. 2005), pp. 464–467. ISSN: 0026-1394, 1681-7575. DOI: 10.1088/0026-1394/42/5/018. URL: <https://iopscience.iop.org/article/10.1088/0026-1394/42/5/018> (visited on 08/05/2021).

- [37] Seth Erickson et al. “Optical Atomic Clock Based on Direct Comb Spectroscopy”. In: *Optics Letters* (Aug. 8, 2024). Publisher: Optica Publishing Group. ISSN: 0146-9592, 1539-4794. DOI: 10.1364/ol.531600. URL: <https://opg.optica.org/ol/abstract.cfm?doi=10.1364/OL.531600> (visited on 09/17/2024).
- [38] Seth E. Erickson. *An Optical Atomic Clock based on Frequency Comb Spectroscopy*. 2024. URL: <http://hdl.handle.net/10150/671250>.
- [39] Fang Fang et al. “NIM5 Cs fountain clock and its evaluation”. In: *Metrologia* 52.4 (Aug. 1, 2015), pp. 454–468. ISSN: 0026-1394, 1681-7575. DOI: 10.1088/0026-1394/52/4/454. URL: <https://iopscience.iop.org/article/10.1088/0026-1394/52/4/454> (visited on 01/15/2025).
- [40] Xin Feng et al. “Determination of the coefficient of thermal expansion with embedded long-gauge fiber optic sensors”. In: *Measurement Science and Technology* 21.6 (June 1, 2010), p. 065302. ISSN: 0957-0233, 1361-6501. DOI: 10.1088/0957-0233/21/6/065302. URL: <https://iopscience.iop.org/article/10.1088/0957-0233/21/6/065302> (visited on 06/05/2024).
- [41] G. Fischer and P.-A. Schnegg. *Total Intensity Map of Switzerland 1:500000*. 1979. URL: <https://www.geocat.ch/geonetwork/srv/eng/catalog.search#/metadata/132d9ff6-92de-4c02-87a7-72df26bcb33e>.
- [42] V. Gerginov and K. Beloy. “Two-photon Optical Frequency Reference with Active ac Stark Shift Cancellation”. In: *Physical Review Applied* 10.1 (July 30, 2018), p. 014031. ISSN: 2331-7019. DOI: 10.1103/PhysRevApplied.10.014031. URL: <https://link.aps.org/doi/10.1103/PhysRevApplied.10.014031> (visited on 08/05/2021).
- [43] Irene Goti et al. “Absolute frequency measurement of a Yb optical clock at the limit of the Cs fountain”. In: *Metrologia* 60.3 (June 1, 2023), p. 035002. ISSN: 0026-1394, 1681-7575. DOI: 10.1088/1681-7575/acbc5. URL: <https://iopscience.iop.org/article/10.1088/1681-7575/acbc5> (visited on 01/15/2025).
- [44] Michele Gozzelino et al. “Realization of a pulsed optically pumped Rb clock with a frequency stability below 10^{-15} ”. In: *Scientific Reports* 13.1 (Aug. 10, 2023), p. 12974. ISSN: 2045-2322. DOI: 10.1038/s41598-023-39942-5. URL: <https://www.nature.com/articles/s41598-023-39942-5> (visited on 01/01/2025).
- [45] J Guéna et al. “Contributing to TAI with a secondary representation of the SI second”. In: *Metrologia* 51.1 (Feb. 1, 2014), pp. 108–120. ISSN: 0026-1394, 1681-7575. DOI: 10.1088/0026-1394/51/1/108. URL: <https://iopscience.iop.org/article/10.1088/0026-1394/51/1/108> (visited on 01/15/2025).
- [46] Jacques Haesler et al. “Development of a High-Performance and Swiss Based Rolex Timescale System Including a Unique Optical Atomic Clock”. In: *2024 European Frequency and Time Forum (EFTF)*. 2024 European Frequency and Time Forum (EFTF). Neuchâtel, Switzerland: IEEE, June 25, 2024, pp. 49–50. ISBN: 9798350354270. DOI: 10.1109/EFTF61992.2024.10722272. URL: <https://ieeexplore.ieee.org/document/10722272/> (visited on 01/09/2025).

Bibliography

- [47] Jacques Haesler et al. “Swiss miniature atomic clock: First prototype and preliminary results”. In: *2012 European Frequency and Time Forum*. 2012 European Frequency and Time Forum (EFTF). Gothenburg, Sweden: IEEE, Apr. 2012, pp. 312–315. ISBN: 978-1-4673-1923-2 978-1-4673-1924-9 978-1-4673-1922-5. DOI: 10.1109/EFTF.2012.6502390. URL: <http://ieeexplore.ieee.org/document/6502390/> (visited on 01/15/2025).
- [48] John L. Hall. “Nobel Lecture: Defining and measuring optical frequencies”. In: *Reviews of Modern Physics* 78.4 (Nov. 17, 2006), pp. 1279–1295. ISSN: 0034-6861, 1539-0756. DOI: 10.1103/RevModPhys.78.1279. URL: <https://link.aps.org/doi/10.1103/RevModPhys.78.1279> (visited on 01/21/2025).
- [49] Theodor W. Hänsch. “Nobel Lecture: Passion for precision”. In: *Reviews of Modern Physics* 78.4 (Nov. 17, 2006), pp. 1297–1309. ISSN: 0034-6861, 1539-0756. DOI: 10.1103/RevModPhys.78.1297. URL: <https://link.aps.org/doi/10.1103/RevModPhys.78.1297> (visited on 08/05/2021).
- [50] O. S. Heavens. “Radiative Transition Probabilities of the Lower Excited States of the Alkali Metals”. In: *Journal of the Optical Society of America* 51.10 (Oct. 1, 1961), p. 1058. ISSN: 0030-3941. DOI: 10.1364/JOSA.51.001058. URL: <https://www.osapublishing.org/abstract.cfm?URI=josa-51-10-1058> (visited on 11/11/2021).
- [51] L. Hilico et al. “Metrological features of the rubidium two-photon standards of the BNM-LPTF and Kastler Brossel Laboratories”. In: *The European Physical Journal Applied Physics* 4.2 (Nov. 1998), pp. 219–225. ISSN: 1286-0042, 1286-0050. DOI: 10.1051/epjap:1998263. URL: <http://www.epjap.org/10.1051/epjap:1998263> (visited on 08/05/2021).
- [52] Kevin W. Holman et al. “Remote transfer of a high-stability and ultralow-jitter timing signal”. In: *Optics Letters* 30.10 (May 15, 2005), p. 1225. ISSN: 0146-9592, 1539-4794. DOI: 10.1364/OL.30.001225. URL: <https://opg.optica.org/abstract.cfm?URI=ol-30-10-1225> (visited on 02/07/2024).
- [53] Yao Huang et al. “Geopotential measurement with a robust, transportable Ca + optical clock”. In: *Physical Review A* 102.5 (Nov. 18, 2020), p. 050802. ISSN: 2469-9926, 2469-9934. DOI: 10.1103/PhysRevA.102.050802. URL: <https://link.aps.org/doi/10.1103/PhysRevA.102.050802> (visited on 01/15/2025).
- [54] Bernardo Jadusziwer and James Camparo. “Past, present and future of atomic clocks for GNSS”. In: *GPS Solutions* 25.1 (Jan. 2021), p. 27. ISSN: 1080-5370, 1521-1886. DOI: 10.1007/s10291-020-01059-x. URL: <http://link.springer.com/10.1007/s10291-020-01059-x> (visited on 09/01/2021).
- [55] A Jallageas et al. “First uncertainty evaluation of the FoCS-2 primary frequency standard”. In: *Metrologia* 55.3 (June 1, 2018), pp. 366–385. ISSN: 0026-1394, 1681-7575. DOI: 10.1088/1681-7575/aab3fa. URL: <https://iopscience.iop.org/article/10.1088/1681-7575/aab3fa> (visited on 01/15/2025).

- [56] A Jallageas et al. “Status and prospect of the Swiss continuous Cs fountain FoCS-2”. In: *Journal of Physics: Conference Series* 723 (June 2016), p. 012010. ISSN: 1742-6588, 1742-6596. DOI: 10.1088/1742-6596/723/1/012010. URL: <https://iopscience.iop.org/article/10.1088/1742-6596/723/1/012010> (visited on 01/15/2025).
- [57] David J. Jones et al. “Carrier-Envelope Phase Control of Femtosecond Mode-Locked Lasers and Direct Optical Frequency Synthesis”. In: *Science* 288.5466 (Apr. 28, 2000), pp. 635–639. ISSN: 0036-8075, 1095-9203. DOI: 10.1126/science.288.5466.635. URL: <https://www.science.org/doi/10.1126/science.288.5466.635> (visited on 01/29/2025).
- [58] Cezary Kaczmarek. “Measurement of the Temperature Sensitivity of Modal Birefringence of Polarization Maintaining Fibers Using a Sagnac Interferometer”. In: *IEEE Sensors Journal* 16.10 (May 2016), pp. 3627–3632. ISSN: 1530-437X, 1558-1748, 2379-9153. DOI: 10.1109/JSEN.2016.2533320. URL: <http://ieeexplore.ieee.org/document/7421933/> (visited on 07/27/2023).
- [59] Koji Kawasaki and Kiyoshi Senzaki. “Permeation of Helium Gas through Glass”. In: *Japanese Journal of Applied Physics* 1.4 (Apr. 1962), pp. 223–226. ISSN: 0021-4922, 1347-4065. DOI: 10.1143/JJAP1.223. URL: <https://iopscience.iop.org/article/10.1143/JJAP1.223> (visited on 10/13/2021).
- [60] John Kitching. “Chip-scale atomic devices”. In: *Applied Physics Reviews* 5.3 (Sept. 2018), p. 031302. ISSN: 1931-9401. DOI: 10.1063/1.5026238. URL: <https://pubs.aip.org/aip/apr/article/123951> (visited on 01/15/2025).
- [61] Svenja Knappe et al. “A microfabricated atomic clock”. In: *Applied Physics Letters* 85.9 (Aug. 30, 2004), pp. 1460–1462. ISSN: 0003-6951, 1077-3118. DOI: 10.1063/1.1787942. URL: <http://aip.scitation.org/doi/10.1063/1.1787942> (visited on 08/05/2021).
- [62] S. B. Koller et al. “Transportable Optical Lattice Clock with 7×10^{-17} Uncertainty”. In: *Physical Review Letters* 118.7 (Feb. 13, 2017), p. 073601. ISSN: 0031-9007, 1079-7114. DOI: 10.1103/PhysRevLett.118.073601. URL: <https://link.aps.org/doi/10.1103/PhysRevLett.118.073601> (visited on 01/15/2025).
- [63] P. Kwee et al. “Stabilized high-power laser system for the gravitational wave detector advanced LIGO”. In: *Optics Express* 20.10 (May 7, 2012), p. 10617. ISSN: 1094-4087. DOI: 10.1364/OE.20.010617. URL: <https://www.osapublishing.org/oe/abstract.cfm?uri=oe-20-10-10617> (visited on 11/19/2021).
- [64] Patrick Kwee, Benno Willke, and Karsten Danzmann. “Laser power noise detection at the quantum-noise limit of 32 A photocurrent”. In: *Optics Letters* 36.18 (Sept. 15, 2011), p. 3563. ISSN: 0146-9592, 1539-4794. DOI: 10.1364/OL.36.003563. URL: <https://www.osapublishing.org/abstract.cfm?URI=ol-36-18-3563> (visited on 12/21/2021).
- [65] Nathan D. Lemke et al. “Measurement of Optical Rubidium Clock Frequency Spanning 65 Days”. In: *Sensors* 22.5 (Mar. 3, 2022), p. 1982. ISSN: 1424-8220. DOI: 10.3390/s22051982. URL: <https://www.mdpi.com/1424-8220/22/5/1982> (visited on 03/07/2022).

Bibliography

- [66] Dou Li et al. “A frequency shift compensation method for light shift and vapor-cell temperature shift in atomic clocks”. In: *arXiv.2405.14281* 2024 (). URL: <https://doi.org/10.48550/arXiv.2405.14281>.
- [67] Dou Li et al. “Dual-interrogation method for suppressing light shift in Rb 778 nm two-photon transition optical frequency standard”. In: *Optics Express* 32.2 (Jan. 15, 2024), p. 2766. ISSN: 1094-4087. DOI: 10.1364/OE.512205. URL: <https://opg.optica.org/abstract.cfm?URI=oe-32-2-2766> (visited on 01/15/2024).
- [68] P. F. Liao and J. E. Bjorkholm. “Direct Observation of Atomic Energy Level Shifts in Two-Photon Absorption”. In: *Physical Review Letters* 34.1 (Jan. 6, 1975), pp. 1–4. ISSN: 0031-9007. DOI: 10.1103/PhysRevLett.34.1. URL: <https://link.aps.org/doi/10.1103/PhysRevLett.34.1> (visited on 08/05/2021).
- [69] Michael Lombardi. “Fundamentals of Time and Frequency”. In: *Mechatronics*. Ed. by Robert Bishop. CRC Press, Sept. 13, 2005, pp. 10–1–10–18. ISBN: 978-0-8493-6358-0 978-1-4200-3724-1. DOI: 10.1201/9781420037241.ch10. URL: <http://www.crcnetbase.com/doi/10.1201/9781420037241.ch10> (visited on 01/06/2025).
- [70] Long-Sheng Ma et al. “Delivering the same optical frequency at two places: accurate cancellation of phase noise introduced by an optical fiber or other time-varying path”. In: *Optics Letters* 19.21 (Nov. 1, 1994), p. 1777. ISSN: 0146-9592, 1539-4794. DOI: 10.1364/OL.19.001777. URL: <https://opg.optica.org/abstract.cfm?URI=ol-19-21-1777> (visited on 09/26/2023).
- [71] Leo A. Mallette, Joe White, and Pascal Rochat. “Space qualified frequency sources (clocks) for current and future GNSS applications”. In: *IEEE/ION Position, Location and Navigation Symposium*. 2010 IEEE/ION Position, Location and Navigation Symposium - PLANS 2010. Indian Wells, CA, USA: IEEE, May 2010, pp. 903–908. ISBN: 978-1-4244-5036-7. DOI: 10.1109/PLANS.2010.5507225. URL: <http://ieeexplore.ieee.org/document/5507225/> (visited on 01/03/2022).
- [72] Bonnie L. Schmittberger Marlow and David R. Scherer. “A Review of Commercial and Emerging Atomic Frequency Standards”. In: *IEEE Transactions on Ultrasonics, Ferroelectrics, and Frequency Control* 68.6 (June 2021), pp. 2007–2022. ISSN: 0885-3010, 1525-8955. DOI: 10.1109/TUFFC.2021.3049713. URL: <https://ieeexplore.ieee.org/document/9316270/> (visited on 09/13/2022).
- [73] Giuseppe Marra, Helen S. Margolis, and David J. Richardson. “Dissemination of an optical frequency comb over fiber with 3×10^{-18} fractional accuracy”. In: *2012 Conference on Lasers and Electro-Optics (CLEO)*. ISSN: 2160-8989. May 2012, pp. 1–2. URL: <https://ieeexplore.ieee.org/abstract/document/6325922>.
- [74] Kyle W. Martin et al. “Compact Optical Atomic Clock Based on a Two-Photon Transition in Rubidium”. In: *Physical Review Applied* 9.1 (Jan. 18, 2018), p. 014019. ISSN: 2331-7019. DOI: 10.1103/PhysRevApplied.9.014019. URL: <https://link.aps.org/doi/10.1103/PhysRevApplied.9.014019> (visited on 11/14/2023).

- [75] Kyle W. Martin et al. “Frequency shifts due to Stark effects on a rubidium two-photon transition”. In: *Physical Review A* 100.2 (Aug. 28, 2019), p. 023417. ISSN: 2469-9926, 2469-9934. DOI: 10.1103/PhysRevA.100.023417. URL: <https://link.aps.org/doi/10.1103/PhysRevA.100.023417> (visited on 08/05/2021).
- [76] Kyle W. Martin et al. “The Optical Stark Shift on a Two-Photon Transition in Rubidium”. In: *2018 IEEE International Frequency Control Symposium (IFCS)*. 2018 IEEE International Frequency Control Symposium (IFCS). Olympic Valley, CA: IEEE, May 2018, pp. 1–2. ISBN: 978-1-5386-3214-7. DOI: 10.1109/IFCS.2018.8597481. URL: <https://ieeexplore.ieee.org/document/8597481/> (visited on 08/05/2021).
- [77] Vincent Maurice et al. “Miniaturized optical frequency reference for next-generation portable optical clocks”. In: *Optics Express* 28.17 (Aug. 17, 2020), p. 24708. ISSN: 1094-4087. DOI: 10.1364/OE.396296. URL: <https://www.osapublishing.org/abstract.cfm?URI=oe-28-17-24708> (visited on 10/06/2021).
- [78] W. F. McGrew et al. “Atomic clock performance enabling geodesy below the centimetre level”. In: *Nature* 564.7734 (Dec. 1, 2018), pp. 87–90. ISSN: 1476-4687. DOI: 10.1038/s41586-018-0738-2. URL: <https://doi.org/10.1038/s41586-018-0738-2>.
- [79] S. Micalizio et al. “A pulsed-Laser Rb atomic frequency standard for GNSS applications”. In: *GPS Solutions* 25.3 (Apr. 23, 2021), p. 94. ISSN: 1521-1886. DOI: 10.1007/s10291-021-01136-9. URL: <https://doi.org/10.1007/s10291-021-01136-9>.
- [80] Shambo Mukherjee et al. “Digital Doppler-Cancellation Servo for Ultrastable Optical Frequency Dissemination Over Fiber”. In: *IEEE Transactions on Ultrasonics, Ferroelectrics, and Frequency Control* 69.2 (Feb. 2022), pp. 878–885. ISSN: 0885-3010, 1525-8955. DOI: 10.1109/TUFFC.2021.3125066. URL: <https://ieeexplore.ieee.org/document/9599700/> (visited on 07/19/2023).
- [81] Stella Torres Müller et al. “Compact frequency standard based on an intracavity sample of cold cesium atoms”. In: *Journal of the Optical Society of America B* 28.11 (Nov. 1, 2011), p. 2592. ISSN: 0740-3224, 1520-8540. DOI: 10.1364/JOSAB.28.002592. URL: <https://opg.optica.org/abstract.cfm?URI=josab-28-11-2592> (visited on 02/15/2025).
- [82] N. R. Newbury, P. A. Williams, and W. C. Swann. “Coherent transfer of an optical carrier over 251 km”. In: *Optics Letters* 32.21 (Nov. 1, 2007), p. 3056. ISSN: 0146-9592, 1539-4794. DOI: 10.1364/OL.32.003056. URL: <https://opg.optica.org/abstract.cfm?URI=ol-32-21-3056> (visited on 09/26/2023).
- [83] Zachary L. Newman et al. “Architecture for the photonic integration of an optical atomic clock”. In: *Optica* 6.5 (May 20, 2019), p. 680. ISSN: 2334-2536. DOI: 10.1364/OPTICA.6.000680. URL: <https://www.osapublishing.org/abstract.cfm?URI=optica-6-5-680> (visited on 08/05/2021).
- [84] Zachary L. Newman et al. “High-performance, compact optical standard”. In: *Optics Letters* 46.18 (Sept. 15, 2021), p. 4702. ISSN: 0146-9592, 1539-4794. DOI: 10.1364/OL.435603. URL: <https://opg.optica.org/abstract.cfm?URI=ol-46-18-4702> (visited on 11/14/2023).

Bibliography

- [85] F. Nez et al. “Optical frequency determination of the hyperfine components of the $5S_{1/2}$ - $5D_{3/2}$ two-photon transitions in rubidium”. In: *Optics Communications* 102.5 (1993), pp. 432–438. ISSN: 0030-4018. DOI: [https://doi.org/10.1016/0030-4018\(93\)90417-4](https://doi.org/10.1016/0030-4018(93)90417-4). URL: <https://www.sciencedirect.com/science/article/pii/0030401893904174>.
- [86] Tin Nghia Nguyen and Thomas R. Schibli. “Temperature-shift-suppression scheme for two-photon two-color rubidium vapor clocks”. In: *Physical Review A* 106.5 (Nov. 3, 2022), p. 053104. ISSN: 2469-9926, 2469-9934. DOI: 10.1103/PhysRevA.106.053104. URL: <https://link.aps.org/doi/10.1103/PhysRevA.106.053104> (visited on 02/06/2023).
- [87] Katsunari Okamoto. “Chapter 3 - Optical fibers”. In: *Fundamentals of Optical Waveguides (Second Edition)*. Ed. by Katsunari Okamoto. Second Edition. Burlington: Academic Press, 2006, pp. 57–158. ISBN: 978-0-12-525096-2. DOI: <https://doi.org/10.1016/B978-012525096-2/50004-0>. URL: <https://www.sciencedirect.com/science/article/pii/B9780125250962500040>.
- [88] C. Perrella et al. “Dichroic Two-Photon Rubidium Frequency Standard”. In: *Physical Review Applied* 12.5 (Nov. 27, 2019), p. 054063. ISSN: 2331-7019. DOI: 10.1103/PhysRevApplied.12.054063. URL: <https://link.aps.org/doi/10.1103/PhysRevApplied.12.054063> (visited on 08/05/2021).
- [89] C. Perrella et al. “Two-color rubidium fiber frequency standard”. In: *Optics Letters* 38.12 (June 15, 2013), p. 2122. ISSN: 0146-9592, 1539-4794. DOI: 10.1364/OL.38.002122. URL: <https://www.osapublishing.org/abstract.cfm?URI=ol-38-12-2122> (visited on 08/05/2021).
- [90] Gretchen Phelps et al. “Compact Optical Clock with 5×10^{-13} Instability at 1 s”. In: *NAVIGATION* 65.1 (Mar. 2018), pp. 49–54. ISSN: 0028-1522, 2161-4296. DOI: 10.1002/navi.215. URL: <https://onlinelibrary.wiley.com/doi/10.1002/navi.215> (visited on 12/22/2023).
- [91] Gretchen Phelps et al. “Two-Photon Spectroscopy in Rb for an Optical Frequency Standard”. In: *Frontiers in Optics 2015. Laser Science*. San Jose, California: OSA, 2015, LTh4I.5. ISBN: 978-1-943580-03-3. DOI: 10.1364/LS.2015.LTh4I.5. URL: <https://www.osapublishing.org/abstract.cfm?URI=LS-2015-LTh4I.5> (visited on 08/05/2021).
- [92] N. Poli et al. “A transportable strontium optical lattice clock”. In: *Applied Physics B* 117.4 (Dec. 2014), pp. 1107–1116. ISSN: 0946-2171, 1432-0649. DOI: 10.1007/s00340-014-5932-9. URL: <http://link.springer.com/10.1007/s00340-014-5932-9> (visited on 01/15/2025).
- [93] Daryl W. Preston. “Doppler-free saturated absorption: Laser spectroscopy”. In: *American Journal of Physics* 64.11 (Nov. 1, 1996), pp. 1432–1436. ISSN: 0002-9505, 1943-2909. DOI: 10.1119/1.18457. URL: <https://pubs.aip.org/ajp/article/64/11/1432/1054770/Doppler-free-saturated-absorption-Laser> (visited on 01/30/2025).

- [94] Norman F. Ramsey. “A Molecular Beam Resonance Method with Separated Oscillating Fields”. In: *Physical Review* 78.6 (June 15, 1950), pp. 695–699. ISSN: 0031-899X. DOI: 10.1103/PhysRev.78.695. URL: <https://link.aps.org/doi/10.1103/PhysRev.78.695> (visited on 08/05/2021).
- [95] William Riley and David Howe. *Handbook of Frequency Stability Analysis*. July 1, 2008. URL: https://tsapps.nist.gov/publication/get_pdf.cfm?pub_id=50505.
- [96] W. A. Rogers, R. S. Buritz, and D. Alpert. “Diffusion Coefficient, Solubility, and Permeability for Helium in Glass”. In: *Journal of Applied Physics* 25.7 (July 1, 1954), pp. 868–875. ISSN: 0021-8979, 1089-7550. DOI: 10.1063/1.1721760. URL: <https://pubs.aip.org/jap/article/25/7/868/160802/Diffusion-Coefficient-Solubility-and-Permeability> (visited on 01/31/2025).
- [97] Jonathan D. Roslund et al. “Optical clocks at sea”. In: *Nature* 628.8009 (Apr. 25, 2024), pp. 736–740. ISSN: 0028-0836, 1476-4687. DOI: 10.1038/s41586-024-07225-2. URL: <https://www.nature.com/articles/s41586-024-07225-2> (visited on 07/29/2024).
- [98] Enrico Rubiola and Francois Vernotte. “The Companion of Enrico’s Chart for Phase Noise and Two-Sample Variances”. In: *IEEE Transactions on Microwave Theory and Techniques* 71.7 (July 2023), pp. 2996–3025. ISSN: 0018-9480, 1557-9670. DOI: 10.1109/TMTT.2023.3238267. arXiv: 2201.07109[physics, physics:quant-ph]. URL: <http://arxiv.org/abs/2201.07109> (visited on 11/15/2023).
- [99] Thibaud Ruelle et al. “Development of an Industrial Two-Photon Rb Atomic Clock for Timekeeping Applications”. In: *2024 European Frequency and Time Forum (EFTF)*. 2024 European Frequency and Time Forum (EFTF). Neuchâtel, Switzerland: IEEE, June 25, 2024, pp. 1–2. ISBN: 9798350354270. DOI: 10.1109/EFTF61992.2024.10722354. URL: <https://ieeexplore.ieee.org/document/10722354/> (visited on 01/09/2025).
- [100] Vladimir Schkolnik et al. “JOKARUS - design of a compact optical iodine frequency reference for a sounding rocket mission”. In: *EPJ Quantum Technology* 4.1 (Dec. 2017), p. 9. ISSN: 2196-0763. DOI: 10.1140/epjqt/s40507-017-0063-y. URL: <http://epjquantumtechnology.springeropen.com/articles/10.1140/epjqt/s40507-017-0063-y> (visited on 12/22/2021).
- [101] Thilo Schuldt et al. “Development of a compact optical absolute frequency reference for space with 10^{-15} instability”. In: *Applied Optics* 56.4 (Feb. 1, 2017), p. 1101. ISSN: 0003-6935, 1539-4522. DOI: 10.1364/AO.56.001101. URL: <https://opg.optica.org/abstract.cfm?URI=ao-56-4-1101> (visited on 09/14/2022).
- [102] D. Sheng, A. Pérez Galván, and L. A. Orozco. “Lifetime measurements of the 5 d states of rubidium”. In: *Physical Review A* 78.6 (Dec. 15, 2008), p. 062506. ISSN: 1050-2947, 1094-1622. DOI: 10.1103/PhysRevA.78.062506. URL: <https://link.aps.org/doi/10.1103/PhysRevA.78.062506> (visited on 08/05/2021).
- [103] Daniel A Steck. *Rubidium 87 D Line Data*. URL: <https://steck.us/alkalidata/rubidium87numbers.1.6.pdf> (visited on 07/24/2024).

Bibliography

- [104] Masao Takamoto et al. “Test of general relativity by a pair of transportable optical lattice clocks”. In: *Nature Photonics* 14.7 (July 2020), pp. 411–415. ISSN: 1749-4885, 1749-4893. DOI: 10.1038/s41566-020-0619-8. URL: <https://www.nature.com/articles/s41566-020-0619-8> (visited on 01/15/2025).
- [105] Osama Terra. “Absolute frequency measurement of the hyperfine structure of the $5S_{1/2}$ – $5D_{3/2}$ two-photon transition in rubidium using femtosecond frequency comb”. In: *Measurement* 144 (Oct. 2019), pp. 83–87. ISSN: 02632241. DOI: 10.1016/j.measurement.2019.04.042. URL: <https://linkinghub.elsevier.com/retrieve/pii/S0263224119303604> (visited on 10/29/2021).
- [106] Robert L. Tjoelker et al. “Mercury Ion Clock for a NASA Technology Demonstration Mission”. In: *IEEE Transactions on Ultrasonics, Ferroelectrics, and Frequency Control* 63.7 (July 2016), pp. 1034–1043. ISSN: 0885-3010. DOI: 10.1109/TUFFC.2016.2543738. URL: <http://ieeexplore.ieee.org/document/7437483/> (visited on 01/06/2022).
- [107] Dylan P. Tooley et al. “A Two-Photon Rb Clock Based on Direct Comb Excitation”. In: *CLEO 2024*. CLEO: Science and Innovations. Charlotte, North Carolina: Optica Publishing Group, 2024, SM2G.3. ISBN: 978-1-957171-39-5. DOI: 10.1364/CLEO_SI.2024.SM2G.3. URL: https://opg.optica.org/abstract.cfm?URI=CLEO_SI-2024-SM2G.3 (visited on 01/13/2025).
- [108] F. Tricot et al. “Power stabilization of a diode laser with an acousto-optic modulator”. In: *Review of Scientific Instruments* 89.11 (Nov. 2018), p. 113112. ISSN: 0034-6748, 1089-7623. DOI: 10.1063/1.5046852. URL: <http://aip.scitation.org/doi/10.1063/1.5046852> (visited on 09/09/2021).
- [109] J. Vanier et al. “Aging, warm-up time and retrace: important characteristics of standard frequency generators (Proposal for IEEE Standards Project P1193)”. In: *Proceedings of the 1992 IEEE Frequency Control Symposium*. 1992 IEEE Frequency Control Symposium. Hershey, PA, USA: IEEE, 1992, pp. 807–815. ISBN: 978-0-7803-0476-5. DOI: 10.1109/FREQ.1992.269956. URL: <http://ieeexplore.ieee.org/document/269956/> (visited on 11/10/2024).
- [110] Benjamin White et al. *The SWaP plot: Visualising the performance of portable atomic clocks as a function of their size, weight and power*. Number: arXiv:2409.08484. Sept. 13, 2024. DOI: 10.48550/arXiv.2409.08484. arXiv: 2409.08484[physics]. URL: <http://arxiv.org/abs/2409.08484> (visited on 01/15/2025).
- [111] N. C. Wong and J. L. Hall. “Servo control of amplitude modulation in frequency-modulation spectroscopy: demonstration of shot-noise-limited detection”. In: *Journal of the Optical Society of America B* 2.9 (Sept. 1, 1985), p. 1527. ISSN: 0740-3224, 1520-8540. DOI: 10.1364/JOSAB.2.001527. URL: <https://opg.optica.org/abstract.cfm?URI=josab-2-9-1527> (visited on 01/30/2025).

- [112] Jan Wuest. “Optical iodine clocks for future GNSS”. In: 9th International Colloquium on Scientific and Fundamental Aspects of GNSS. Wrocław, Poland: European Space Agency, Dec. 2024. DOI: 10.57780/esa-0yq5l8b. URL: <https://gssc.esa.int/education/library/doi/gnss-science-colloquium/2024-wroclaw/>.
- [113] Ning Yang et al. “Research on the temperature characteristics of optical fiber refractive index”. In: *Optik* 125.19 (Oct. 2014), pp. 5813–5815. ISSN: 00304026. DOI: 10.1016/j.ijleo.2014.07.053. URL: <https://linkinghub.elsevier.com/retrieve/pii/S0030402614008031> (visited on 06/05/2024).
- [114] V I Yudin et al. “Combined error signal in Ramsey spectroscopy of clock transitions”. In: *New Journal of Physics* 20.12 (Dec. 18, 2018), p. 123016. ISSN: 1367-2630. DOI: 10.1088/1367-2630/aaf47c. URL: <https://iopscience.iop.org/article/10.1088/1367-2630/aaf47c> (visited on 08/05/2021).
- [115] V. I. Yudin et al. “Universal methods for suppressing the light shift in atomic clocks using power modulation”. In: *Physical Review Applied* 14.2 (Aug. 3, 2020), p. 024001. ISSN: 2331-7019. DOI: 10.1103/PhysRevApplied.14.024001. arXiv: 1911.02935. URL: <http://arxiv.org/abs/1911.02935> (visited on 08/05/2021).
- [116] V.I. Yudin et al. “General Methods for Suppressing the Light Shift in Atomic Clocks Using Power Modulation”. In: *Physical Review Applied* 14.2 (Aug. 3, 2020), p. 024001. ISSN: 2331-7019. DOI: 10.1103/PhysRevApplied.14.024001. URL: <https://link.aps.org/doi/10.1103/PhysRevApplied.14.024001> (visited on 08/05/2021).
- [117] Nathan D Zamoski et al. “Pressure broadening and frequency shift of the $5S_{1/2} \rightarrow 5D_{5/2}$ and $5S_{1/2} \rightarrow 7S_{1/2}$ two photon transitions in ^{85}Rb by the noble gases and N_2 ”. In: *Journal of Physics B: Atomic, Molecular and Optical Physics* 47.22 (Nov. 28, 2014), p. 225205. ISSN: 0953-4075, 1361-6455. DOI: 10.1088/0953-4075/47/22/225205. URL: <https://iopscience.iop.org/article/10.1088/0953-4075/47/22/225205> (visited on 08/05/2021).
- [118] Chuankun Zhang et al. “Frequency ratio of the $^{229\text{m}}\text{Th}$ nuclear isomeric transition and the ^{87}Sr atomic clock”. In: *Nature* 633.8028 (Sept. 5, 2024), pp. 63–70. ISSN: 0028-0836, 1476-4687. DOI: 10.1038/s41586-024-07839-6. URL: <https://www.nature.com/articles/s41586-024-07839-6> (visited on 01/21/2025).
- [119] S. Y. Zhang et al. “Direct frequency comb optical frequency standard based on two-photon transitions of thermal atoms”. In: *Scientific Reports* 5.1 (Dec. 2015), p. 15114. ISSN: 2045-2322. DOI: 10.1038/srep15114. URL: <http://www.nature.com/articles/srep15114> (visited on 08/05/2021).
- [120] W. Zhang et al. “Reduction of residual amplitude modulation to 1×10^{-6} for frequency modulation and laser stabilization”. In: *Optics Letters* 39.7 (Apr. 1, 2014), p. 1980. ISSN: 0146-9592, 1539-4794. DOI: 10.1364/OL.39.001980. URL: <https://opg.optica.org/abstract.cfm?URI=ol-39-7-1980> (visited on 03/07/2022).

Appendix

Science Communication

During my PhD thesis, I had the chance to attend (and win) two contests on science communication. Each time, the goal was to present scientific research in no more than 180 seconds. Here below are the texts that I wrote for the official contest *Ma Thèse en 180 Secondes*¹ and for the CSEM-internal *Science Slam*². The first text addresses a broad public, whereas the second one is written for scientists and engineers.

Ma Thèse en 180 Secondes

Une microseconde, c'est rien du tout. Et 300 mètres ?

Vous l'avez éteint, votre téléphone ? Peu importe, mais sans doute, vous avez déjà utilisé sa fonction GPS. Et j'espère pour vous qu'elle s'est pas trompée de 300 mètres...

Le système GPS est basé sur des satellites. Ces satellites émettent des signaux que votre téléphone reçoit une fraction de seconde plus tard. Ce petit décalage n'est pas embêtant, mais il permet de vous localiser. Car la vitesse du signal et son temps de voyage donnent la distance entre vous et le satellite. Et à l'aide de plusieurs satellites bien synchronisés, le téléphone calcule votre position.

Tout va bien jusqu'ici. Alors revenons sur la microseconde. Dans ce temps minuscule, un signal GPS fait une distance de 300 mètres. Alors une microseconde est beaucoup. C'est la différence entre l'hôpital de la Providence et ici [Aula des Jeunes-Rives, Neuchâtel]. Pour éviter une telle incertitude, les satellites doivent tous avoir l'heure précise. Et là, votre belle vieille Tissot ne suffit plus. Il nous faut autre chose: une horloge atomique.

Mais c'est quoi une horloge atomique ? Réponse simple : le sujet de ma thèse. Réponse utile: une horloge normale, mais avec un horloger personnel. Un horloger qui ne dort jamais et

¹Held on 30 March 2023 at the University of Neuchâtel

²Held on 28 June 2024 at CSEM, Neuchâtel

qui règle son horloge 24 heures sur 24. Et les meilleurs horlogers, ce ne sont ni les Chaux-de-Fonniers, ni les Biennois, mais les atomes.

Mon horloger s'appelle rubidium. Et son travail est de régler un laser. Un laser a une longueur d'onde bien définie. Ce qu'on appelle la longueur d'onde est mieux connue sous le nom de "couleur". Et chaque couleur a son propre tic-tac. Cela veut dire que la couleur du laser dicte la vitesse à laquelle avance l'horloge. Mon horloger adore un rouge invisible à l'œil humain. Alors il règle le laser à cette couleur. Et tant qu'il le fait avec soin, le tic-tac de l'horloge n'est ni trop lent, ni trop rapide. On pourrait aussi dire que le laser et l'horloger sont sur la même longueur d'onde.

Encore 37 secondes, dit l'horloge. Vous l'imaginez bien, l'histoire n'est pas encore finie. Quelque chose dérange mon horloger. C'est le laser même. Parfois, il brille plus ou moins fort. Pas beaucoup, mais beaucoup trop pour des chercheurs comme moi. C'est pourquoi le but de ma thèse est de l'aider à se concentrer pleinement. Et comme j'aime bien les lasers, je vais en utiliser un deuxième. J'espère qu'il va l'aimer autant que moi. Et avec sa belle lumière, il pourra faire son meilleur travail.

Science Slam

Something to the power of eighty-two. So many atoms are there in the universe. So why not take some of them and make something nice? For instance, an atomic clock.

An atomic clock is like a normal clock, but really stubborn. It just won't change its mind, no matter how hard you try. A normal clock, in comparison, is really moody. So macroscopic effects like temperature will change its frequency. Depending on how it feels, it will tick faster or slower.

But not so the atomic clock. Because the way it ticks is the way it sticks to what its consultants consult. In my case rubidium-87 – the hot stuff. More specifically: a hot atomic vapor cell at 100 degree Celsius. And since all the atoms are of the same isotope, they all do, feel and act the same. Not good for diversity, but really good for an atomic clock.

So how do you talk to atoms? The language of resonance. You can talk it to a bridge, you get a catastrophe. But you talk it to atoms, you get the most precise devices ever made: atomic clocks.

An atom is not a cat – you can put it in a microwave. And if it's on resonance, you get a really high quality factor. The quality factor is the ratio of the frequency of the resonance to how narrow it is. And the higher it is, the better. That is why for decades, we've been using atomic clocks based on microwave transitions. But we wouldn't be in the 21st century, if we didn't have something fancier: lasers.

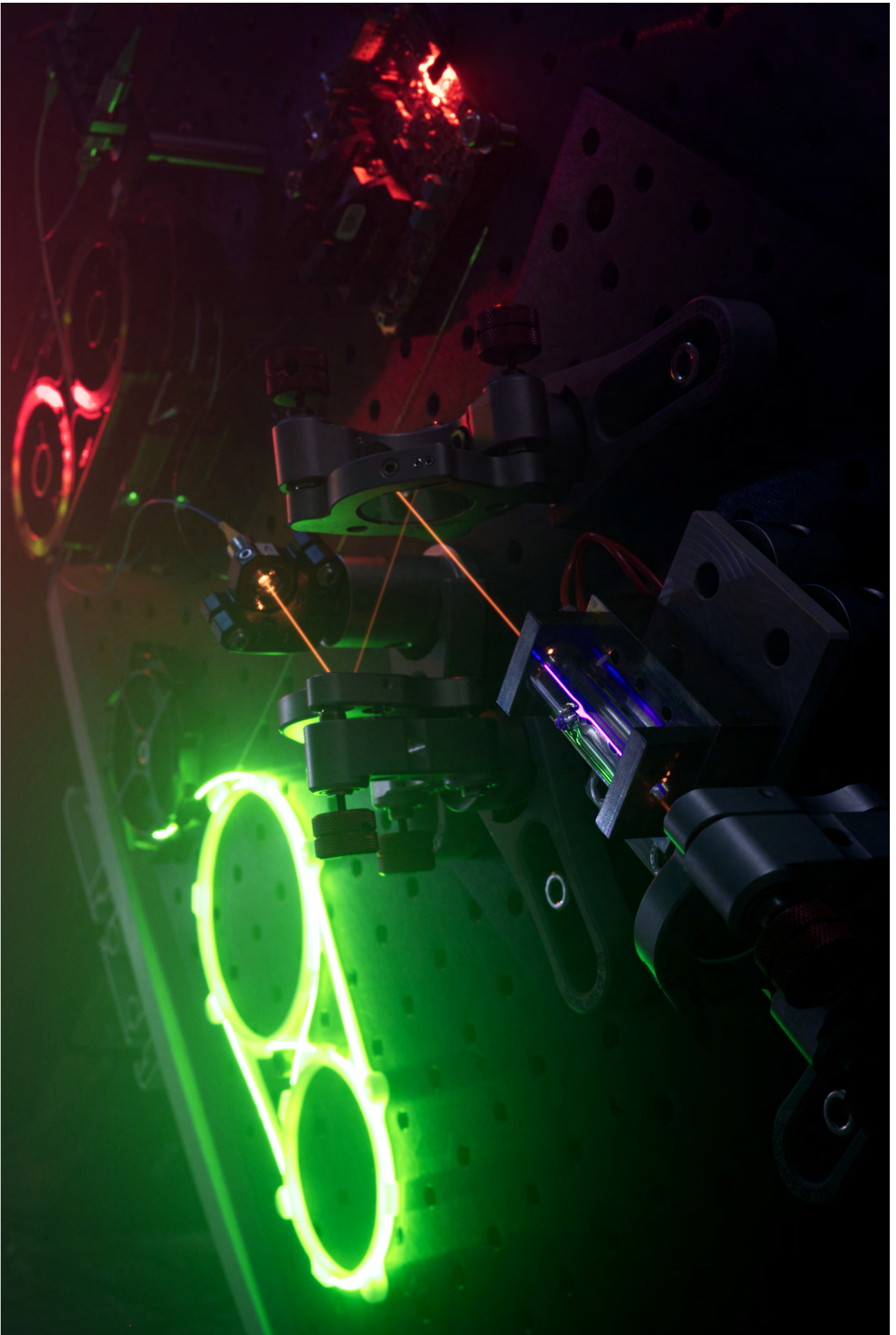
My clock ticks on this laser here [pointing to image]. It is the heartbeat of the clock. But still, it's a laser. And I'm sure you can feel with my atoms. Not only are they confined in this tiny vapor cell, but they are also confronted 24/7 to this *hot chili laser*. And this hot chili laser, it

perturbs the rubidium. Even though it's a really good consultant, when there is more laser power, it will tick slower. And if there is less, it will tick faster.

That is why I want to counteract that with another laser: the *milk laser*. And so far, I've shown that it works in some cases. I will look at other cases, and with these, I can decide if the addition of a milk laser is actually useful or not. So stay tuned, stay on resonance. Thank you.

Red, Blue and Green - An Artistic View on the Two-Photon Clock

The photograph on the next page illustrates the working principle of the rubidium two-photon clock. The picture is not representative of the setup described in the main part of this thesis. I arranged the different optics components such that the key elements of the system are highlighted: the interrogation laser beam in red, the fluorescence signal in blue, and the amplification of the clock laser with an erbium-doped fiber in green. The interrogation beam is visualized with a fog machine. It is obtained by amplifying and frequency-doubling a portion of light from a laser which is locked to the two-photon transition using another vapor cell not shown in the image. The photograph was shot in a single exposure. I made no adjustments to the picture except for the usual post-processing of the raw image file. © Roman Blum 2024.



ROMAN BLUM

German Mother tongue
English Full working proficiency
French Full working proficiency
IT/NL/SV Advanced basic knowledge

01.10.1993
Swiss (CH)

PROFESSIONAL EXPERIENCE



2025
(2021-2025)

PhD in Science. Fields: **Time & Frequency** and **Photonics**
Light Shift Mitigation for the Rubidium Two-Photon Atomic Clock
CSEM + University of Neuchâtel, with 3-month research stay
at the **European Space Agency (ESA)**, ESTEC, Netherlands
Topics: Atomic clock, frequency and time transfer, laser optics,
mechanical design, electronics, data acquisition and analysis



2018
(6 months)

Internship, **ROLEX S.A.**, Geneva, Switzerland
Project Responsible R&D, Micro Technologies



2012-13
(10 months)

Military Service, **Swiss Army**, different locations
Corporal in Nuclear/Biological/Chemical Defense



EDUCATION



2019
(2016-2019)

MSc in Microengineering (5.42/6), Lausanne, Switzerland
Ecole Polytechnique Fédérale de Lausanne (**EPFL**)



2019
(6 months)

Master Thesis about Silicon Photonics (6/6)
University of California, Berkeley, USA



2016
(2013-2016)

BSc in Microengineering (4.86/6), **EPFL**
with **exchange year** at KTH, Stockholm, Sweden



2012

Swiss Federal Matura, (5.80/6), bilingual DE/EN
Gymnasium Kirchenfeld, Bern, Switzerland



EXTRACURRICULAR ACTIVITIES



2013-23
(10 years)

Swiss Study Foundation, active member, participation in
30+ events including **summer schools** on highly diverse subjects



2016-18
(2 years)

Dynamic the Students' Association Microengineering at EPFL
Committee member: photographer (2016-18), treasurer (2017-18)



AWARDS



2024

EFTF 2024 Student Best Paper Competition
winner in category Compact Clocks and Precision Spectroscopy



2023

Ma Thèse en 180 Secondes: Sélection Neuchâteloise
winner science communication contest at University of Neuchâtel



2012

Multiple awards linked to Swiss Matura
best matura paper in science, excellent average grade, etc.

